

A CFD Study on the Performance of High Speed Planing Hulls

Mowgli J. Crosby

A Thesis Submitted to the Graduate Faculty of

GRAND VALLEY STATE UNIVERSITY

In

Partial Fulfillment of the Requirements

For the Degree of

Master of Science in Mechanical Engineering

School of Engineering

December 2019

Acknowledgments

I would like to take this opportunity to thank committee for their continued support throughout this project and especially thank my thesis committee chair, Dr. Mokhtar, for his continued support. It would not have been possible without his guidance. I would also like to thank Dr. Fleischmann for her assistance with the scale model testing, constant enthusiasm, and general interest in the topic. In addition, I would like to thank Dr. Reffeor for her valuable suggestion and critiques. Finally, I would like to thank Grand Valley State University for giving me the opportunity to pursue further education and for providing me with all of the resourced needed to complete my research.

Abstract

Most high speed water craft are able to achieve high speeds through the use of a planing hull. Planing hulls use hydrodynamic forces to lift a portion of the vessel out of the water, reducing drag, and allowing for greater speeds. Determining the flow around such vessels is traditionally achieved using a scale model in a tow tank. The purpose of this study was to analyze the performance of a high speed planing hull determine the effects of several geometric features using computational fluid dynamics rather than traditional experimentation. The goal was to determine the best configuration to ensure the lowest resistance on the hull at high speed. This was achieved using STAR CCM+ to solve a three dimensional computational analysis for the multiphase flow and dynamic motion of a planing hull. An initial simulation was created for a 25 ft base hull and validated using experimental data from a towing tank. After developing an accurate simulation for a single hull, the hull geometry was modified to test for the effects of the keel line geometry, deadrise angle, and spray rail location.

A full factorial DOE analysis was performed to examine the effects of the tested geometric features and the interactions between them. The results from this analysis showed that the tested features had a significant effect on the performance of the hull. Increasing the deadrise angle resulted in a decrease in sinkage, an increase in trim angle, and an increase in the total drag on the hull. Raising the keel line height caused a decrease in trim angle and sinkage, while increasing the total drag. These two terms had a significant interaction. As one increased, the relative effect of changing the other also increased for total drag. The final geometric feature tested was the spray rails. Adding spray rails to the bottom of the hull significantly increased the sinkage. Moving the location of the spray rails away from the center of the hull increased the total drag. This showed that the total drag could be significantly reduced by altering these geometric features of the hull.

Table of Contents

Acknowledgments.....	3
Abstract	4
Table of Contents	5
List of Figures	8
List of Tables	11
Nomenclature	13
Abbreviations	16
1. Introduction.....	17
1.1 Background.....	17
1.2 Typical Hull Geometry	19
1.3 Fluid Resistance Equations.....	22
2. Literature Review.....	25
2.1 Types of Drag	25
2.1.1 Viscous Hull Resistance	26
2.1.2 Wake Making Resistance.....	27
2.1.3 Air Resistance	28
2.2 Effect of Deadrise Angle	28
2.3 Effect of Chine.....	30
2.4 Effect of Spray Rails.....	32
2.5 Effect of Keel Line Depth.....	33
2.6 Effects of Other Characteristics	34
3. CFD Theory	37

4.1 Conservation of Mass	38
4.2 Conservation of Momentum	39
4.3 Conservation of Energy	41
4.4 Navier-Stokes Equations.....	41
4.4 Turbulence Modeling.....	42
4.5 Multiphase Flow	44
4.6 Fluid Structure Interaction	45
4. Methodology	48
5. Phase I: Base Hull Simulation	51
5.1 CFD Model	51
5.1.1 CAD Model.....	51
5.1.2 Physics Model	57
5.1.3 Boundary Conditions	59
5.1.4 Mesh Model	59
5.2 Phase I Results	62
5.2.1 Mesh Convergence Results	63
5.2.2 Base Hull Simulation Results	66
6. Phase II: Model Validation	74
6.1 Procedure	74
6.2 Scale Model Results.....	79
7. Phase III: Effects of Geometric Features	85
7.1 Procedure	85
7.2 Single Characteristic Results	88

7.3 Full DOE Results	93
7.3.1 Total Drag Results	93
7.3.2 Trim Angle Results	100
7.3.3 Sinkage Results	101
7.4 Geometric Analysis Conclusions.....	103
8. Conclusion	105
9. Future Work	108
References.....	109
Appendix A – Drawings	113

List of Figures

Figure 1. Planing Hull.....	17
Figure 2. Resistance Curve for a Planing Hull	19
Figure 3. Planing Hull Geometry.....	20
Figure 4. Ideal Flow around a Body	26
Figure 5. Actual Flow around a Body.....	26
Figure 6. Example of Deadrise Angle.....	29
Figure 7. An Example of the Chine	31
Figure 8. An Example of Spray Rails	32
Figure 9. An Example of the Keel Line	33
Figure 10. Control Volume used for Deriving Governing Equations.....	37
Figure 11. Conservation of Mass Differential Element	38
Figure 12. Shear Stress in only x-Direction.....	40
Figure 13. Flow Chart used to Describe Iterative Process.....	47
Figure 14. Visualization of Deadrise Angle Changes.....	49
Figure 15. Visualization of Keel Line Geometry Changes.....	50
Figure 16. Visualization of Spray Rail Location Changes	50
Figure 17. CAD Model	52
Figure 18. CAD Model Front View	53
Figure 19. CAD Model Side View	53
Figure 20. CAD Model Bottom View.....	53
Figure 21. Center of Mass.....	54
Figure 22. Final Simulation Geometry	55

Figure 23. Overset Region	55
Figure 24. Simulation Far Field	56
Figure 25. Boundary Conditions Used in the Simulations	59
Figure 26. The Surface Mesh.....	60
Figure 27. The Tested Volume Mesh with (a) 213,490 Cells, (b) 423,509 Cells,.....	61
Figure 28. The Overset Mesh.....	62
Figure 29. Drag Convergence Plot.....	64
Figure 30. Motion Convergence Plot.....	64
Figure 31. (a) Side View and (b) Top View of the Final Far Field Volume Mesh.....	65
Figure 32. (a) Side View and (b) Top View of the Final Far Field Overset Mesh.....	66
Figure 33. Final Prism Layer for the Hull.....	66
Figure 34. Motion Plot for the Base Hull	68
Figure 35. Visualization of Hull Motion.....	68
Figure 36. Base Hull Resistance Curve	69
Figure 37. Drag Coefficient	69
Figure 38. Wetted Surface Area at Different Test Speeds.....	71
Figure 39. Wake Pattern at Different Test Speeds.....	72
Figure 40. Scale Model Hull.....	74
Figure 41. Scale Model Front View.....	75
Figure 42. Scale Model Bottom View	75
Figure 43. Scale Model Side View	75
Figure 44. GVSU 12 ft Tow Tank	76
Figure 45. (a) The Strain Gage, (b) the Hanging Mass, (c) the Attachment on the Towing Arm	77

Figure 46. Simplified Calibration Diagram	77
Figure 47. Scale Model in Towing Tank	78
Figure 48. Applied Force vs Measured Strain Plot.....	79
Figure 49. Simulated and Scale Model Results	81
Figure 50. Simulated and Scale Model Drag Coefficients	81
Figure 51. Side View of Simulated Hull at $Fr = 0.24$	82
Figure 52. Side View of Scale Model Hull at $Fr = 0.24$	82
Figure 53. Single Parameter's Effect on Total Drag.....	89
Figure 54. Single Parameter's Effect on Trim Angle	89
Figure 55. Single Parameter's Effect on Sinkage	89
Figure 56. Wetter Surface Area Due to Spray Rails.....	91
Figure 57. Flow Field Created Spray Rail on the Bottom of the Hull	92
Figure 58. Normal Quantile Plot.....	95
Figure 59. Total Drag Residual Plot	95
Figure 60. Studentized Total Drag Residual Pot	95
Figure 61. Single Effect Profiler for Total Drag with Different Spray Rail Location	97
Figure 62. Interaction Profiler for Total Drag with Different Spray Rail Location	98
Figure 63. Single Effect Profilers for Total Drag with the Addition of Spray Rails	99
Figure 64. Single Effect Profiler for Trim Angle with Spray Rail Location	100
Figure 65. Single Effect Profiler for Trim Angle with the Addition of Spray Rails Added.....	101
Figure 66. Single Effect Profiler for Sinkage with Spray Rail Location	102
Figure 67. Single Effect Profiler for Sinkage with the Addition of Spray Rails Added.....	103

List of Tables

Table 1. Relevant Study Information.....	36
Table 2. k- ϵ Turbulence Modeling Constants [20]	43
Table 3. k- ω Turbulence Modeling Constants [21]	44
Table 4. Hull Geometry Test Parameters.....	49
Table 5. Hull Dimensions	52
Table 6. Hull Mass Features	54
Table 7. Overset Dimensions.....	56
Table 8. Far Field Dimensions.....	56
Table 9. Tested Mesh Values for Convergence Study.....	60
Table 10. Mesh Convergence Results.....	63
Table 11. Final Mesh Values	65
Table 12. Base Hull Results.....	67
Table 13. Scale Model Dimensions	74
Table 14. Towing Tanks Dimensions	76
Table 15. Tested Speeds	78
Table 16. Towing Tank Calibration Results	79
Table 17. Scale Model Results.....	80
Table 18. Trim and Sinkage Values at $Fr = 0.24$	83
Table 19. Hull Geometry Characteristics.....	85
Table 20. DOE table	86
Table 21. Single Term Effects Results	88
Table 22. Complete DOE Results.....	93

Table 23. Total Drag ANOVA Results.....	94
Table 24. Reduced Total Drag ANOVA Results.....	96
Table 25. Total Drag ANOVA Results for Spray Rail Location.....	97
Table 26. Total Drag ANOVA Results with Added Spray Rails	98
Table 27. Reduced Total Drag ANOVA Results with Added Spray Rails	99
Table 28. Reduced ANOVA Results for Trim Angle with Spray Rail Location	100
Table 29. Reduced ANOVA Results for Trim Angle with the Addition of Spray Rails.....	101
Table 30. Reduced ANOVA Results for Sinkage with Spray Rail Location	102
Table 31. Reduced ANOVA Results for Sinkage with the Addition of Spray Rails.....	102

Nomenclature

A	<i>Sectional Area of Towing Tank</i>
A_x	<i>Maximum Sectional Area of Model</i>
b	<i>Beam Length</i>
C_{AA}	<i>Coefficient of Air Resistance</i>
C_{L0}	<i>Lift Force on Planing Plates</i>
C_s	<i>Speed Coefficient</i>
C_T	<i>Coefficient Total of Hull Resistance</i>
C_V	<i>Coefficient of Viscous Resistance</i>
C_W	<i>Coefficient of Wave Making Resistance</i>
$C_{L\beta}$	<i>Lift Force on a Planing Hull</i>
E	<i>Total Energy</i>
F	<i>Applied Force</i>
F_{net}	<i>Net Force</i>
F_r	<i>Froude Number</i>
F_{rh}	<i>Depth Froude Number</i>
g	<i>Acceleration due to Gravity</i>
h	<i>Depth of Water</i>
H_a	<i>Alternative</i>
H_o	<i>Hypothesis</i>
I	<i>Inertia Tensor</i>
k	<i>Turbulent Kinetic Energy</i>
L	<i>Length of the Hull</i>

L_f	<i>Lift Forces</i>
L_m	<i>Mean Wetted Length</i>
m	<i>Mass</i>
m_b	<i>Blockage Ratio</i>
\dot{m}	<i>Mass Flow Rate</i>
p	<i>Pressure</i>
P_k	<i>Production of Turbulent Kinetic Energy</i>
q	<i>Heat Added</i>
R^2	<i>Coefficient of Determination</i>
Re	<i>Reynolds Number</i>
R_{AA}	<i>Air Resistance</i>
R_T	<i>Total Resistance</i>
R_V	<i>Viscous Resistance</i>
R_W	<i>Wake Making Resistance</i>
S	<i>Wetted Surface Area of the Hull</i>
S_i	<i>Body Force</i>
t	<i>Time</i>
U	<i>Velocity Vector</i>
u	<i>Velocity Component in the x Direction</i>
v	<i>Velocity Component in the y Direction</i>
V	<i>Velocity of Hull</i>
w	<i>Velocity Component in the z Direction</i>

α	<i>Significance Level</i>
α_i	<i>Effects due to Factor A</i>
β	<i>Deadrise Angle</i>
β_j	<i>Effects due to Factor B</i>
γ	<i>Volume Fraction</i>
γ_k	<i>Effects due to Factor C</i>
ε	<i>Dissipation</i>
ε_μ	<i>Microstrain</i>
ϵ	<i>Experimental Error</i>
λ	<i>Non-Dimensional Mean Wetted Length</i>
μ	<i>Dynamic Viscosity</i>
μ_j	<i>Population Mean</i>
μ_t	<i>Turbulent Viscosity</i>
ρ	<i>Density of the Fluid</i>
τ	<i>Shear Stress</i>
τ_θ	<i>Dynamic Trim Angle</i>
ν	<i>Kinematic Viscosity of the Fluid</i>
ω	<i>Specific Dissipation</i>
ω	<i>Angular Velocity</i>

Abbreviations

<i>ANOVA</i>	<i>Analysis of Variance</i>
<i>CAD</i>	<i>Computer Aided Design</i>
<i>CFD</i>	<i>Computational Fluid Dynamics</i>
<i>DFBI</i>	<i>Dynamic Fluid Body Interaction</i>
<i>DOE</i>	<i>Design of Experiment</i>
<i>FSI</i>	<i>Fluid Structure Interaction</i>
<i>DOF</i>	<i>Degrees of Freedom</i>
<i>RANS</i>	<i>Reynolds Averaged Navier-Stokes Equation</i>
<i>SST</i>	<i>Shear Stress Transport</i>
<i>VOF</i>	<i>Volume of Fluid</i>

1. Introduction

Planing hulls have been around since the late 19th century and have been the dominant design for high speed water craft. They have been used for recreation, racing, and transportation. Through the use of hydrodynamic forces, boats with planing hulls are able to outperform most traditional vessels. They are able to achieve greater speeds with minimal fuel consumption due to the low hull resistance that planing is able to achieve. Traditionally, hull resistance is determined using experimentations with scale models in a tow tank. But this method can be time consuming and expensive. A more universal method for determining hull resistance is to simulate the flow using computational fluid dynamics (CFD). This method uses numerical methods to analyze fluid flow, can be used to accurately model a system, and can determine the flow properties including resistance of any hull.



Figure 1. Planing Hull

1.1 Background

Most boat hulls fall into one of two categories: displacement and planing hulls. Displacement hulls push the water aside and are designed to cut through the water. This allows

them to move smoothly through the water, but are limited to slower speeds. They are used today in sail boats and large container vessels, but have been the predominate design for most of human history. It was not until the late 19th century that major advancements were made in both hull design and propulsion systems. The first boat powered by a gasoline engine was built in 1886, and the earliest known planing hull was built in 1898. The design was not popularized until 1928 when Uffa Fox, in his planing boat *Avenger*, won 52 of 57 races of the International Fourteen Footer [1]. This was possible because his planing vessel created lift through the hydrostatic pressure distribution on the hull. This lift can support a significant amount of a ship's weight and can even lift a portion of the hull out of the water. This reduces the wetted surface area, and allows the boat to achieve much greater speeds than a traditional displacement hull [2].

Planing vessels have three distinct operating regimes: displacement, transition, and planing. At low speed, when the Froude Number (F_r) $< \sim 0.5$, planing hulls act similar to traditional displacement hulls. They push the water aside and do not generate enough lift to raise the boat out of the water. At speeds of $F_r > 0.5$, the hull will move into a transition region where it is neither planing nor operating in a displacement condition. During this phase, the boat will have a large trim angle and resistance [2]. During the transition region, there is a distinct hump in the resistance curve where the drag on the hull is greater than that of the other regions as shown in Figure 2. As the vessel increases in speed, the hydrodynamic forces acting on the hull continue to increase and create more lift. This begins to move the hull toward the surface of the water. Once the $F_r > 0.85$, the hull is finally fully in the planing regime. To achieve planing, the hull has to overcome a so-called resistance barrier, which requires a large amount of power. Large engines are required to transition from displacement to the planing regime. The performance of planing hulls is also highly dependent on the center of gravity. This location affects how quickly the boat will transition to

planing. The further back the center of gravity is located, the longer it will take to overcome the resistance barrier and the transition region. Once planing has been achieved, the boat is more efficient and requires less power to maintain speed [2]. This is because the wetted surface area is reduced, and thus lowering the skin friction drag.

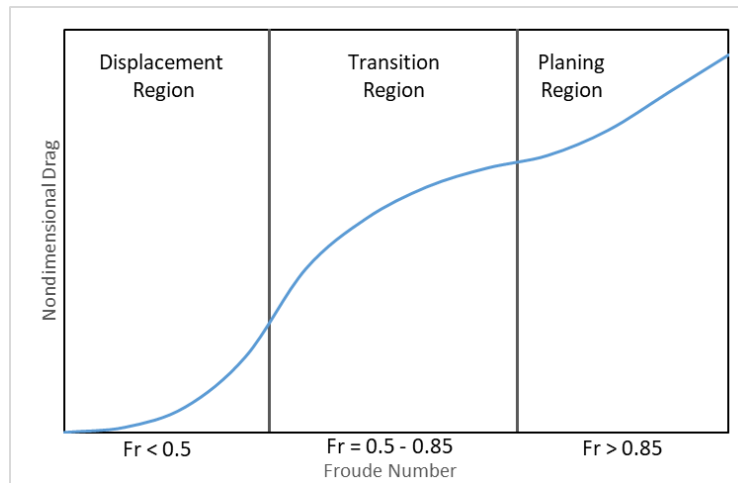


Figure 2. Resistance Curve for a Planing Hull

In this state, the flow becomes two-phase and the solution to the traditional analytical techniques become impossible. This creates the need for other methods analyzing hull design. Experimental testing through the use of tow tanks is the most reliable way of modeling these flows, but can be very expensive to perform. This leads to the use of computation fluid dynamics as the primary tool used for analyzing the flow around a planing hull.

1.2 Typical Hull Geometry

Planing hulls make use of several key geometric features to reduce drag, create lift, and achieve the greatest possible speed. Figure 3 shows the common geometric features of a planing hull.

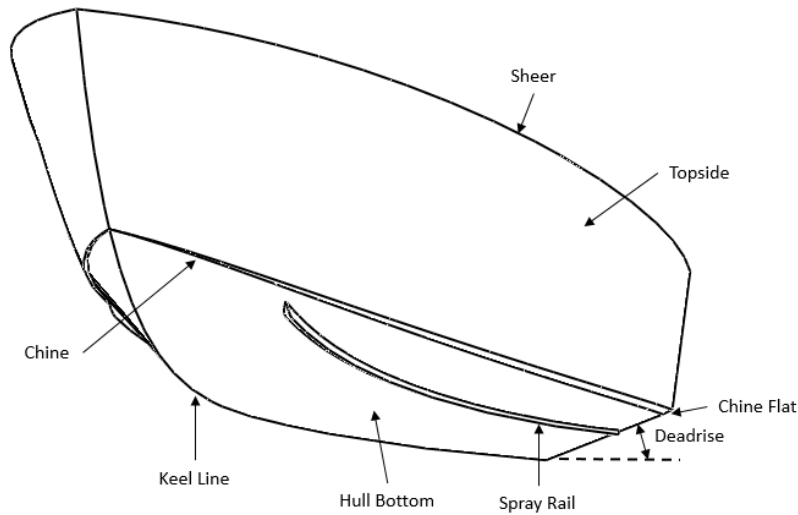


Figure 3. Planing Hull Geometry

There are several terms which are essential to understanding the geometry of a hull. They can be defined as follows [3], [4]:

- *Beam*: The boat's overall width.
- *Bow*: The forward end of the boat.
- *Chine*: The intersection of the bottom and sides of the hull. Usually immersed below the waterline from midship back.
- *Deadrise*: The angle between the bottom of the hull with a horizontal surface.
- *Draft*: The total distance the boat penetrates the water.
- *Hull*: The physical portion of the boat that sits on the water.
- *Keel*: The portion of the boat that is the furthest below the water's surface.
- *Sheer Line*: The upper profile of boat.
- *Spray Rail*: A sharp board mounted protrusion that is designed to redirect bow waves downward and reduce spray.
- *Stern*: The aft most section of the boat.

- *Transom*: The flat outboard stern structure of a ship from keel to deck.
- *Trim*: The difference between the draft forward and the draft aft, or the angle of the boat in the water.
- *Waterline Length*: The length of the hull where it intersects the water from bow to stern.

Certain features have a significant impact on the performance of the boat. The deadrise angle has affects on both the total drag and the quality of the ride. Flat bottom vessels with a deadrise angle of 0 degrees move smoothly through still water, but in rough water they are subject to slamming as the hull falls off of the crest of a wave back to the water surface. This can damage the hull and can sometimes cause severe injuries to the passengers onboard. Having a deadrise angle allows the hull to cut through the surface of the water, travel smoothly on both calm and rough seas, while reducing the total resistance of the hull [2].

The chine has a similar effect. At higher speeds and in turbulent water, a chine can cause smother hull motion and increase the stability. The chine is considered to become harder as the angle between the bottom and sides of the hull increase. The chine cuts the water and is intended to spray water to the side. As the chine becomes harder, more water is sprayed to each side [3]. This prevents water from rising up the hull, reduces the wetted area, decreases the drag, and increases the possible speed of the vessel.

Spray rails can improve both the performance and efficiency of planing hulls. Spray rails have a similar purpose to the chine, to redirect the upcoming water. As the water moved across the bottom of the hull, the stray rails are able to redirect the water downward. This is used to confine the water to the bottom of the hull and generate lift. This reduces the wetted surface area, and increases the efficiency of the hull. They usually have a triangular cross section and sharp edges in order to prevent stagnation points from forming [2].

1.3 Fluid Resistance Equations

The analysis of hull performance uses several equations. The United States Naval Academy has outlined the following equations [5]. As a ship moves through the water, there are numerous factors that contribute to the total drag. The total resistance (R_T) can be expressed as:

$$R_T = R_V + R_W + R_{AA} \quad 1$$

Where R_V is the viscous friction, R_W is the wave making resistance, and R_{AA} is the air resistance. The resistance can also be written using dimensionless terms. The total coefficient of hull resistance (C_T) can be expressed as:

$$C_T = C_V + C_W + C_{AA} \quad 2$$

Where C_V is the coefficient of viscous resistance, C_W is the coefficient of wake making resistance, and C_{AA} is the coefficient of air resistance. Since the total resistance is dependent on the hull geometry, motion and fluid properties, the coefficient of total hull resistance can also be expressed as:

$$C_T = \frac{R_T}{\frac{1}{2}\rho V^2 S} \quad 3$$

Where R_T is the total hull resistance, ρ is the density of water, V is the velocity, and S is the wetted surface area of the hull. The lift coefficient (C_L) can be expressed as [6]:

$$C_L = \frac{L_f}{0.5\rho V^2 b^2 \lambda} \quad 4$$

Where L_f is the lift, ρ is the density of water, V is the velocity, b is the beam length and λ is the non-dimensional mean wetted length given by:

$$\lambda = \frac{L_m}{b} \quad 5$$

Where L_m is the mean wetted length, and b is the beam length. To determine the lift force, two components are needed. The first is generated by the hydrodynamic pressure and the second is from the hydrostatic lift from buoyant pressure. Savitsky equation [6] for lift on planing plates (C_{L0}) is given by:

$$C_{L0} = \tau_\theta^{1.1} \left(0.012\sqrt{\lambda} + \frac{0.0055\lambda^{2.5}}{C_s^2} \right) \quad 6$$

Where τ_θ is the dynamic trim angle, λ is the non-dimensional mean wetted length, and C_s is the speed coefficient given by:

$$C_s = \frac{V}{\sqrt{gb}} \quad 7$$

Where V is the velocity, g is the acceleration due to gravity, and b is the beam length. The total lift force ($C_{L\beta}$) acting on the bottom of a hull can be found using:

$$C_{L\beta} = C_{L0} - 0.0065\beta C_{L0}^{0.6} \quad 8$$

Where C_{L0} is the lift on a flat plate, and β is the deadrise angle. The dimensionless form of velocity for ship speed is the Froude Number (F_r) [5] and can be expressed as:

$$F_r = \frac{V}{\sqrt{gL}} \quad 9$$

Where V is the velocity, g is the acceleration due to gravity, and L is the length of the ship. Reynolds Number (R_e) is another dimensionless number that represents the ratio of inertia forces to viscous forces and can be expressed as:

$$R_e = \frac{LV}{\nu} \quad 10$$

Where L is the length of the ship, V is the velocity and ν is the kinematic viscosity of water. When a ship moves through the water, it creates a wave. The wave length (L_w) [5] can be determined by the following:

$$L_w = \frac{2\pi V^2}{g} \quad 11$$

Where V is the velocity, and g is the acceleration due to gravity. The speed when the wave length is equal to the length of the hull is known as the hull speed (V_s) and is expressed as:

$$V_s = 1.34\sqrt{L} \quad 12$$

Where L is the ship length.

2. Literature Review

There have been many studies performed on the optimization of planing hulls. They have focused on the reduction of the total hull resistance. This was accomplished through the reduction in one of the three forms for hull drag: viscous resistance, wave making resistance, and air resistance. Each form of resistance has unique physics and can be reduced in different ways. Viscous resistance is proportional to the wetted surface area of the hull and can be reduced by creating more lift or spraying the water away from the hull. The wave making resistance is affected by the amount of water displaced, and air resistance is due to the boat geometry above the water. Each of these can be reduced through the use of different geometric features. These include the deadrise angle, the chine, spray rails, and the keel line geometry. To properly understand the effects of these features, previous studies performed have been discussed.

2.1 Types of Drag

As a hull moves through the water, the ship experiences a force acting in the opposite direction of the motion. This represents the water's resistance to the motion of the ship, and is commonly called the total hull resistance. The total resistance can be broken into three main components: viscous resistance of the water acting on the hull, wave making resistance, and air resistance [5]. At low speed, viscous resistance is the main contributing factor to the total resistance. This is due to minimal energy being expended in the creation of a wake, and water's much greater viscosity than air. But as the velocity increases, wave making resistance becomes the dominate factor [5].

2.1.1 Viscous Hull Resistance

The ideal flow around a submerged body is characterized by the fluid passing smoothly over the entire surface, staying attached to the surface, and the pressure distribution being normal to the body. This is shown in Figure 4 and results in smooth streamlines along the surface. In the ideal flow, there is no drag on the body. There is a component of pressure resisting the motion in the forward section of the body, but there is also a component of pressure assisting the motion on the aft section [7]. This results in a net force of zero, meaning there is no drag.

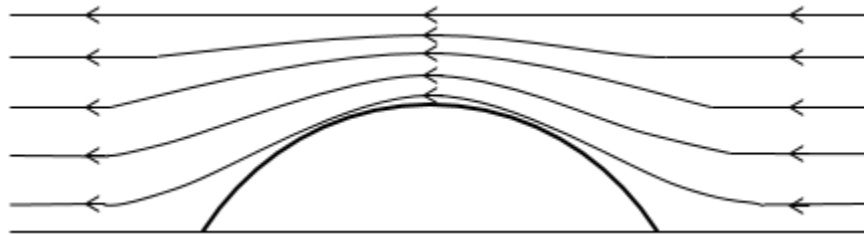


Figure 4. Ideal Flow around a Body

In reality, the flow is not ideal and drag is present. As a fluid passes over a body, it clings to the surface, resulting in the formation of a boundary layer as shown in Figure 5. Within this layer, the flow rapidly changes in speed, from zero at the surface of the body, to free stream velocity far from the surface. This results in two forms of drag: viscous friction resistance resulting from shear stress within the fluid, and viscous pressure resistance resulting from a pressure differential.

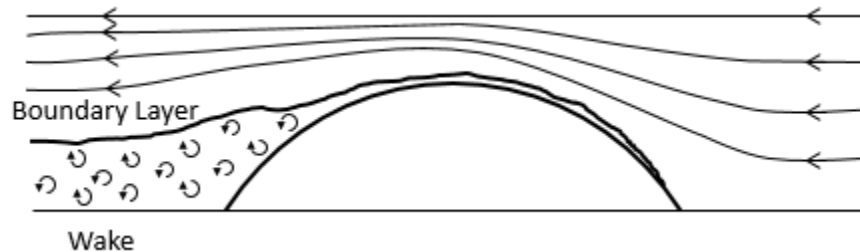


Figure 5. Actual Flow around a Body

For a ship's hull, the frictional resistance is a function of the shape of the hull, the wetted surface area, the surface roughness of the hull, and the water's viscosity. As a boat moves through the water, the velocity of the water at the hull's surface is equal to the speed of the boat. As the distance from the hull increases, the velocity moves toward the free stream velocity. This velocity gradient creates shear stress in the water and thus drag [5]. The viscous pressure resistance is caused by a pressure differential along the hull. At the bow of the boat, the water's impact on the hull creates a high pressure area known as a stagnation point. As the flow passes over the hull, it begins to separate, resulting in the formation of a low pressure wake. So at the aft of a hull, there is a low pressure region [5]. This difference in pressure results in a force acting in the opposite direction of the boat's motion.

2.1.2 Wake Making Resistance

The creation of waves requires energy. As the speed of the boat increases, the height of the produced waves also increases and thus requires more energy. This loss of energy is known as wave making resistance. The waves generated are stationary when observed from the boat or along the side of the hull. The wavelength increases as the velocity is increased until the wavelength is equal to the length of the hull. At this point, the waves generated at the bow and stern are in phase [8]. This critical velocity is known as the hull limit speed. This can be overcome by small powerful boats capable of reaching the planing regime. Once in this regime, the hydrodynamic lift becomes significant and is able to raise a portion of the hull out of the water. This corresponds with a sharp decrease in wake drag and an increase in acceleration as the mass of the displaced water decreases [9]. The sudden decrease in wake drag is often overlooked as the viscous resistance continues to increase. As the boat continues to increase in speed while planing, the wake drag does continue to increase but at a slower rate.

2.1.3 Air Resistance

Air resistance is very similar to the viscous resistance. Viscous hull resistance acts on the portion of the hull below the water and air resistance acts on the portion of the boat above the water. This means the main difference is what fluid is acting on the ship and the corresponding fluid viscosity. The viscosity of water is in the magnitude of 50 times greater than that of air [7]. This results in significantly more drag. As a result, resistance due to air is typically 4-8% of the total ship resistance [5]. Reducing air drag is possible through the use of more streamline geometry or reducing the projected frontal area, but the potential drag reductions are overshadowed by the cost of manufacturing.

2.2 Effect of Deadrise Angle

The deadrise is the angle between the bottom of the hull and a horizontal plane as shown in Figure 6. The deadrise affects the stability, the smoothness of the ride, lift, wetted surface area and the drag of a ship. The angle changes depending on the operating conditions for the boat. For inshore crafts, to be used on small, calm lakes, the deadrise angle is usually around 10° - 12° at the aft and increases from midships towards the bow. For coastal craft, designed for use near the coast of large bodies of water, the deadrise is larger and is often 15° - 20° . The increase in angle is present to allow the hull to cut through larger waves, reduce the impact forces on the hull, and create a smoother ride. Finally, for offshore vessels, the deadrise angle must be even greater and is usually around 20° - 25° . Some very high speed offshore vessels use a deadrise in the afterbody as high as 30° [3]. This is done to soften the impact load on the hull after the boat jumps clear of the water and then slams back down onto the surface when at speed in excess of 50 knots.

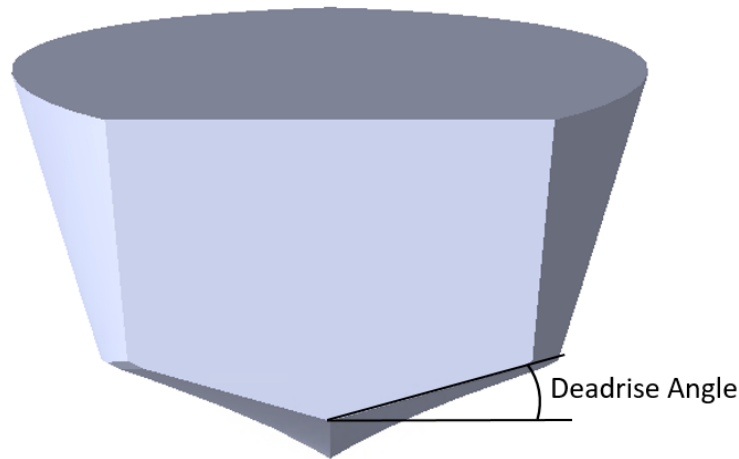


Figure 6. Example of Deadrise Angle

There have been several studies performed the effects of deadrise angle on the performance of high speed planing hulls. A study performed at Washington State University in 2014, tested the effects of negative deadrise angles. Although less popular than traditional V shaped hulls with a positive deadrise angle, vessels with a negative angle can be more beneficial for high loadings. The study tested both positive and negative deadrise hulls with an absolute value of 8° . The tests were performed with Froude Numbers between 1 and 5. The results showed that the water flow does not usually separate from vertical sides of the negative-deadrise hull. This caused an increase in the wetted surface area and friction drag. Even though there was more drag on the negative deadrise hull, the lift and lift-drag ratios were practically the same. Finally, the center of pressure and mean wetted lengths were slightly less on the negative deadrise hull [10].

Another study was performed by Rolla Research and tested deadrise angles between 0° and 15° . Tests were performed with different mesh refinements, and were verified using the Savitsky method. The major drawback to the Savitsky method is that it is only valid for monoedric hulls, so any variation in deadrise angle or beam cannot be taken into account even though most real world planing hulls are warped and have variable deadrise angles. The tests used a constant beam

of 0.3 m, used a fixed trim of 4° and transom draft of 0.045 m. The results showed that at low speeds, the Savitsky method underestimated the lift force. The lift and center of pressure were greater for the 0° hull than the 15° hull. Flat bottom hulls can produce more lift than traditional V shape hull on calm water, but are still not preferred due to their instability and high drag on rough water. The wave structure was also affected by the differing deadrise angle. At lower speeds, $F_r = 2$, a divergent wave was present at the bow and the flow sharply detached from the transom. At higher speeds, $F_r = 6$, there were no classical waves. A steep crest formed at the stagnation line. For the 0° hull, the crest was nearly vertical, while for the 15° case the crest was overturning. The differing wave geometry showed that more energy was expended in the formation of the wake for the 0° hull than those with larger deadrise angles [11]. The wave structure was far more vertical and had a sharper slope, resulting in more drag.

2.3 Effect of Chine

The chine is the sharp corner on the side of the hull. It is the intersection of the side and bottom of a ship and is shown in Figure 7. There are two traditional chine geometries. A hard chine is characterized by a sharp angular intersection, while a soft chine has a rounded corner. Each of these can also be a reverse chine, where the angle is pointed downward toward the surface of the water rather than away. A hard chine is designed to spray water to the sides and reduce the wetted surface area of a hull. A soft chine is a sharp turn not a corner. This gives a smoother ride but results in more drag [3]. A reverse chine pushes the spray back toward the surface of the water causing an increase in lift, eliminates most of the horizontal spray, and results in a very dry ride for the passengers.

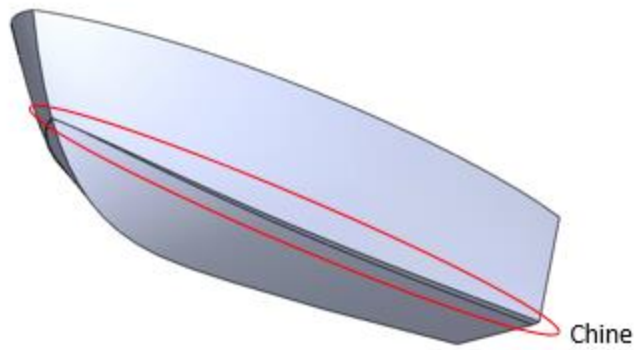


Figure 7. An Example of the Chine

One study that tested the effects of different geometries on hull performance was performed by the Fluid-Structure Interaction Research Group at University of Southampton. The study was done to determine the influence of hull design parameters on the performance of hard chine crafts. The study used six different models and were tested in a 200 m tow tank at GKN Westland Aerospace. Each of the models were tested in calm water at speeds from 4 to 12 m/s. The results showed that a stepped hull had a significant reduction in resistance as the speed increased, but the number of steps did not. Each of the other test parameters had no significant effect on the overall resistance. The study also found that there was no influence of transverse step on either the dynamic sinkage or trim [12].

Another study was performed at the University of Naples Federico in 2017. The tests were performed in the towing tank of the Naval Division of DII using scale models of the Naples Systematic Series hull. The length-to-beam ratios of the parent hull were varied for each model. The models were tested at $Re > 3.5 \times 10^6$, and at speed from $Fr = 0.5 - 1.6$. Each model was tested with and without interceptors along the bottom of the hull. The results showed that the hull efficiently was improved by interceptors, but only on models with high L/B ratios [13]. At intermediate Froude numbers, there was the greatest improvements in performance.

2.4 Effect of Spray Rails

Planing hulls use different geometric features to reduce drag and raise the hull out of the water. Hydrodynamic pressure on the bottom of the hull is a significant factor in raising the hull. Spray rails were designed to control the flow direction, increase the hydrodynamic lift on the hull, and reduce the trim angle. These triangular protrusions which run dead straight when viewed from the below, redirect the flow of water downward [14]. This increased the lift and reduces the wetted surface area. Figure 8 shows a spray rail on hull of a full scale boat.

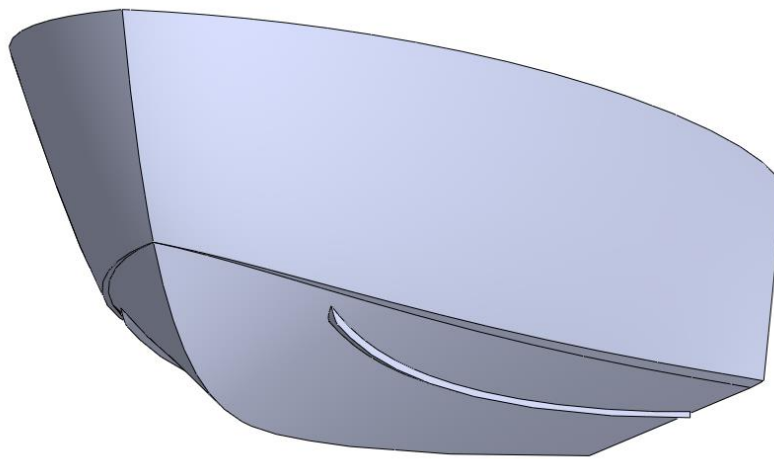


Figure 8. An Example of Spray Rails

A study performed by the Department of Naval Architecture and Ocean Engineering of South Korea in 2016 analyzed the effects of the spray rails on the total resistance and seakeeping of planing hulls. The test used 1/15 scale, 2 m long models and were tested in a 110 m tow tank at Seoul Nation University. The models had slender wave-piercing bows, round bilge, and small deadrise angle on stern. The wave piercing bow was used to reduce vertical motion in head sea by splitting the water rather than riding on top of surface. The models were tested at Fr from 0.416 to 4.158 to correspond to 5 to 50 knots on the full scale vessel. Each model was tested in calm water with a bare hull, then again with spray rails present. The test performed without spray rails present resulted in large trim angles causing the bottom of the hull to contact the water rather than the

sharp front edge of the bow. With the spray rails, the total resistance was decreased by 6.28% and the trim angles was reduced. As the speed of the ship increased, the location where the spray rails were functional became deeper in the water. When tested in head seas, the spray rails reduced both the pitch and heave motion, decreased the vertical acceleration, and increased the effective power [14]. This demonstrated the effectiveness of spray rails for drag reduction and seaworthiness.

2.5 Effect of Keel Line Depth

Traditional planing hulls have a smooth curve from the tip of the bow to flat portion on the bottom of the hull. This is known as the keel line and is shown in Figure 9. Traditionally, the majority of the keel line is above the water as the boat rides on top of the water. If the keel line goes deeper below the surface, the hull begins to cut through the water rather than ride on top. This is known as a wave piercing bow [14]. In some instances, the keel line can extend far below the traditional deepest point on a planing hull. This adds more resistance by not providing as much lift resulting in a larger wetted surface area. But they do have one distinct advantage, they provide a much better ride in head seas. Traditional planing hulls tend to jump out of the water when operating on rough water. This results in slamming which is very uncomfortable for the passenger and can damage the hull [15]. Wave piercing hulls cut through the waves and provide more stability.

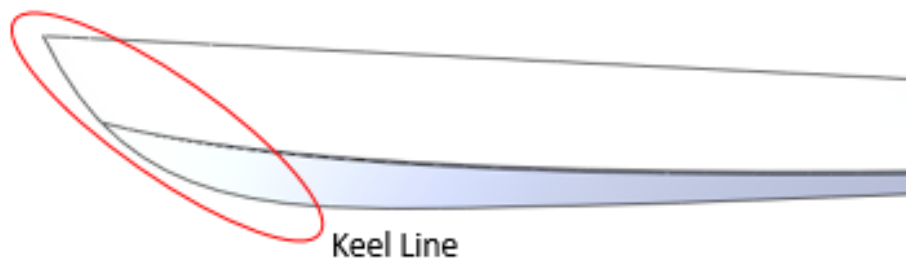


Figure 9. An Example of the Keel Line

A study performed by the Maritime & Ocean Engineering Research Institute in 2013 tested the effects of the keel line geometry on the total resistance of the hull. The tests were performed in a 117 m tow tank at Seoul National University. Three 1/6.5 scale models were created, each about 1 m in length. All three were hard chine planing monohulls, with a deep V design. The first model was a traditional planing hull while the other two were wave piercing. The tests were performed at speeds of 1.01 to 9.08 m/s or Fr 0.36 to 3.25 corresponding to 5 to 45 knots on the full size vessel. In calm water, the model with the shallowest keel line depth has the greatest lift and rose the furthest out of the water. The resistance was lowest for this hull and greatest for the hull with the deepest keel line. The hulls were then tested with head waves, with a wave amplitude of 0.02 m at a speed of 4.04 m/s or Fr 1.44. This corresponds to 0.26 m amplitude and 20 knots for a full size ship. The traditional hull showed a fly over phenomenon. This occurred when the boat left the surface of the water and slammed back into the water. The other two hulls did not come out of the water as they were able to cut through the waves more easily, with the deepest hull being the most stable [15]. This showed how simply reducing the drag cannot be the only objective when designing a hull. The vessel needs to have low resistance but also be stable and comfortable for the passengers.

2.6 Effects of Other Characteristics

There have been many other studies performed that have tested a variety of other drag reduction tools. A study performed at the University of California, Berkeley in 2014 tested the addition of tunnels on the performance of the Cougar Hull. The study used the CFD software FLUENT to solve for the flow and verifies the results with experimental data from literature and Savitsky's method. The original hull was modified to have two tunnels on the bottom, but kept the weight and center of gravity the same. The hulls were tested from Fr of 1 to 5.62 corresponding to

20 to 60 knots for the full size hull. The final results showed similar drags at low speeds, but at 60 knots there was a 14% reduction in drag [16]. Using Savitsky's method, there was only 2% discrepancy at 60 knots showing that the results were accurate.

The effects of a superhydrophobic grille was tested in a study performed at Dalian University of Technology in 2011. The concept was based on the water strider and used a material that repels water. This allowed the fluid to easily flow over the surface, reducing the skin friction drag. The grille was made of copper wires treated chemically with an ethanol solution of tetradecanoic acid. After a few hours in the solution at room temperature, the wires showed superhydrophobic properties. The tests were performed on flat bottom hulls made of a polyester polyurethane foam and had an outline size of 160×90×10 mm. Unlike most other studies which used a tow tank or CFD, this study used an open water circulation system. After the completion of the test, the hydrophobic hull showed a 78.9% reduction in drag when the moving at a velocity of 4.12 cm/s. There are two possible reasons of this significant reduction. The contact area between the hull and the water is very low, or the grille structure allows the water to pass more freely through the passages [17]. This shows the feasibility of using superhydrophobic materials to reduce drag.

The studies discussed in the literature review along with others were used to determine what geometric features would be tested in this paper along with what values would be used. A table of each study along with the relative information is shown in Table 1.

Table 1. Relevant Study Information

Year	Hull Profile	Vessel Type		Drag		CFD Simulation	Testing Type			Parametric Study				
		Displacement	Planing	Hull	Wake		Tow Tank Testing	Full Size Testing	Empirical Methods	Deadrise Angle	Chine Line	Hydrophobic Grille	Interceptors	
1	2014 Cougar Hull		x	x	x	x						x		
2	2013 None		x									x		
3	2007 None		x			x								
4	2011 Flat Bottom	x		x	x			x					x	
5	2009 None	x												
6	2017 Barge	x			x	x		x						
	DTMB5512													
7	2017 WIGLEY III	x		x	x	x								
8	2014 Custom Hull		x	x	x	x							x	
	America's Cup Yacht													
9	2004 Olympic Class Rowing Boat	x		x	x	x								
10	2014 Parametric Hulls		x										x	
11	2014 Narrow Hull		x		x	x							x	
	Athens Hull													
12	2015 Swede Ship Hull		x	x	x	x								
	Series 62													
	Series 65													
13	US Coast Guard 47ft Motor Lifeboat		x	x	x			x					x	
14	2011 None		x		x	x								
15	2012 None		x	x	x	x								
16	2017 C954		x	x	x	x								
17	2010 Series 62		x	x	x	x		x						x
18	2015 Prismatic Hulls		x	x	x	x								

3. CFD Theory

This study aimed to achieve its goals through the use of computational fluid dynamics (CFD). The study was performed using STAR CCM+ developed by CD Adapco. STAR CCM+ uses Reynolds Averaged Navier-Stokes Equations (RANS) to solve for flow fields. These equations are based on fundamental physical laws. These include the conservation of mass, Newton's Second Law of Motion, and First Law of Thermodynamics. Newton's Second Law and the First Law of Thermodynamics govern the conservation of momentum and the conservation of energy respectively. STAR CCM+ solves these governing equations through the use of a differential approach using Equation 13 with the control volume shown in Figure 10.

$$\frac{\partial \rho}{\partial t} + \nabla \cdot (\rho \mathbf{u}) = 0 \quad 13$$

The differential element has side lengths of δx , δy , and δz for x, y, and z directions respectively with the center of the fluid element is at position (x, y, z) . The volume of the element is $\delta x \delta y \delta z$. The velocity components at the center of the element for the x, y, and z directions are u, v, and w respectively. A systematic account for the changes in mass, momentum, and energy as it flows across the boundaries leads to the fluid flow equations. The first two terms in a Taylor Series Expansion are used to approximate the flow [18].

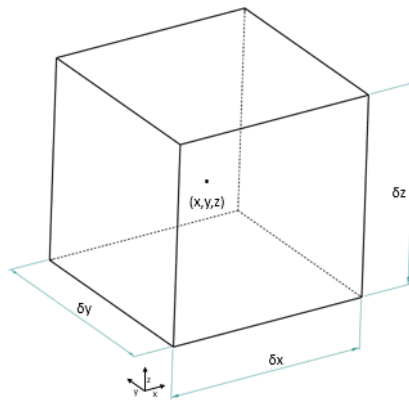


Figure 10. Control Volume used for Deriving Governing Equations

4.1 Conservation of Mass

The first equation is the conservation of mass. The general form of the equation is shown below.

$$\text{Rate of mass transfer} = \text{Mass flow in} - \text{Mass flow out} \quad 14$$

This is a scalar equation, meaning that the direction does not matter and only results in one equation. To derive the equation, the control volume shown in Figure 10 is used and the mass flow rate (\dot{m}) is equal to:

$$\dot{m} = \rho VA \quad 15$$

Where ρ is the density of the fluid, V is the velocity of the fluid, and A is the area of the control surface [18]. Using a Taylor series expansion, the velocity terms are expanded and added to the control volume with the mass flow in being in the positive x, y, and z directions, and the flow out being negative as shown in Figure 11. The velocities shown are multiplied by the differential areas. The total mass flow out is subtracted from total mass flow in, and then simplified. The final equation for the conservation of mass is shown in Equation 16.

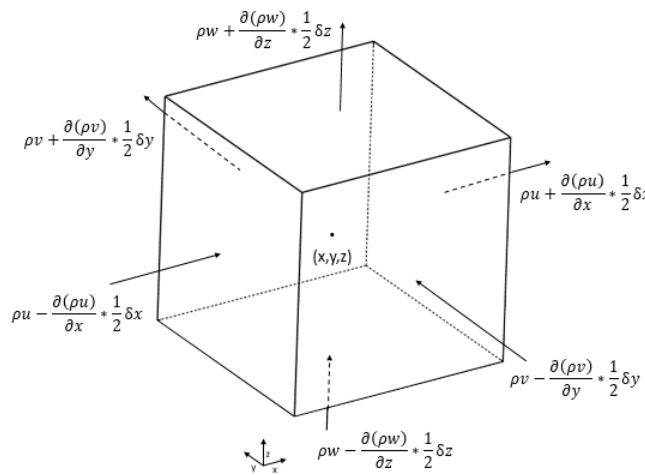


Figure 11. Conservation of Mass Differential Element

$$\frac{\partial \rho}{\partial t} + \frac{\partial(\rho u)}{\partial x} + \frac{\partial(\rho v)}{\partial y} + \frac{\partial(\rho w)}{\partial z} = 0 \quad 16$$

This equation can be simplified in several ways. If the model is steady, then there is no change in flow with time, then $d/dt = 0$. This is a very common simplification because it greatly decreases the computing time and power needed for the solution to converge. It is commonly done when analyzing the external flow around a car because the air speed is constant. Another simplification is if the flow is incompressible, meaning the density is also constant so $d\rho/dt = 0$. Liquids are considered to be incompressible along with air flow at low speeds. In reality, no flow is completely incompressible but in practice it can be ignored at speeds lower than Mach 0.3 or about 230 mph. The final simplification is if the flow is not three dimensional [18]. For these cases, the terms of any other dimensions are equal to zero and can be eliminated from the equation.

4.2 Conservation of Momentum

The second equation comes from the conservation of momentum. The general form of the equation is shown below.

$$\text{Sum of forces} = \text{Rate of momentum increase} \quad 17$$

This is a vector equation so each direction has an equation. This means that there are three separate equations [18]. The forces acting on the control volume are represented by equivalent stresses. The normal stresses act perpendicular to the surface and shear stresses act on the plane of the surface. The forces can be separated into surface forces and body forces. The surface forces acting on the control volume in one direction are shown in Figure 12. The forces were expanded using a Taylor series expansion and can be simplified to final equation for the x direction and is shown in Equation 18.

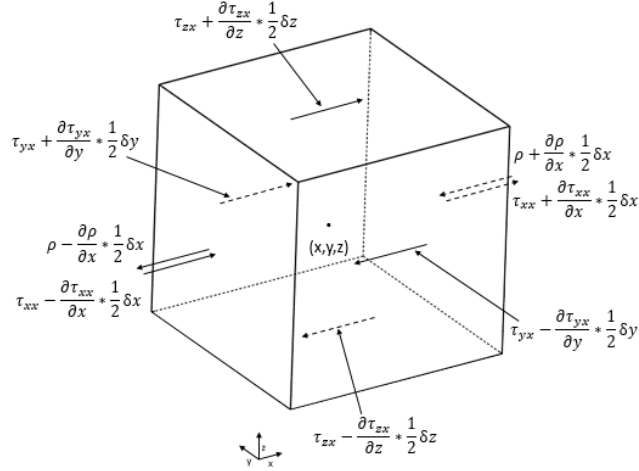


Figure 12. Shear Stress in only x-Direction

$$\rho \frac{Du}{Dt} = \frac{\partial(-p+\tau_{xx})}{\partial x} + \frac{\partial \tau_{yx}}{\partial y} + \frac{\partial \tau_{zx}}{\partial z} + S_{Mx} \quad 18$$

Each term in this equation represents a different set of forces. The left side of the equation represent the inertial forces. The first term on the right hand side represents the pressure forces, the next two are the viscous forces, and the final term is the body forces. The body forces are not part of the derivation, but still act on the fluid. These include gravity, centrifugal, Coriolis and electromagnetic forces [18]. This same process is applied to the other two directions and results in Equations 19 and 20.

$$\rho \frac{Dv}{Dt} = \frac{\partial \tau_{xy}}{\partial x} + \frac{\partial(-p+\tau_{yy})}{\partial y} + \frac{\partial \tau_{zy}}{\partial z} + S_{My} \quad 19$$

$$\rho \frac{Dw}{Dt} = \frac{\partial \tau_{xz}}{\partial x} + \frac{\partial \tau_{yz}}{\partial y} + \frac{\partial(-p+\tau_{zz})}{\partial z} + S_{Mz} \quad 20$$

These equations can be simplified similarly to the mass equation. If the flow steady, then there is no change over time and $d/dt = 0$. If the flow is incompressible, the density is constant so $dp/dt = 0$. Another simplification is if the inviscid. In this case the fluid viscosity is considered to be zero, so there is no shear stress. There are very few inviscid fluids, known as superfluids. The

only know superfluid is liquid helium. The final simplification is when the flow is not three dimensional, resulting in the terms in the unused direction being equal to zero [18].

4.3 Conservation of Energy

The final conservation law is the conservation of energy known as the first law of thermodynamics. The general form of the equation is shown below.

$$\text{Rate of change of energy} = \text{Heat added} - \text{Work done} \quad 21$$

This is a scalar equation so there are no components and only results in one additional equation. By applying the work done and heat added on each surface, the final equation for the conservation of energy can be derived and is shown in Equation 22.

$$\rho \frac{DE}{Dt} = \left[\frac{\partial(u(-p+\tau_{xx}))}{\partial x} + \frac{\partial(u\tau_{yx})}{\partial y} + \frac{\partial(u\tau_{zx})}{\partial z} \right] + \left[\frac{\partial(v\tau_{xy})}{\partial x} + \frac{\partial(v(-p+\tau_{yy}))}{\partial y} + \frac{\partial(v\tau_{zy})}{\partial z} \right] + \left[\frac{\partial(w\tau_{xz})}{\partial x} + \frac{\partial(w\tau_{yz})}{\partial y} + \frac{\partial(w(-p+\tau_{zz}))}{\partial z} \right] - \left[\frac{\partial(q_x)}{\partial x} + \frac{\partial(q_y)}{\partial y} + \frac{\partial(q_z)}{\partial z} \right] + S_E \quad 22$$

There are several other forms of this equation. By simply changing a couple of variables, this equation can be rewritten for kinetic energy, internal energy, enthalpy, and temperature [18]. In CFD, if the flow is assumed to be incompressible then there is no change in energy and so there is no need to solve the energy equation. This greatly simplifies the system of equations and greatly reduces the computing power necessary to solve for the flow.

4.4 Navier-Stokes Equations

While the conservation equations provide a solid base for the analysis, they fail to solve for the viscous shear stress components. These viscous stresses are related to the velocity gradients in the x, y, and z directions. This lead to the development of the Navier-Stokes equations. To use the equations several assumptions must be met. The fluid must be isotropic, so the viscous stresses

are not a function of direction. It must also be a Newtonian fluid so the viscous stresses are proportional to the strain rate [18]. The final equations for incompressible flow are shown in Equations 23, 24, and 25.

$$\rho \left(\frac{\partial u}{\partial t} + u \frac{\partial u}{\partial x} + v \frac{\partial u}{\partial y} + w \frac{\partial u}{\partial z} \right) = -\frac{\partial p}{\partial x} + \mu \left(\frac{\partial^2 u}{\partial x^2} + \frac{\partial^2 u}{\partial y^2} + \frac{\partial^2 u}{\partial z^2} \right) + \rho g_x \quad 23$$

$$\rho \left(\frac{\partial v}{\partial t} + u \frac{\partial v}{\partial x} + v \frac{\partial v}{\partial y} + w \frac{\partial v}{\partial z} \right) = -\frac{\partial p}{\partial y} + \mu \left(\frac{\partial^2 v}{\partial x^2} + \frac{\partial^2 v}{\partial y^2} + \frac{\partial^2 v}{\partial z^2} \right) + \rho g_y \quad 24$$

$$\rho \left(\frac{\partial w}{\partial t} + u \frac{\partial w}{\partial x} + v \frac{\partial w}{\partial y} + w \frac{\partial w}{\partial z} \right) = -\frac{\partial p}{\partial z} + \mu \left(\frac{\partial^2 w}{\partial x^2} + \frac{\partial^2 w}{\partial y^2} + \frac{\partial^2 w}{\partial z^2} \right) + \rho g_z \quad 25$$

4.4 Turbulence Modeling

Turbulence is characterized by three dimensional irregular flow. It is a random state of motion where velocity and pressure are changing with time. The flow typically contains rotational eddies that vary in three dimensions. Even flow where the mean velocity and pressure only vary in one or two dimensions, still have turbulent fluctuations in three dimensions [19]. The most common turbulence models use a Reynolds decomposition for the instantaneous velocities and pressures. These values are then inserted into the Navier-Stokes equations given in Equations 23, 24, and 25. The result is the Reynolds Averaged Navier-Stokes (RANS) Equation [18] and can be written as:

$$\bar{u} \frac{\partial \bar{u}}{\partial x} + \bar{v} \frac{\partial \bar{v}}{\partial y} + \bar{w} \frac{\partial \bar{w}}{\partial z} = -\frac{1}{\rho} \frac{dp}{dx} + \nu \left(\frac{\partial^2 \bar{u}}{\partial x^2} + \frac{\partial^2 \bar{u}}{\partial y^2} + \frac{\partial^2 \bar{u}}{\partial z^2} \right) - \left(\frac{\partial \overline{u'^2}}{\partial x} + \frac{\partial \overline{u'v'}}{\partial y} + \frac{\partial \overline{u'w'}}{\partial z} \right) \quad 26$$

The RANS equation solves for eleven unknowns. Five are related to flow properties, and the other 6 are Reynolds stresses. The software solves for mean flow then adds the effects of turbulence. Although RANS is a powerful tool, it alone is unable to achieve the desired results. The two-equation turbulence models, k- ϵ and k- ω , use two additional transport equations to describe the turbulent viscosity [19]. The standard k- ϵ model developed by Launder uses Equation

27 to determine the turbulent viscosity (μ_t) based on the turbulent kinetic energy (k) and dissipation (ε). The transport equations [20] are shown in Equations 28, and 29.

$$\mu_t = C_\mu \frac{k^2}{\varepsilon} \quad 27$$

$$\frac{\partial \rho K}{\partial \tau} + \frac{\partial \rho U_j K}{\partial x_j} = \frac{\partial}{\partial x_j} \left[\left(\mu + \frac{\mu_t}{\sigma_k} \right) \frac{\partial K}{\partial x_j} \right] + P_k + G_k - \rho \varepsilon \quad 28$$

$$\frac{\partial \rho \varepsilon}{\partial \tau} + \frac{\partial \rho U_j \varepsilon}{\partial x_j} = \frac{\partial}{\partial x_j} \left[\left(\mu + \frac{\mu_t}{\sigma_\varepsilon} \right) \frac{\partial \varepsilon}{\partial x_j} \right] + C_{\varepsilon 1} (P_k + C_{\varepsilon 3} G_k) \frac{\varepsilon}{K} - C_{\varepsilon 2} \rho \frac{\varepsilon^2}{K} \quad 29$$

Where σ_k , σ_ε , $C_{\varepsilon 1}$, $C_{\varepsilon 2}$, $C_{\varepsilon 3}$, and C_p are model constants with their values shown in Table 2. P_k is the production of turbulent kinetic energy, modeled using a Boussinesq approximation, and is shown in Equation 30.

Table 2. k- ε Turbulence Modeling Constants [20]

σ_k	σ_ε	$C_{\varepsilon 1}$	$C_{\varepsilon 2}$	$C_{\varepsilon 3}$	C_p
1	1.3	1.44	1.92	0-1.0	0.09

$$P_k = \rho \overline{u_i u_j} \frac{\partial U_t}{\partial x_j} \quad 30$$

The standard k- ε model is robust and produces accurate results for free flow with small pressure gradients and flow close to the walls, but has poor performance with large separation regions such as behind a ship. This leads to the need for an additional turbulence model. The k- ω model developed by Wilcox uses Equation 31 to relate the turbulent kinetic energy and specific dissipation (ω) to the turbulent viscosity. This is very similar to the k- ε model. The transport functions [21] are shown in Equations 32 and 33.

$$\mu_t = \frac{\rho k}{\omega} \quad 31$$

$$\frac{\partial(\rho k)}{\partial t} + \frac{\partial(\rho u_j k)}{\partial x_j} = P - \beta^* \rho \omega k + \frac{\partial}{\partial x_j} \left[\left(\mu + \sigma_k \frac{\rho k}{\omega} \right) \frac{\partial k}{\partial x_j} \right] \quad 32$$

$$\frac{\partial(\rho\omega)}{\partial t} + \frac{\partial(\rho u_j \omega)}{\partial x_j} = \frac{\gamma\omega}{k} P - \beta\rho\omega^2 + \frac{\partial}{\partial x_j} \left[\left(\mu + \sigma_\omega \frac{\rho k}{\omega} \right) \frac{\partial \omega}{\partial x_j} \right] \quad 33$$

Where σ_ω , σ_k , β^* , β , and γ are model constants with the values shown in Table 3. The standard k- ω model can accurately describe the flow in large separation regions, but may have errors close to the walls. Both the k- ω and k- ϵ models have distinct advantages and disadvantages. This lead to the development of a final turbulence model.

Table 3. k- ω Turbulence Modeling Constants [21]

σ_ω	σ_k	β^*	β	γ
0.5	0.5	0.09	3/40	5/9

The shear stress transport (SST) k- ω model developed by Menter uses both the traditional k- ω and k- ϵ models. The k- ω SST combines both other models into one blending function. It uses k- ϵ near the walls and in the fully developed flow, while k- ω is used in the outer boundary layers and separation regions [22]. The k- ω SST is used in a variety of complex flows and is recognized as one of the best turbulence models for ship hydrodynamics.

4.5 Multiphase Flow

To simulate a ship moving in the water, the model must incorporate both water, air, and the boundary between them. There are several multiphase models that can accurately track the interaction. Some track the surface directly while others track the phases then reconstruct the interface. The most common method to capture the free surface and analyze ship hydrodynamics is the volume of fluid (VOF) method. For this method, each phase is tracked and marked with a color function (γ) known as the volume fraction. If there is only one phase, then γ is 1 or 0. If so the standard Navier-Stokes equation is solved. If γ is in between 0 and 1, as at the interface, then phase properties are averaged to get a single function. The average density and viscosity are found

using Equations 34 and 35. Then a modified Navier-Stokes is used with the averaged fluid properties [23] as shown in Equation 36.

$$\rho = \gamma\rho_1 + (1 - \gamma)\rho_2 \quad 34$$

$$v = \gamma v_1 + (1 - \gamma)v_2 \quad 35$$

$$\frac{\partial U_i}{\partial t} + U_j \frac{\partial U_i}{\partial x_j} = -\frac{1}{\rho} \frac{\partial P}{\partial x_i} + \nu \frac{\partial^2 U_i}{\partial x_j^2} + g_i + S_{i,s} \quad 36$$

This equation has an additional source term that accounts for the moment exchange across the interface due to surface tension forces. The final surface is found using Equation 37.

$$\frac{\partial \gamma}{\partial t} + U_i \frac{\partial \gamma}{\partial x_i} = 0 \quad 37$$

The VOF method is not the most robust as other methods, but it provide accurate solutions and is less computational demanding

4.6 Fluid Structure Interaction

To simulate the dynamic motion of a hull before reaching equilibrium, fluid structure interaction (FSI) between the hull and fluids occurs and must be simulated. This is achieved by solving the equations of motion for the vessel. In general, there are six possible degrees of freedom (DOF): three translational and three rotational. Translation in the x, y, and z directions are known as surge, sway, and heave respectively, while rotations in x, y, and z are roll, pitch, and yaw. For a ship, the most common types of motion are known as sinkage and trim. Sinkage is heave motion and can be described as how the hull moves perpendicular to the surface of the water. Trim is a pitch rotation and is the angle of the hull in the water. Translational motion is governed by Newton's second law, and is shown in Equation 38 where F_{net} is the net force on the hull, m is the total mass and U is the velocity. For rotational motion, Equation 39 is used where τ_{net} is the net torque, ω is the angular velocity, and I is the inertia tensor shown in Equation 40.

$$m \frac{d\vec{U}}{dt} = \vec{F}_{net} \quad 38$$

$$\mathbf{I} \frac{d\vec{\omega}}{dt} + \vec{\omega} \times (\mathbf{I} \cdot \vec{\omega}) = \vec{\tau}_{net} \quad 39$$

$$\mathbf{I} = \begin{bmatrix} I_{xx} & I_{xy} & I_{xz} \\ I_{yx} & I_{yy} & I_{yz} \\ I_{zx} & I_{zy} & I_{zz} \end{bmatrix} \quad 40$$

STAR CCM+ offers several different methods for determining the dynamic motion of bodies being acted upon by fluid flow. One the better methods is the 6 DOF Dynamic Fluid Body Interaction (DFBI). It uses forces and moments to compute the translation of the center of mass and the angular rotation about the former. It accomplishes this through the use of a second order trapezoidal scheme that solves for the equilibrium. At a time step, the software calculates the different forces acting on the body. The body is then moved to its new position. The body stays in this new position until STAR CCM+ reaches a force and moment tolerance or the max inner time step is achieved. At this point the forces are triggered to act and the body moves to the next position. The software uses an iterative process to solve for the position and is shown in the flow chart in Figure 13. This process is continued until the body reached equilibrium and the net forces are zero [24]. Once the body reaches equilibrium, the final position of the hull will have been achieved.

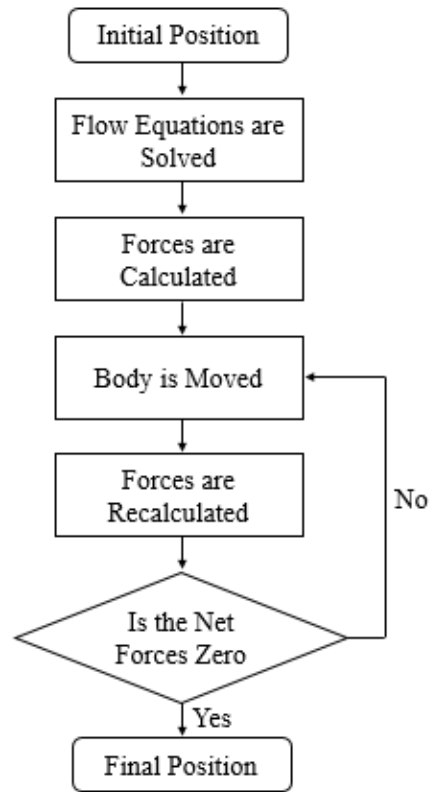


Figure 13. Flow Chart used to Describe Iterative Process

4. Methodology

The goal of this study was to analyze the effects of different geometric features on the performance of high speed planing hulls. The criteria being tested for was the total drag, trim angle, and sinkage. This included viscous drag, wave making drag, and air resistance. The hull being tested was designed using dimensions based on traditional planing hulls used on inland lakes. The study was broken into three phases with the overall goals as follows.

- Develop a CFD model for planing hulls
 - Obtain the resistance curve for the base hull
 - Perform a mesh validation study
- Validate simulation using experimental data from a scale model tested in a towing tank
- Study effect of keel line geometry, spray rail location, and deadrise angle on the hull drag
- Determine the best hull configuration for drag reduction on the hull at high speed

The first phase of the study was to develop a fully functional CFD stimulation for the base hull. The simulation tested for the different forces and moments on the hull, then adjusted the position of the hull. It determined the total hull resistance. The goal was to obtain the entire resistance curve and analyze the effectiveness of the simulation. A mesh dependency was performed to ensure that the results were independent of the mesh size and were accurate. The next phase of the study was to verify the CFD results using experimental data. A scale model was created and then tested in the towing tank located in the GVSU's fluids lab. Due to the small size of the tank and the relatively low testing speeds, the model was relatively small with a total length of 9 in at a scale of 1:33.33. The models was tested at various speeds corresponding Froude

Numbers used in the CFD simulation. Using the experimental results, the CFD simulation was validated and proven to be correct.

The final phase of the study was to test the effects of different geometric features on the overall performance. The features being tested were the deadrise angle, the keel line depth/geometry, and the location of spray rails. The geometric test values are shown in Table 4 and visualizations of each are shown in Figure 14, Figure 15, and Figure 16. Each of the geometric features were changed from the base hull without changing any other features. The mass, center of gravity, and moment of inertia remained the same for each test to ensure consistent results. For each feature, several different values and locations were tested. Each feature was first tested individually, and then using a DOE analysis with a full 2x2x3 factorial design. A combination of the best geometric features was used to determine the best configuration. The goal of this stage is to determine the best hull geometry to reduce the total drag on the hull at high speeds.

Table 4. Hull Geometry Test Parameters

	Chine Height (in)	Deadrise Angle (deg)	Keel Line Depth Relative to Base (in)	Spray Rail Location (% of Surface from Medial Edge)
Base Hull	12	15.6	0	NA
Minimum Value	9	9.09	-10	30
Maximum Value	15	21.8	10	60

Each of these phases helped toward achieving the final goal of the study. The results of each part determined the direction going forward and provided the necessary evidence to continue to the next part of the experiment.

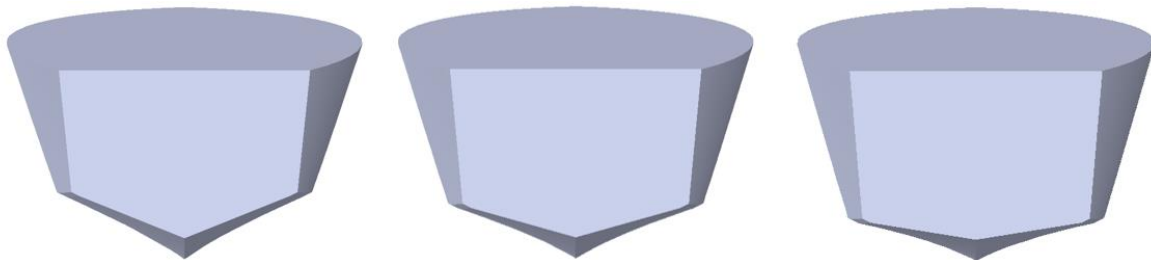


Figure 14. Visualization of Deadrise Angle Changes

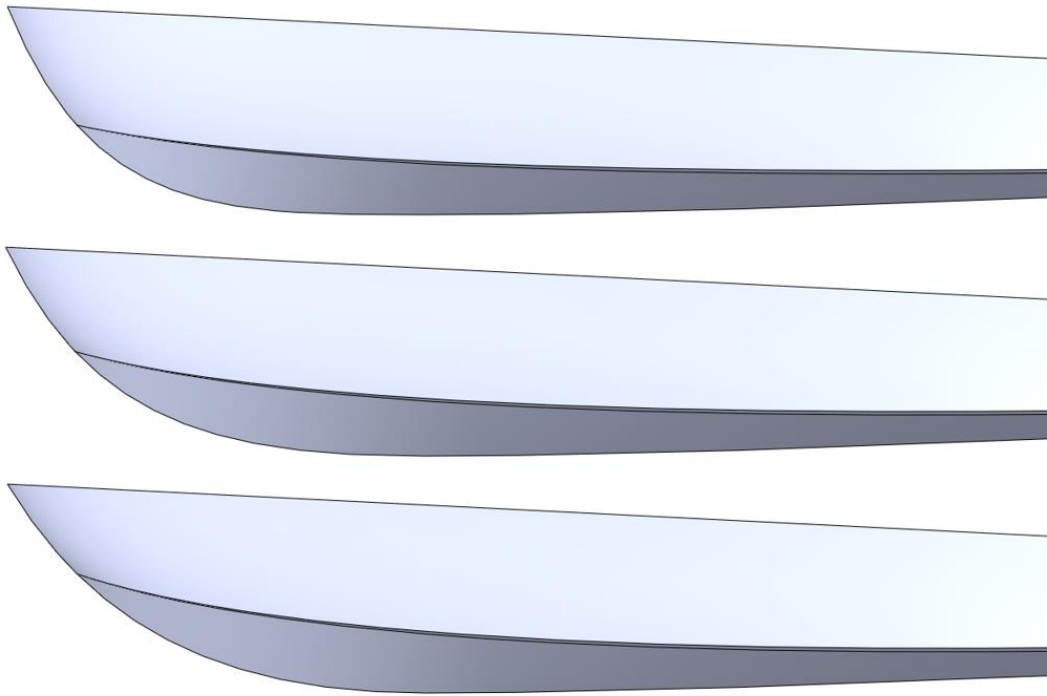


Figure 15. Visualization of Keel Line Geometry Changes

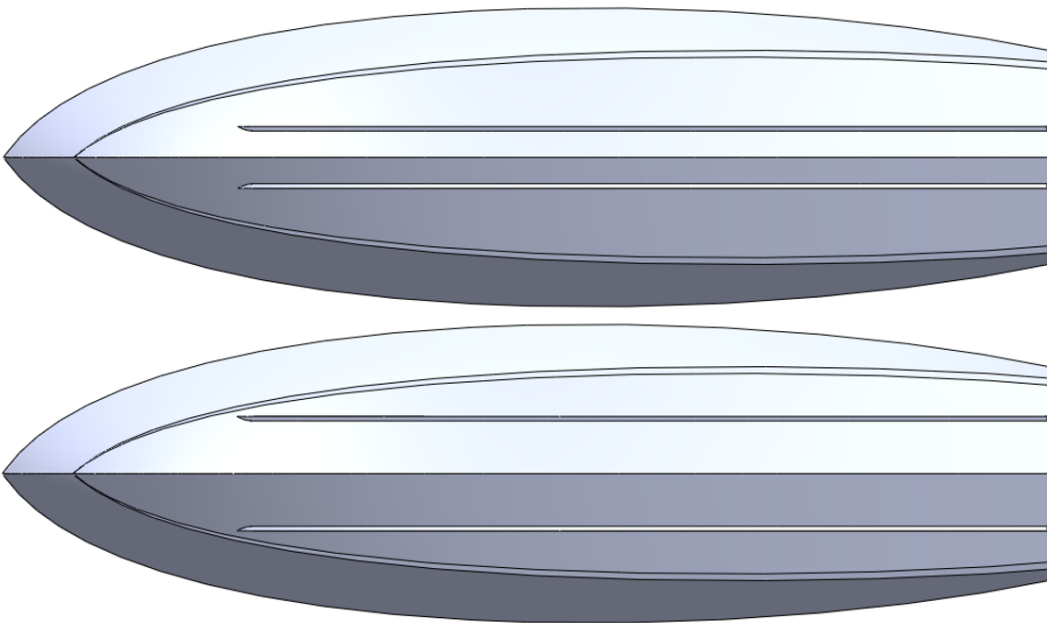


Figure 16. Visualization of Spray Rail Location Changes

5. Phase I: Base Hull Simulation

The goal of the first phase of study was to create an accurate CFD simulation for a planing hull. The simulation required a CAD model, physics model, mesh model, and boundary conditions. The CAD model had to accurately capture the geometry of a real planing hull. The mesh model had to be independent and not affect the final results for position, trim angle, and total drag. To achieve this, several different mesh refinements were performed until there was less than 5% difference for the drag, sinkage, and trim. With the refined mesh, the base hull was tested at various speeds in order to examine the hull's performance.

5.1 CFD Model

Creating a CFD simulation required several different types of models. The CAD model was the actual geometry used in the simulation. It was composed of the hull, overset region, and the far field. The CAD models were used to create a mesh that the simulation could use. The model's surfaces were recreated using a surface mesh to accurately capture the shape of each feature. The space around the body was where the fluids actually flowed. This area was filled with the volume mesh. CFD software uses a mesh to solve the flow equations using the finite element approach. A finer mesh results in a more accurate the flow but requires far more computation time. The physics model described what equations were used and what simplifications were made. Finally, the boundary conditions described what happened at the edges of the simulation and on the surface of the CAD model.

5.1.1 CAD Model

The CAD model used in this study was designed from scratch using a parametric scheme outlined by Pérez-Arribas in 2014 [25]. The three dimensional center, sheer, and chine lines were

created using a combination of two dimensional B-splines in both the lateral and plan views. The hull's surfaces were then lofted from the boundary curves. The basic dimensions for the hull were common for 25 ft planing hulls [26] [27] and are shown in Table 5. Figure 17 shows the model used in the simulation. It was simplified form real vessel. This was done to reduce the complexity of the model and significantly reduce the computation time. The simplifications included removing the passenger areas, motor, side rails, and then simplifying these areas with flat geometry.

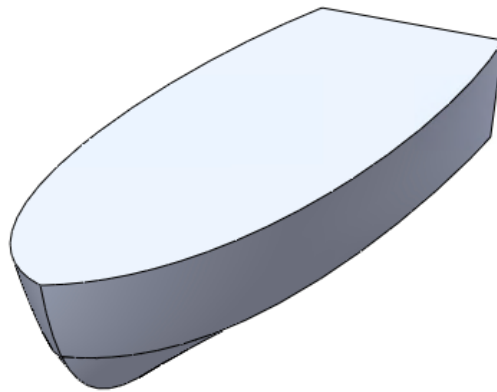


Figure 17. CAD Model

Table 5. Hull Dimensions

Length	25 ft	7.62 m
Beam	7.1 ft	2.16 m
Depth	5.0 ft	1.52 m
Chine Height	7.0 in	0.18 m
Waterline Length	24.7 ft	7.51 cm
Wetted Surface Area	392.6 ft ²	36.5 m ²
Deadrise Angle	15.6 deg	

The hull was 25 ft in length with a beam of about 7 ft. These dimensions are common for vessels designed to operate on small in land lakes [26] [27]. The hull geometry is shown in Figure 18, 19 and 20 with the detailed drawing being in Appendix A. The base hull had a hard chine with a small chine flat used to redirect the flow of water away from the vessel. This reduced the wetted

area and thus the drag. The boat had a deadrise angle of 15.6° at the aft with a slight twist toward the bow.

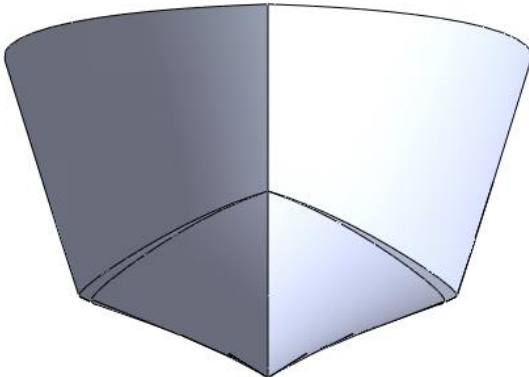


Figure 18. CAD Model Front View

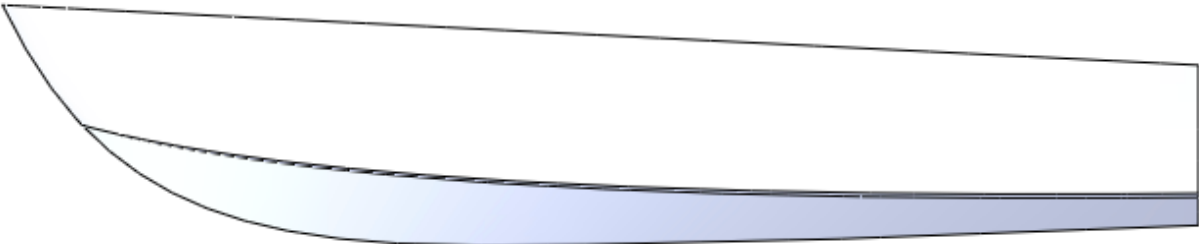


Figure 19. CAD Model Side View

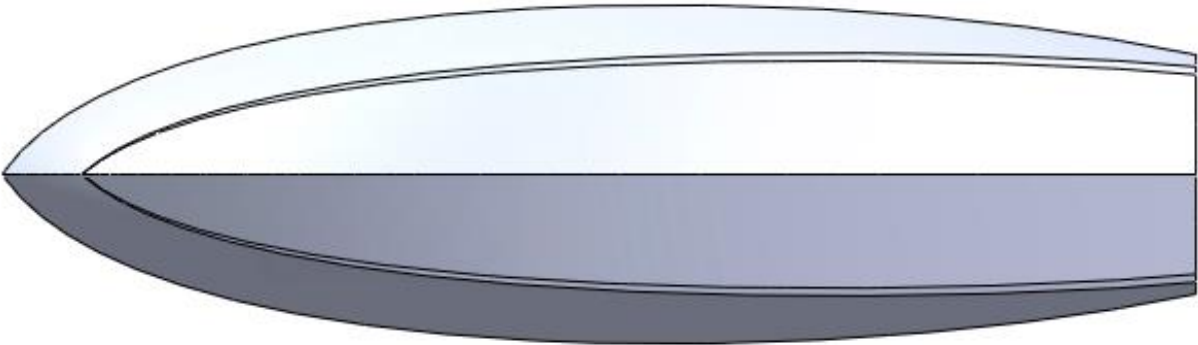


Figure 20. CAD Model Bottom View

For the CFD simulation, other geometric features were required to properly determine the motion of the hull and the final equilibrium location. These included the mass, center of mass, and moment of inertia. Table 6 contains these values while Figure 21 shows the location of the center

of mass. The total mass was obtained from the scale model hull tested in the towing tank. The value was scaled up to the full size hull. The center of mass was estimated using the relative location from existing hulls [19]. The moment of inertia was found using a solid modeling software and the defined center of mass.

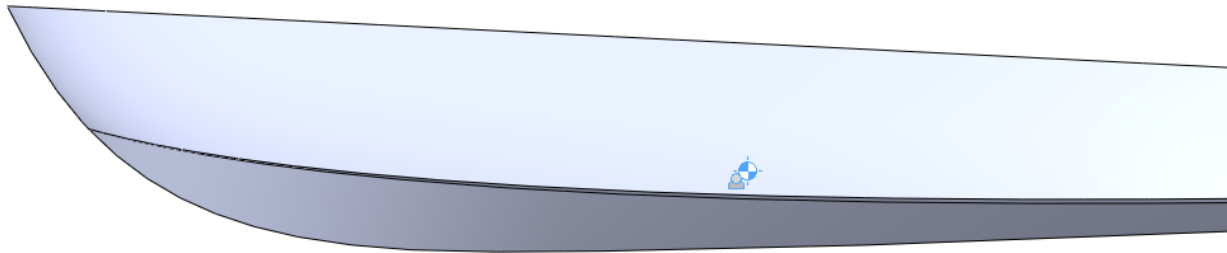


Figure 21. Center of Mass

Table 6. Hull Mass Features

Full Hull	Mass (kg)	6000		
	Center of Mass (m)	x	y	z
		-3	0	0.5
	Moment of Inertia (kg m ²)	lxx	lyy	lzz
		2400	25800	26400
Off Diagonal (kg m ²)	lxy	lxz	lyz	
	0	1200	0	
Half Hull	Mass (kg)	3000		
	Center of Mass (m)	x	y	z
		-3	0	0.5
	Moment of Inertia (kg m ²)	lxx	lyy	lzz
		1200	12900	13200
Off Diagonal (kg m ²)	lxy	lxz	lyz	
	0	600	0	

For the simulation, symmetry was used to further simplify the geometry. The hull was split down the center and only half of the hull was used. This greatly reduced the total number of elements, and the computation time. The final simulation geometry is shown in Figure 22. This could be done because the flow was roughly symmetrical along the central plane.

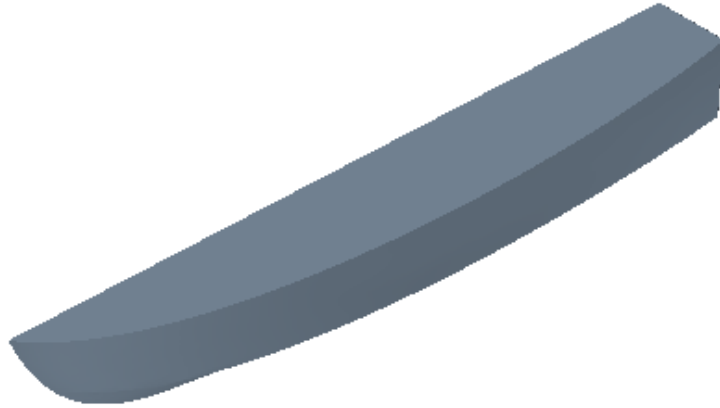


Figure 22. Final Simulation Geometry

In addition to the hull geometry, the simulation had two other geometric features. The first was the overset region. This was a volume that moved with the hull relative the surface of the water and the rest of the far field. This region was needed to accurately simulate the hull motion by providing a second region that could contain a separate mesh. The overset region is shown in Figure 23 with the dimension in Table 7.

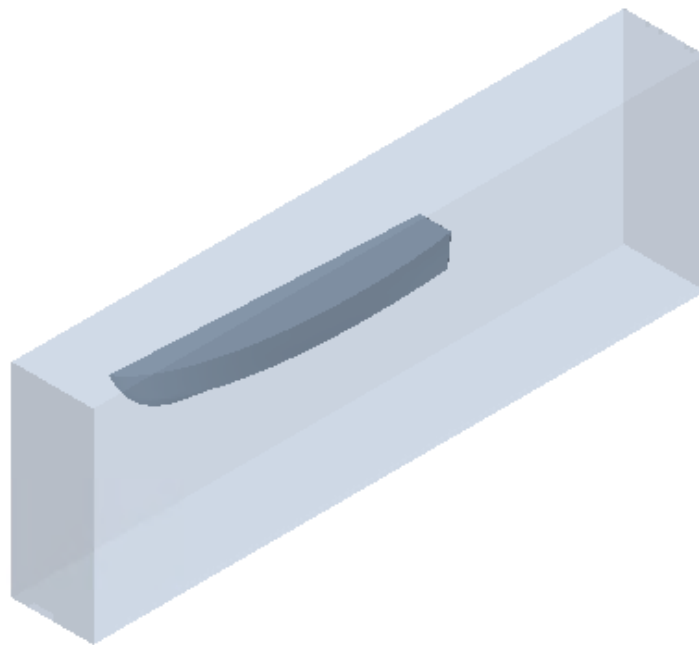


Figure 23. Overset Region

Table 7. Overset Dimensions

	Numerical Value (m)	Ratio to Boat
Lenth	15	1.97
Width	2	1.85
Depth	5	3.28

The final geometry was the far field. This region contains everything in the simulation. The far field is shown in Figure 24 while the dimensions are in Table 8. In order to have good results, the domain must be far larger than the tested geometry. Each of the far field dimensions were at least 10x those of the hull [18]. This ensures that boundaries do not affect the flow around the hull.

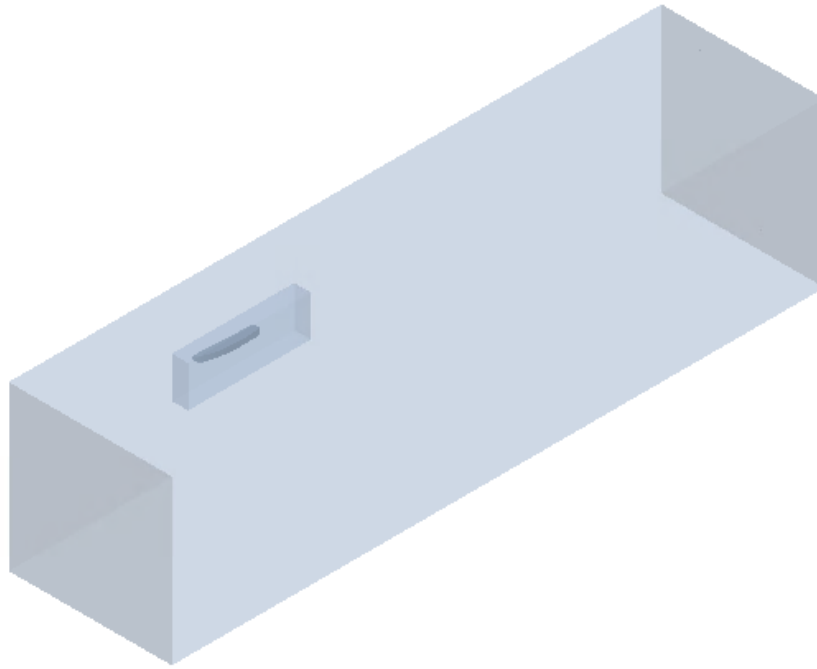


Figure 24. Simulation Far Field

Table 8. Far Field Dimensions

	Numerical Value (m)	Ratio to Boat
Length	80	10.50
Width	20	18.53
Depth	20	13.12
Air Depth	10	6.56
Water Depth	10	6.56

5.1.2 Physics Model

The physics model used in the simulation are shown below.

1. **Space** – Three Dimensional
2. **Time** – Implicit Unsteady
3. **Material** – Eulerian Multiphase
 - a. Multiphase Interaction

The simulation was three dimensional because a 3D model was tested. Other CFD simulations can be tested in 2D such as airfoils. An implicit unsteady model was used because the hulls position relative to the water was dependent on the velocity of the fluid. This meant that the hulls position was not time independent so a steady state model could not be used. A time-step of 0.005 seconds with 10 inner iterations per time-step was used to accurately determine the flow. Because modeling a boat required both water and air, a multiphase physics model was used.

4. **Eulerian Multiphase Mixture** - Volume of Fluid (VOF)
 - a. Multiphase Equation of State
5. **Flow** – Segregated Flow
 - a. Gradients

The VOF model is the preferred model for marine applications as it uses the standard Navier-Stokes equations when only one phase is present, and used a modified equation with averaged properties when more than one phase is present. This model is able to accurately represent the surface of the water and the interactions involved. Segregated flow was used because both fluids behave as incompressible, so there was no need to solve the energy equation. Although air is considered to be compressible at any speed, the effects were minimal as the test speeds were relatively low. If the air speeds had been increased past Mach 0.3 [18], the coupled flow would

have been used and the energy equation would have been solved. Using segregated flow greatly reduced the computational time for each simulation.

6. **Viscous Regime** – Turbulent
 - a. Reynolds-Averages Navier Stokes
7. **Reynolds-Averages Turbulence** – K-Omega Turbulence
 - a. SST K-Omega
 - b. Exact Wall Distance
 - c. All y + Wall Treatment
8. **Optional Models**
 - a. Gravity
 - b. Cell Quality Remediation
 - c. VOF Waves

A turbulent model was used because turbulence would be present in the simulation. Laminar flow can only be used at low speeds and with smooth bodies. The laminar flow physics model can only calculate laminar flow, while the turbulent model can be used for both laminar and turbulent flow. The SST K-Omega turbulence was used because it incorporated both the standard k- ϵ and k- ω models. The k- ϵ model performs well with small pressure gradients and close to the walls, while the k- ω captures the flow in large separation regions far better [22]. The SST K-Omega used both models and produced more accurate results.

The two phases present in simulation were liquid water and air with the boundary between being defined by flat waves VOF waves. This allowed for the capture of the wake created by the hull as it moved through the water. To determine the motion of the boat, DFBI motion was used with 2 degrees of freedom: translation in the z and rotation in the y. The translation captured the

sinkage as the hull moved vertically in the water, while the rotation captured the trim angle as the hull rotated. For DFBI, a release time and ramp time were used to reduce the oscillations from sudden changes in the flow cause by the motion [24]. The release time was set to 0.5 seconds while the ramp times was 5 seconds. The mass and moment of inertia of the hull were specified based on half of the geometry through the use of symmetry.

5.1.3 Boundary Conditions

The boundary conditions used in the simulation were velocity inlet, pressure outlet, symmetry plane, overset mesh, and wall. The surfaces of the boat hull were all set to the wall boundary condition. The front, top and bottom of the far field were set as a velocity inlet, the back was a pressure outlet, and both sides of the virtual tow tank were symmetry plans. The final boundary condition was an overset mesh. This was at the boundary between the moving domain and the stationary far field. At each of the far field boundaries, wave damping was enabled to prevent any interference. Figure 25 shows the boundary conditions used on the simulation.

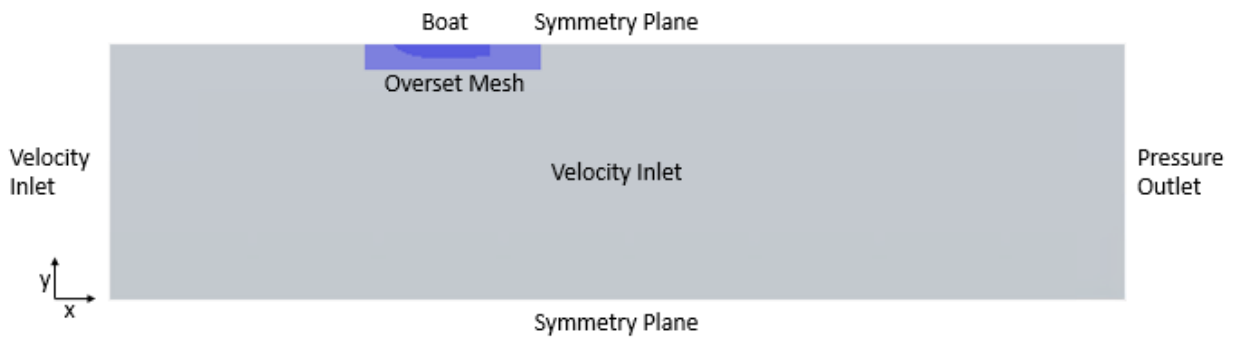


Figure 25. Boundary Conditions Used in the Simulations

5.1.4 Mesh Model

The mesh models used in the simulation were surface remesher, trimmed cell mesher, and prism layer mesher. Because the far field did not contain the hull, no prism layers were needed, so

that model was removed. Four different meshes were tested and the reference values are shown in Table 9.

Table 9. Tested Mesh Values for Convergence Study

	Mesh 1		Mesh 2		Mesh 3		Mesh 4	
	Far Field	Overset						
Base Size (m)	5	2	5	2	5	2	5	2
Target Surface Size (%)	100	25	100	25	100	25	100	25
Minimum Surface Size (%)	10	0.5	10	0.5	10	0.5	10	0.5
Surface Curvature (# Points / Circle)	100	200	100	200	100	200	100	200
Surface Growth Rate	1.3	1.3	1.3	1.3	1.3	1.3	1.3	1.3
Number of Prism Layers	NA	10	NA	10	NA	10	NA	20
Prism Layer Stretching	NA	1.5	NA	1.5	NA	1.5	NA	1.2
Prism Layer Thickness (%)	NA	3	NA	3	NA	3	NA	5
Volumetric Control 1 (%)	16	16	8	8	4	4	3	3
Volumetric Control 2 (%)	16	16	8	8	4	4	3	3
Volumetric Control 3 (%)	8	8	4	4	2	2	1.5	1.5
Number of Cells	213490		423509		1902394		2706977	

The surface mesh was the same for each simulation and is shown in Figure 26. This mesh was fairly well defined and accurately captured the geometry of the hull. The mesh was more defined toward the bow because there was more curvature and thus needs more elements to accurately capture the geometry.

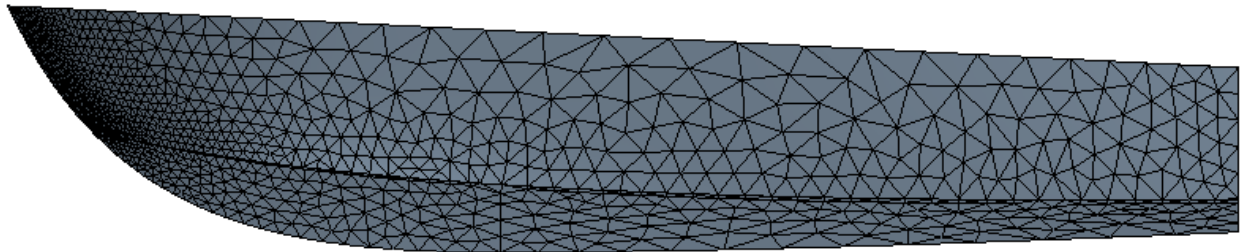


Figure 26. The Surface Mesh

The different volume mesh used in the simulation is shown in Figure 27. For each simulation, three volumetric mesh controls were used to refine the volume mesh. The first encompassed the wake region. The second was anisotropic region at the water's surface where

only the z component was refined. This was intended to help capture the multiphase fluid interaction. The final region was around the hull to better capture the flow around the body.

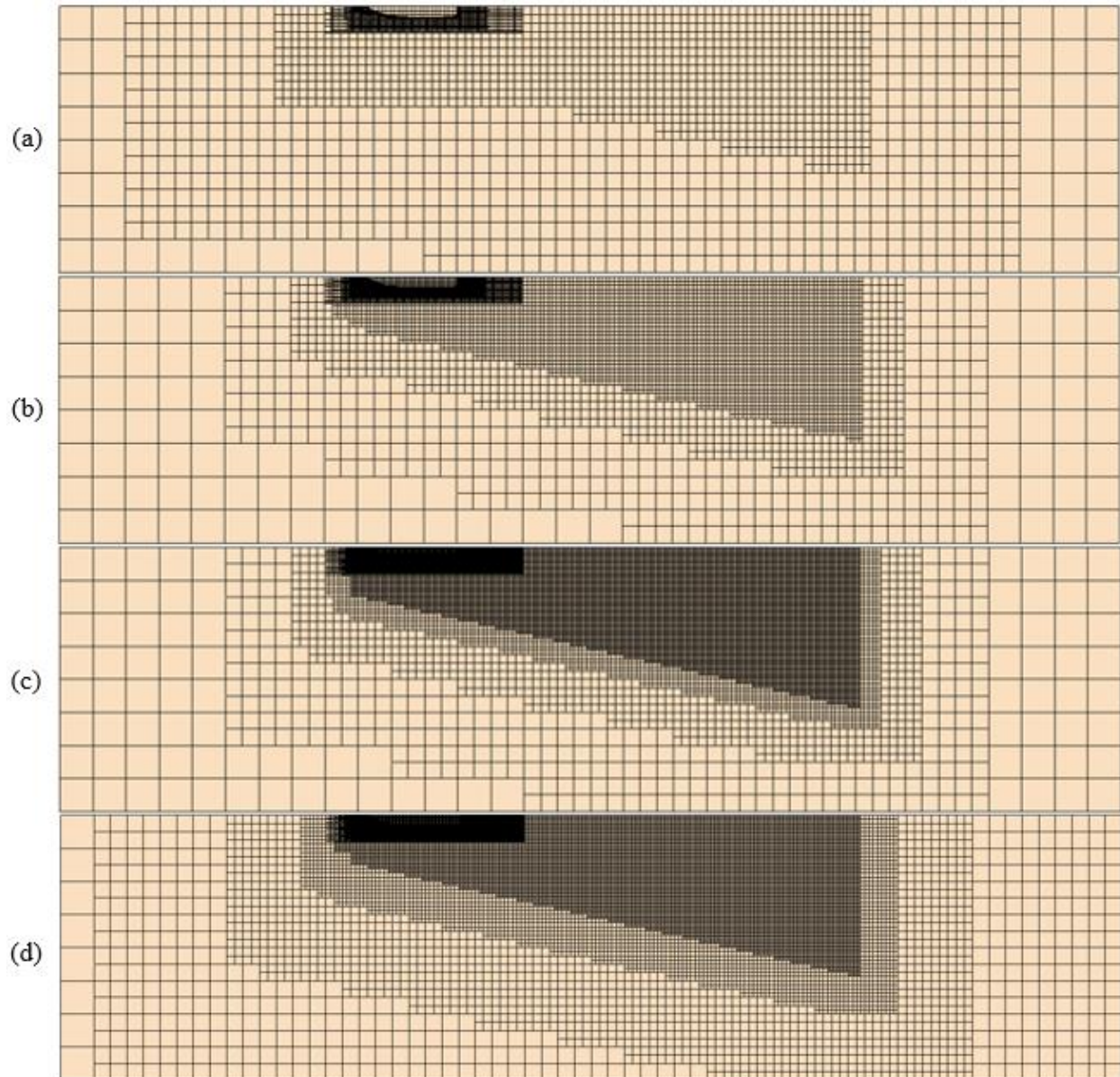


Figure 27. The Tested Volume Mesh with (a) 213,490 Cells, (b) 423,509 Cells, (c) 1,902,394 Cells, and (d) 2,706,977 Cells

The final mesh region was the overset mesh. The overset region used in STAR CCM+ was designed for use when two separate meshes are overlapped. One mesh was stationary, while the other was free to move with the moving body. The mesh was able to both translate and rotate. This

method ensured that the cells maintained their shape while motion occurs. The cells at the interface between the two regions were identified and labeled as donor cells. The cells in background that were closest to the donor cells became acceptor cells. The acceptor cells formed a continuous layer around the overset region, and were used to transfer information between the two regions. Any cell in the background that were completely covered by the overset region became inactive. The main advantage to this method was that only a small portion of the cells are moving. This reduced the error from cell distortion and recalculation. The drawback was that the interpolation between the two mesh regions can be time consuming [24]. The overset mesh used in the simulation is shown in Figure 28.

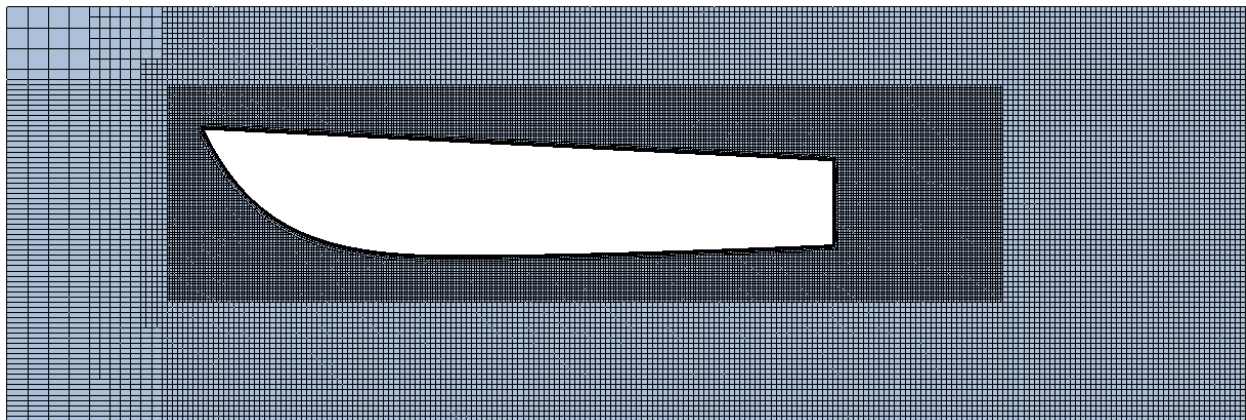


Figure 28. The Overset Mesh

5.2 Phase I Results

Acquiring accurate results that were independent of the mesh required several different iterations. Each simulation used the same geometry, physics, and boundary conditions. Each test was performed at 10 m/s, the results of each simulation were recorded, and the percent difference between each trial were calculated. The percent difference for the total drag, sinkage, and trim angle were all determined and after each value was below 5%, the mesh had converged as done in

previous studies [16]. With the new mesh, the base hull was tested at a several different speeds in order to obtain the resistance curve.

5.2.1 Mesh Convergence Results

The four individual meshes were tested and the results for the total drag, the sinkage, and the final trim angle are shown in Table 10. For each subsequent mesh refinement, the differences in each tested parameter were less than that of the previous the refinement. After two mesh refinements, the percent difference of each parameter was under 10%. While the criteria was met for the motion, it was not met for the drag because the percent difference was 6%. After the final refinement, the percent difference for total drag, sinkage, and trim were all under 5%. This was below the refinement tolerance, so the fourth mesh was used for all of the simulations going forward.

Table 10. Mesh Convergence Results

	Mesh 1	Mesh 2		Mesh 3		Mesh 4	
	Value	Value	Percent Difference	Value	Percent Difference	Value	Percent Difference
Drag (N)	919.47	789.65	14%	741.17	6%	731.17	1%
Sinkage (m)	0.241	0.269	12%	0.264	2%	0.276	4%
Trim (deg)	2.651	3.068	16%	3.156	3%	3.304	5%

To visualize the change in criteria after each iteration, the results for total drag, sinkage, and trim angle were plotted for each mesh. The results are shown in Figure 29 and Figure 30. The plots show that as the mesh was refined, the change in each result was less and the slop of the curves decreased. For the drag, the result decreased after each iteration until the value was around 740 N. For the motion, both the sinkage and trim increased with each iteration with the exception of the sinkage for the third trial. For both motion plots, the percent difference was larger after the forth mesh iteration than the third, but was still at or below 5%.

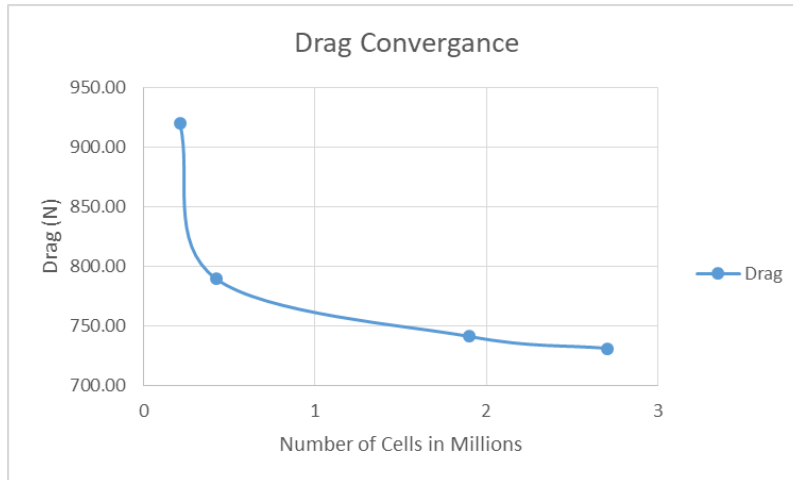


Figure 29. Drag Convergence Plot

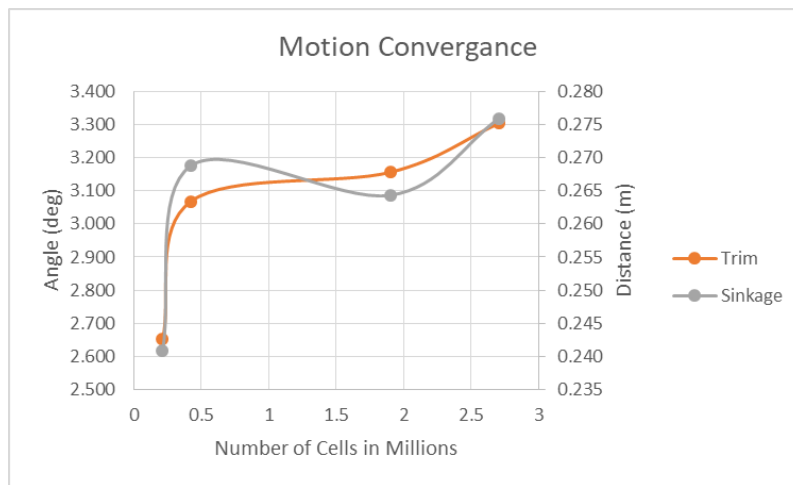


Figure 30. Motion Convergence Plot

The final mesh that was used in rest of the analysis is shown below with the mesh values shown in Table 11. The volume mesh for the far field is shown in Figure 31. The mesh was well defined behind the hull in order to capture the wake generation. The mesh was anisotropic refined at the surface of the water to accurately capture the multiphase interaction of the water and air. The overset region shown in Figure 32 contains actual hull. This prism layers shown in Figure 33 were the smallest cells in the model and were designed to determine the flow very close to the hull. This ensured the flow around the hull and in the boundary layers were accurate. As the distance

from the hull increased, the mesh became coarser until it was fairly large near the boundaries of the far field.

Table 11. Final Mesh Values

	Far Field	Overset
Base Size (m)	5	2
Target Surface Size (%)	100	25
Minimum Surface Size (%)	10	0.5
Surface Curvature (# Points / Circle)	100	200
Surface Growth Rate	1.3	1.3
Number of Prism Layers	NA	20
Prism Layer Stretching	NA	1.2
Prism Layer Thickness (%)	NA	5
Volumetric Control 1 (%)	3	3
Volumetric Control 2 (%)	3	3
Volumetric Control 3 (%)	1.5	1.5
Number of Cells	2706977	

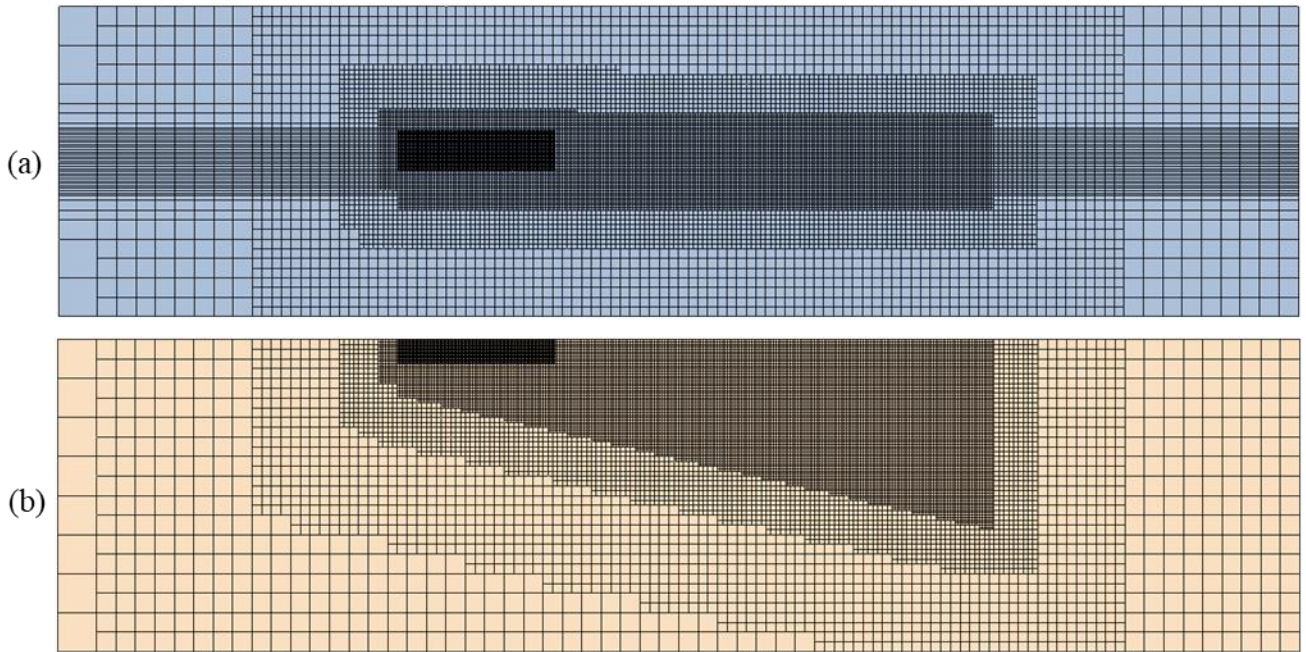


Figure 31. (a) Side View and (b) Top View of the Final Far Field Volume Mesh

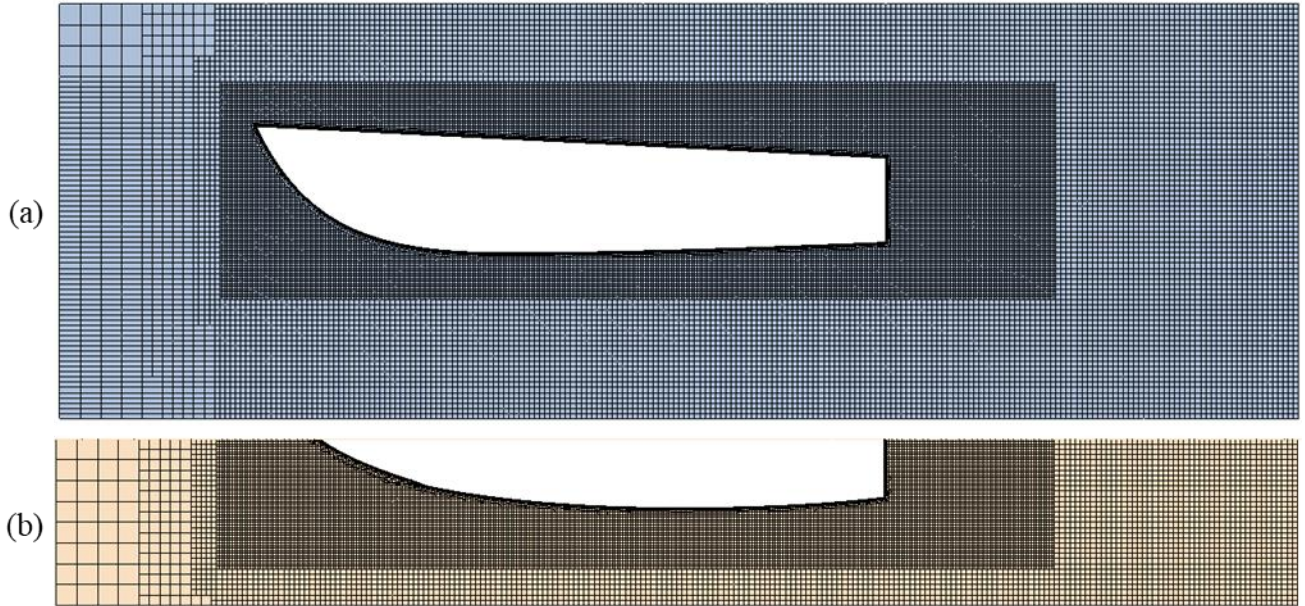


Figure 32. (a) Side View and (b) Top View of the Final Far Field Overset Mesh

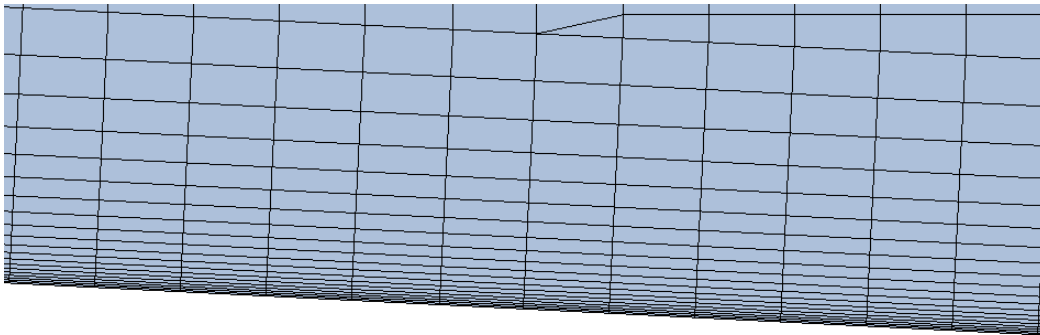


Figure 33. Final Prism Layer for the Hull

5.2.2 Base Hull Simulation Results

Using the final well defined mesh, the base hull was tested at several different speeds. The slowest test speeds were chosen to match the Froude Numbers from the scale model tests performed in Section 6. As the speed increased past the towing tanks capabilities, the velocity was increased by 1.5 m/s until the speed reached 9 m/s and then reduced to 1 m/s for faster convergences. At each speed, the total drag, drag coefficient, trim angle, and sinkage were recorded and are shown Table 12.

Table 12. Base Hull Results

Speed (m/s)	Froude Number	Total Drag (N)	Drag Coefficient	Trim Angle (deg)	Sinkage (m)
0	0	0	0	0	0
0.62	0.07	73.20	0.0106	0.06	-0.003
2.08	0.24	884.60	0.0113	0.64	-0.023
3.43	0.40	3491.11	0.0163	2.62	-0.042
4.36	0.50	6787.84	0.0196	4.37	-0.015
6.00	0.69	9575.30	0.0146	5.97	0.063
7.50	0.87	10857.20	0.0106	7.38	0.150
9.00	1.04	11380.65	0.0077	8.13	0.239
10.00	1.16	11471.94	0.0063	8.44	0.297
11.00	1.27	11054.74	0.0050	8.22	0.372
12.00	1.39	10603.76	0.0041	7.81	0.408
13.00	1.50	10156.02	0.0033	7.26	0.440
14.00	1.62	9536.38	0.0027	6.97	0.452
15.00	1.73	9350.53	0.0023	6.71	0.483
16.00	1.85	9160.84	0.0020	6.45	0.505
17.00	1.97	8919.54	0.0017	6.27	0.526
18.00	2.08	8766.60	0.0015	6.04	0.544
19.00	2.20	8570.18	0.0013	5.89	0.561
20.00	2.31	8513.22	0.0012	5.76	0.574

As the velocity of the hull increased, the hulls relative position to the surface of the water continually changed. Figure 34 plots the motion of the hull as the Froude Number was increased, while Figure 35 shows the hull's position at several tested speeds. At low speed, the boat's center of mass briefly sank into the water, but after $F_r = 0.4$ the hull continually rose out of the water. The trim angle continually increased until $F_r = 1.16$. At this point the trim angle was maximal with a value of 8.46 degrees. As the velocity was increases further, the angle began to decrease slightly.

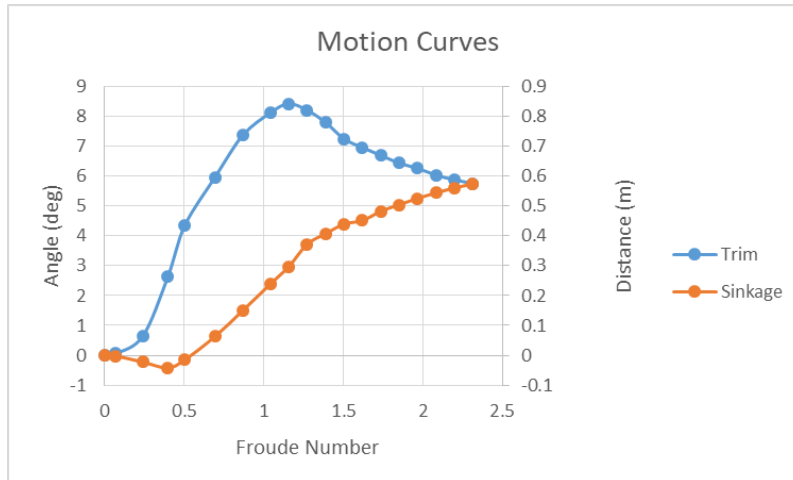


Figure 34. Motion Plot for the Base Hull

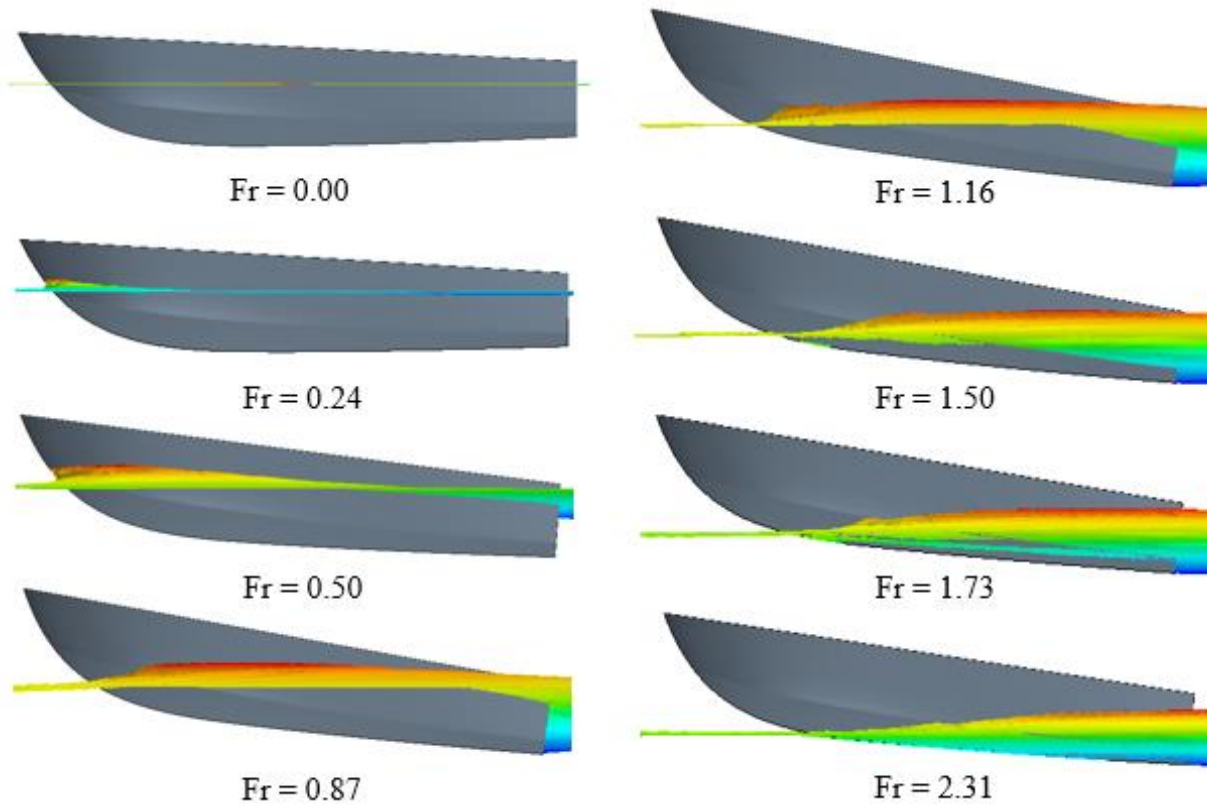


Figure 35. Visualization of Hull Motion

The hull's motion had significant effect on the total drag. Figure 36 shows the resistance curve of the boat and Figure 37 shows the plot of the drag coefficient. At low speeds, there is only a small change in the total resistance and drag coefficient, but as speed increased past $Fr = 0.24$ the changes began to significantly increase. This corresponded to the change in trim angle. As the

slope of trim angle plot increased, the slope of the resistance curve also increased. At $F_r = 0.5$, the slope for both the trim angle and resistance, along with the actual value for the drag coefficient were maximal. The total resistance continued to increase until $F_r = 1.16$, after which it began to decrease, corresponding with the maximum trim angle. At this velocity, the total resistance was greatest with a value of 11471.94 N. As the speed increased further, the total resistance decreased slightly.

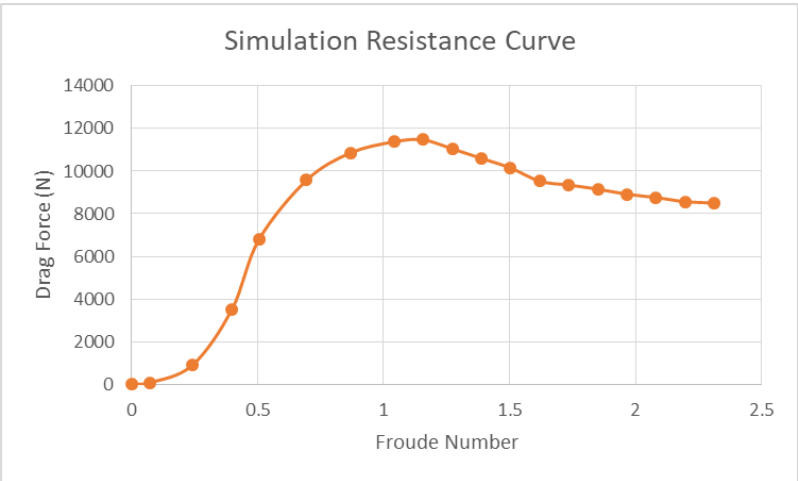


Figure 36. Base Hull Resistance Curve

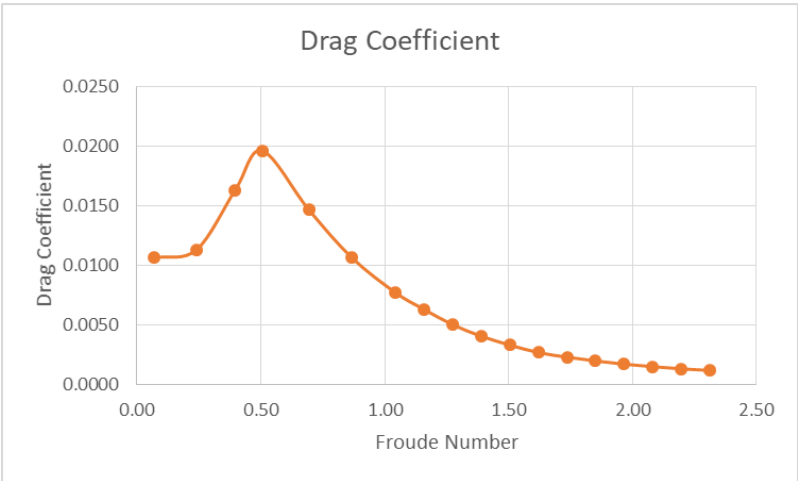


Figure 37. Drag Coefficient

The change in hull position as speed increased affected the wetted surface area of the hull. Figure 38 shows the volume fraction of water on the bottom of the hull at different test speeds.

Volume fraction is a measure of the phase present on the surface of the hull where 1 represents only water, while 0 represents only air. Values between 0 and 1 represent the proportion of water relative to the total volume. As the speed increased, the area in contact with only water decreased. This was due to the trim angle increasing and the hull rising out of the water. Although the wetted surface area decreased, the total resistance increased. This was due to the contact angle between the hull and water increasing. At speeds close to 0 m/s, the flow of water and surface of the hull were close to parallel. At higher speeds, they became more perpendicular. This created a larger stagnation zone where the water impacted the hull rather than flowing over it. While the reduction in wetted surface area decreases the skin friction drag, the pressure differential increased with a greater magnitude, causing the increase in total drag observed. As the trim angle began to decrease, the wetted surface area continued to decrease and the volume fraction on the bottom of the hull became less than 1. This means that there was a mixture of water and air on the bottom of the hull. This allowed for a decrease in the total resistance because the fluid viscosity of the mixture is less than that of water.

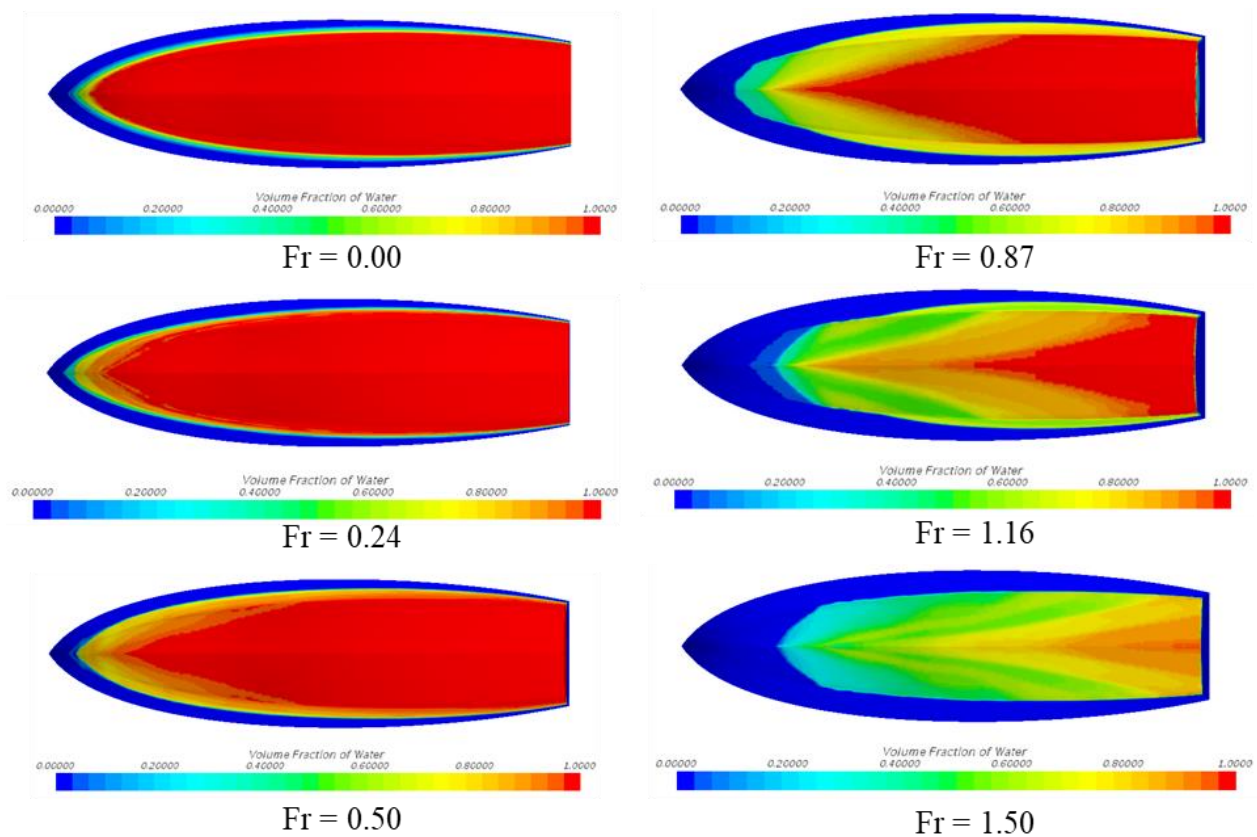


Figure 38. Wetted Surface Area at Different Test Speeds

A final observed characteristic was the wake pattern created by the hull. As the speed increased the wake pattern changed and is shown in Figure 39. At low speeds there was almost no change on the surface of the water, but as the speed was increased the wake became more defined. At $Fr = 0.5$, the beginnings of a wake were present with transverse waves propagating from behind the hull. During the transition region, at $Fr = 0.87$, the traditional wake becomes more defined with a large wake angle. As the speed was increased further, the wake continued to become more defined and the angle decreased. By $Fr = 2.31$, the wake is very narrow and represents a traditional wake generated by a high speed planing hull.

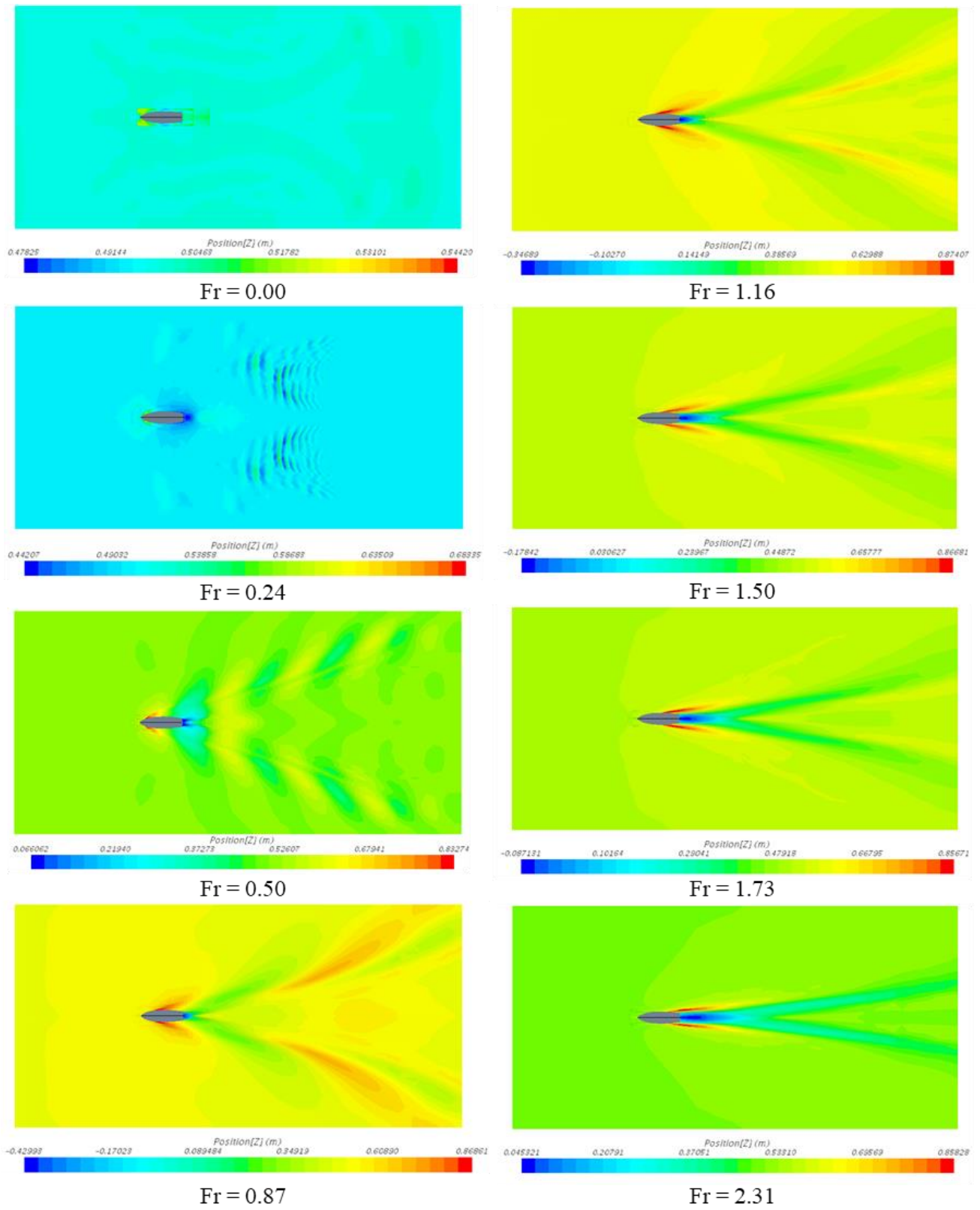


Figure 39. Wake Pattern at Different Test Speeds

The simulated data matched the expected behavior over the tested speeds. At low speeds the hull performed as a displacement hull with a small increase in drag. As the speed increased, the hull entered the transition region. This corresponded to the large increase in trim angle and total drag. There was a distinct ‘hump’ region in the resistance curve during the transition regime. As the hull left the transition region and began to plane, the trim angle decreased, the center of mass continued to rise out of the water, and the resistance began to decrease. This behavior matched what was observed in previous studies [2] [5] [9]. The only difference was that the Froude Numbers were larger than expected for the transition from displacement to planing. This was due to the large value for the mass of the hull. The value was much larger than that of a real world hull, but matched the scale model. This was due to the scale model being made from solid wood, whereas a real hull is mostly hollow. The wake generated by the hull began to form during the transition region and become more defined as the hull began to plane. At the higher test speed, the wake angle was small and well defined and matched the data from previous studies [8] [9]. The data from this simulated hull matched the expected behavior based on previous studies and showed that the created CFD simulation can accurately determine the flow around a planing hull at various speeds.

6. Phase II: Model Validation

6.1 Procedure

The CFD simulation was validated using a scale model testing in a towing tank. The model was a 1:33.33 scale model of the original 25 ft hull and is shown in Figure 40. This scale was chosen to have the scale model be 9 in long. Originally, a 1 ft model was going to be used, but that proved too large to be milled in Grand Valley State University's plastics lab. The model was made from treated pine and created using a 3D milling operation. The final surface was then sanded and a clear top coat was applied to ensure a smooth surface. The final dimensions of the model are shown in Table 13. The model was 9 in in length with a beam of 2.6 in and a depth of 1.8 in. The front, bottom and side views are shown in Figure 41, 42, and 43 respectively.



Figure 40. Scale Model Hull

Table 13. Scale Model Dimensions

Length	9.0 in	22.86 cm
Beam	2.6 in	6.48 cm
Depth	1.8 in	4.57 cm
Chine Height	2.5 in	6.40 cm
Waterline Length	8.9 in	22.5 cm
Wetted Surface Area	50.9 in ²	328.2 cm ²
Deadrise Angle	15.6 deg	

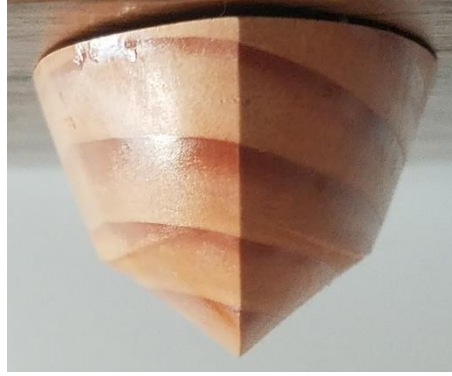


Figure 41. Scale Model Front View



Figure 42. Scale Model Bottom View



Figure 43. Scale Model Side View

The scale model was tested in Grand Valley State University's 12 ft towing tank located in the Fred M. Keller Engineering Laboratories room 102 and is shown in Figure 44 with the tank dimensions on Table 14. The tank had good ratios when compared to the model. The smallest ratio was 5.3 for the water depth. The length and width were both around or above 10 times in size. A numerical method for examining the tank size was the blockage ratio given by Schuster [28]. The blockage ratio is defined as the ratio between the frontal area of the hull and cross section area of the tank. The blockage ratio (m_b) is given by the following:

$$m_b = \frac{A_x}{A}$$

Where A_x is the sectional area of the tank, and A is the maximum sectional area of the model. The blockage ratio correction (ΔV) is given by the following:

$$\frac{\Delta V}{V} = \frac{m_b}{1 - m_b - Fr_h^2} + \left(1 - \frac{R_v}{R_T}\right) \frac{2}{3} Fr_h^{10} \quad 42$$

Where m_b is the blockage ratio, R_v/R_T is the ratio of viscous resistance to total resistance, and Fr_h is the depth Froude Number given by the following:

$$Fr_h = \frac{V}{\sqrt{gh}} \quad 43$$

Where V is the velocity, g is the acceleration due to gravity, and h is the depth of the water. When determining the correction factor for the towing tank at the test speeds, a correction of under 1% was needed, showing the tank was of adequate size for the scale model testing.



Figure 44. GVSU 12 ft Tow Tank

Table 14. Towing Tanks Dimensions

	Numerical Value		Ratio to Model
Length	12 ft	3.7 m	16.0
Width	2 ft	61.0 cm	9.4
Water Depth	9.5 in	24.1 cm	5.3

The tank used a strain gage on a cantilever beam to determine the drag force. As the horizontal force increased, the deflection of the beam also increased. The strain gage was able to measure the deflection and output a numerical value for the strain. This allowed for the determination of the total drag force from the tested hull. Before testing, the tow tank had to be

After the calibration was complete, the model was mounted to the towing bar as shown in Figure 47. The bar was attached above the center of gravity to ensure that proper rotation could be achieved. The attachment was also free to move vertically so the sinkage of the hull could be accurately modeled. A small weight of 20 g was added to aft to have the correct center of gravity so that it matched the simulation. The boat was then tested at different speeds shown in Table 15, and the strain values were recorded. The final step was to determine the drag force, drag coefficient, and compare these values to the CFD simulations results.

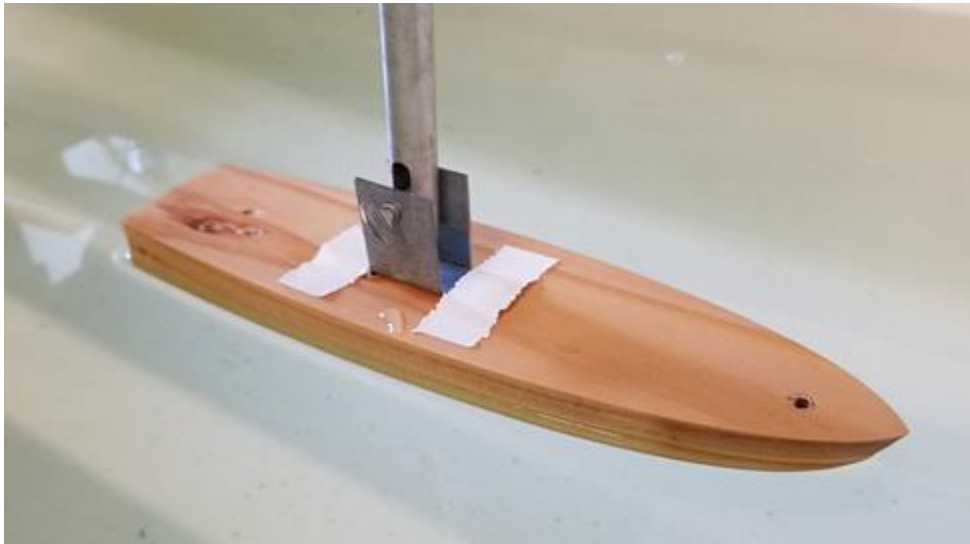


Figure 47. Scale Model in Towing Tank

Table 15. Tested Speeds

Setting	Speed (ft/s)	Speed (m/s)
20	0.35	0.11
30	0.63	0.19
40	0.91	0.28
50	1.18	0.36
60	1.47	0.45
70	1.74	0.53
80	1.95	0.59
90	2.22	0.68
100	2.48	0.76

6.2 Scale Model Results

The calibration was completed before the scale model was tested. To achieve this, the strain gage was zeroed before any weight was added. A hanging mass was added and the mass was increased by increments of 10 g until the total was 100 g. The resulting strain values are shown in Table 16. The data was then plotted and the relationship between force applied and measured strain was determined and is shown in Figure 48.

Table 16. Towing Tank Calibration Results

Mass (g)	Force (N)	Strain ($\mu\epsilon$)
0	0	0
10	0.10	11
20	0.20	42
30	0.29	50
40	0.39	74
50	0.49	92
60	0.59	119
70	0.69	128
80	0.78	150
90	0.88	160
100	0.98	173

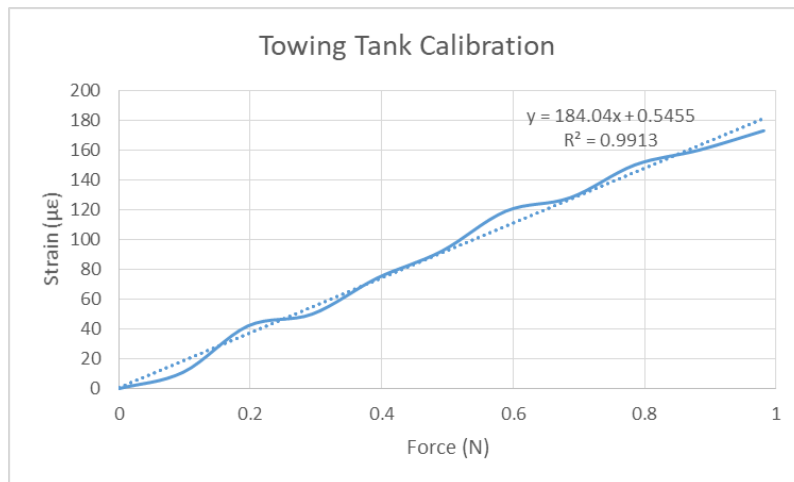


Figure 48. Applied Force vs Measured Strain Plot

The plot showed a consistent upward trend in the strain. As the force increased, the measured strain also increased. The coefficient of determination (R^2) value was 0.9913. This

showed a strong, positive, and linear correlation between the force applied and the strain measured in the strain gage. The resulting relation between force (F) and microstrain (ε_μ) is shown in Equation 41 and was used to determine the drag values.

$$\varepsilon_\mu = 184.04 F + 0.5455 \quad 44$$

After the model was tested at each speed the total drag force and drag coefficient were calculated. The final results from the scale model testing are shown in Table 17. The results showed that as the test speed increased, the corresponding drag also increased with the exception being at low speeds. The drag coefficient was relatively constant at around 0.04 with the exception of at the lowest speeds. This leads to the belief that the low speed results may not be entirely accurate. It is expected that the total drag will be the lowest when the tested speed is lowest, and the drag coefficient should be relatively constant. It was possible that drag was too low for the strain gage to accurately measure leading the higher than expected values.

Table 17. Scale Model Results

Speed (m/s)	Froude Number	Strain ($\mu\varepsilon$)	Total Drag (N)	Drag Coefficient
0.11	0.07	13	0.07	0.363
0.19	0.13	12	0.06	0.103
0.28	0.19	14	0.07	0.058
0.36	0.24	18	0.09	0.045
0.45	0.30	24	0.13	0.039
0.53	0.35	32	0.17	0.037
0.59	0.40	42	0.23	0.039
0.68	0.45	50	0.27	0.036
0.76	0.50	58	0.31	0.033

When the results of the scale model testing are plotted along with the full scale simulated results, both plots have the same trend as shown in Figure 49. As the speed increased, the total drag also increased, with the rate of change being the least at low speeds and greater at higher speeds.

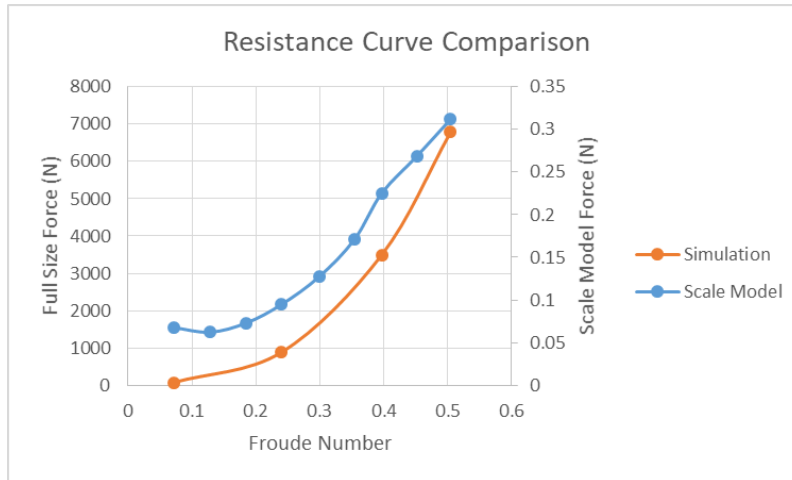


Figure 49. Simulated and Scale Model Results

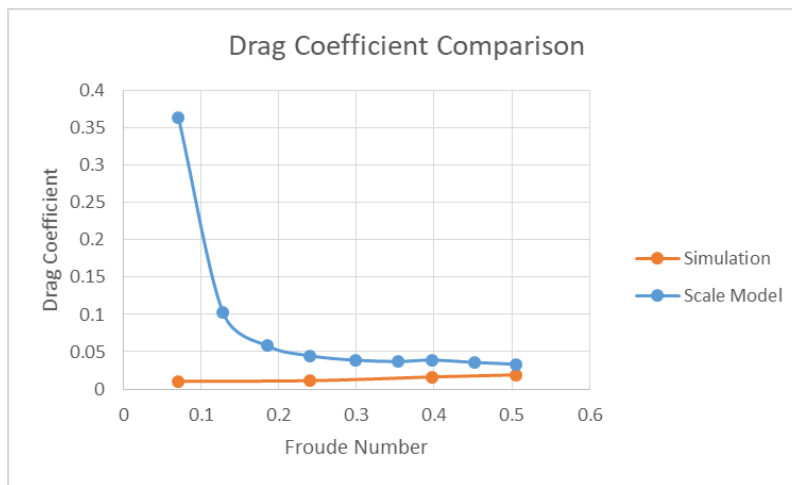


Figure 50. Simulated and Scale Model Drag Coefficients

When comparing the drag coefficients, the simulated drag was about a quarter of the scale model testing at the higher speeds and when the Froude Numbers were the same. At low speed, the scale model had a much larger drag coefficient. This was not desirable as it shows a difference between the simulation and physical testing. At low speeds, the difference was most likely caused by error in the strain gage when only small forces were applied. At higher speeds the difference could be a result of uncertainty in the strain gage, blockage, or an error in the simulation.

A final method of validations was to compare the trim angle and sinkage of the simulated hull to the scale model test. For the scale model test, a 5 cm x 5 cm grid was placed behind the

towing tank to allow for accurate measurements. The test speed used was at a setting of 50 which corresponded to 0.36 m/s and a Froude Number of 0.24. The side view for the simulated hull is shown in Figure 51 and the side view from scale model testing is shown in Figure 52. Based on a purely visual analysis, both models appeared to be very similar. Both sat at about the same height in the water and had roughly the same trim angle.



Figure 51. Side View of Simulated Hull at $Fr = 0.24$



Figure 52. Side View of Scale Model Hull at $Fr = 0.24$

Using the grid in the background the actual values were also determined and are in Table 18. The simulated hull had a trim angle of 0.64° while the scale model hull was at 0.72° . When examining the sinkage, a straight comparison of values would not have provided any useful information. This was because each model was at a different scale. To provide a more accurate comparison, the sinkage values were divided by the total length of the boat. The normalized

sinkage values for the simulated and scale model hulls were -2.96×10^{-5} and -2.75×10^{-5} respectively. The percent differences were both below 12%. Although this was rather large value, there was a large amount of uncertainty in each measurement. The data was not entirely accurate due to the perspective shot, the refraction from the water, and distortion from the glass. Even with these sources of error, this information did provide evidence that the CFD simulation was providing accurate data.

The hull position and orientation were very similar with only a small numeric difference. The difference in trim angle could have been caused by a difference in mass distribution. The CFD model had a defined center of mass which the moment of inertia is calculated from. For the scale model, the hull had a uniform density. This caused the center of mass to be much more forward than that of the simulated hull and thus required the addition of a 20g weigh to be added to the back half of the hull. This moved the center of mass to the correct horizontal position, but may not have been the correct vertical position. This change in the center of mass could have resulted in the slight difference in trim angle and sinkage.

Table 18. Trim and Sinkage Values at Fr = 0.24

	Scale Model	Simulated	Percent Difference
Trim Angle (deg)	0.72	0.64	11.7
Sinkage (m)	-0.0006	-0.023	NA
Sinkage Ratio (Sinkage / Total Length)	-2.75E-05	-2.96E-05	7.4

The combination of the correct trend in drag, the drag coefficient, and hull motion showed that simulation was accurate and could be used to analyze the different hull characteristics. The resistance curve for the simulated hull had the same trend as the scale model tests. The tested speeds were at the low end of a boats speeds with the maximum being Fr = 0.50, but this was unavoidable due to the limitations of the towing tank. To achieve greater Froude Number, the test

speed would have had to increase or the model size would have had to be decreased. A smaller model would have resulted in less drag and would have been less accurate due to the high uncertainty at the low end of the strain gage.

Although the tested speeds were below the planing speed, the results still showed the CFD model was accurate. The drag coefficient was smaller than expected but the model still captures the correct trends in total drag. The differences could have been caused by blockage in the tank, uncertainty in the strain gage, or an error in the simulation. Finally, the hull motion for the CFD model and scale testing were very similar. The sinkage and trim were almost the same with only a small difference that would be explained by a slight difference in the center and distribution of mass. These factors show that the simulation was accurate and capable of performing the analysis.

7. Phase III: Effects of Geometric Features

7.1 Procedure

After developing a working simulation and determining that it was accurate, the different geometric features were tested. The tested features were the deadrise angle, keel line geometry, and spray rail location. These features were changed from the base hull with a minimum and maximum value relative to the base. The values used for each case are shown Table 19. Two different test schemes were used to analyze the features. For the first, only one feature was changed per test. This was done to evaluate the effects of each geometric feature relative to the base hull. For each test, the mesh properties, physics, and boundary conditions were the same as those from base hull simulations found in Section 5.1 CFD Model. Each hull was tested at 20m/s corresponding to $Fr = 2.31$. This speed was chosen because it was within the planing regime and would provide a good indication on how each hull behaved while planing.

Table 19. Hull Geometry Characteristics

	Chine Height (in)	Deadrise Angle (deg)	Keel Line Depth Relative to Base (in)	Spray Rail Location (% of Surface from Medial Edge)
Base Hull	12	15.6	0	NA
Minimum Value	9	9.09	-10	30
Maximum Value	15	21.8	10	60

After evaluating each feature separately, the models were tested using the design of experiment (DOE) method. A 2x2x3 factorial design was used to evaluate the significance of each feature and the interactions between them. The minimum and maximum values from the previous section were used for both the deadrise angle and keel line geometry, while all three cases were used for the spray rail location. Table 20 contains the final DOE table and shows what tests were performed. All 12 cases were tested in a full factorial design in order to determine the effect of each characteristic without having to block or alias any of the interaction terms.

Table 20. DOE table

Case Number	Parameter		
	Deadrise Angle	Keel Line	Spray Rail
1	Min	Min	Min
2	Min	Min	Max
3	Min	Min	Base
4	Min	Max	Min
5	Min	Max	Max
6	Min	Max	Base
7	Max	Min	Min
8	Max	Min	Max
9	Max	Min	Base
10	Max	Max	Min
11	Max	Max	Max
12	Max	Max	Base

In order to determine the significance of the geometric features and the interactions, an analysis of variance (ANOVA) test was performed using the statistics software JMP developed by SAS Institute. A single replicate analysis was performed with significance level (α) of 0.05. The fixed effect model [29] for the 2x2x3 factorial design was as follows:

$$x_{ijkl} = \mu + \alpha_i + \beta_j + \gamma_k + (\alpha\beta)_{ij} + (\alpha\gamma)_{ik} + (\beta\gamma)_{jk} + (\alpha\beta\gamma)_{ijk} + \epsilon_{ijkl} \quad 45$$

$$i = 1, 2; \quad j = 1, 2; \quad k = 1, 2, 3 \quad l = 1$$

Where x_{ijkl} is the typical observation, μ is a constant, α_i is the effect due to deadrise angle, β_j is the effect due to the keel line geometry, γ_k is the effect of the spray rail location, $\alpha\beta$, $\alpha\gamma$, $\beta\gamma$, and $\alpha\beta\gamma$ are the effects due to the interactions, and ϵ_{ijkl} represents the experimental error. The hypothesis for each analysis was that the effects of each geometric characteristic and all of the interactions on the total drag, trim angle, and sinkage were zero. The alternative was that at least one effect was not equal to zero. The hypothesis (H_o) and alternative (H_a) were stated as follows:

- a. $H_0: \alpha_i = 0$ $i = 1, 2$
 $H_a: \text{not all } \alpha_i = 0$
- b. $H_0: \beta_j = 0$ $j = 1, 2$
 $H_a: \text{not all } \beta_j = 0$
- c. $H_0: \gamma_k = 0$ $k = 1, 2, 3$
 $H_a: \text{not all } \gamma_k = 0$
- d. $H_0: (\alpha\beta)_{ij} = 0$ $i = 1, 2; j = 1, 2$
 $H_a: \text{not all } (\alpha\beta)_{ij} = 0$
- e. $H_0: (\alpha\gamma)_{ik} = 0$ $i = 1, 2; k = 1, 2, 3$
 $H_a: \text{not all } (\alpha\gamma)_{ik} = 0$
- f. $H_0: (\beta\gamma)_{jk} = 0$ $j = 1, 2; k = 1, 2, 3$
 $H_a: \text{not all } (\beta\gamma)_{jk} = 0$
- g. $H_0: (\alpha\beta\gamma)_{ijk} = 0$ $i = 1, 2; j = 1, 2; k = 1, 2, 3$
 $H_a: \text{not all } (\alpha\beta\gamma)_{ijk} = 0$

For each factor and all of the interactions, an F statistic was calculated and used with one degree of freedom to determine the P-value for each factor. If the P-value was below the significance level of $\alpha = 0.05$, then there would be significant evidence to reject the null hypothesis and determine that the factor in question did have an effect on the performance of the hull. If the P-value was above 0.05, then there would not be significant evidence to claim that factor had an effect on the performance of the hull. After performing the ANOVA test, any nonsignificant terms that were present were removed from the analysis and it was rerun without those terms [30]. This process continued until only significant terms remained.

7.2 Single Characteristic Results

When testing single characteristics, one feature was changed from the base hull and tested. The minimum and maximum geometries were tested individually, resulting in a total of 7 test cases: the minimum and maximum for each feature and those of the base hull. After performing each of the tests the results for total drag, drag coefficient, trim angle and sinkage were recorded and are shown in Table 21. The numerical results show that each of the tested features had an effect on hull performance, but some were more profound than others.

Table 21. Single Term Effects Results

Case Number	Description			Results			
	Deadrise Angle	Keel Line	Spray Rail	Total Drag (N)	Drag Coefficient	Trim Angle (deg)	Sinkage (m)
1	Base	Base	Base	8513.22	0.00117	5.76	0.574
2	Min	Base	Base	7683.99	0.00106	5.16	0.622
3	Max	Base	Base	9305.22	0.00128	6.34	0.534
4	Base	Min	Base	8153.96	0.00112	5.90	0.587
5	Base	Max	Base	8725.52	0.00120	5.55	0.561
6	Base	Base	Min	8288.45	0.00114	5.88	0.589
7	Base	Base	Max	8309.50	0.00114	5.78	0.591

The single characteristic results for total drag, trim angle and sinkage were plotted and are shown in Figure 53, Figure 54, and Figure 55 respectively. These plots show how each of the geometric features affected the hulls performance and provided a visual representation on the effectiveness relative to the other features.

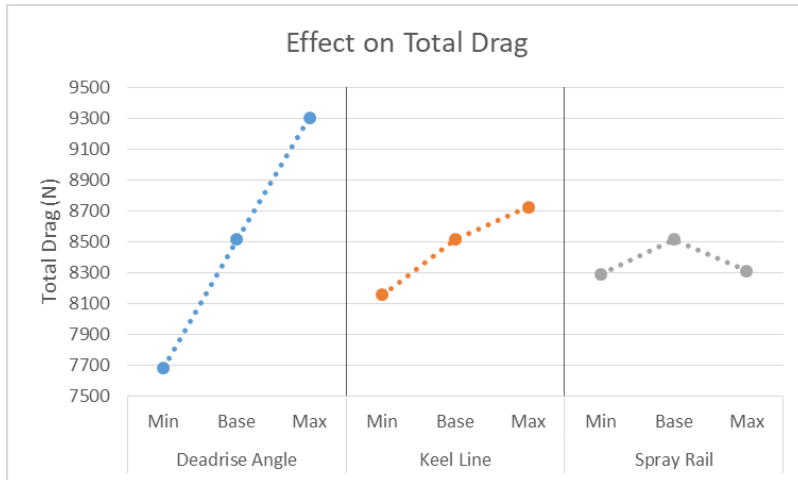


Figure 53. Single Parameter's Effect on Total Drag

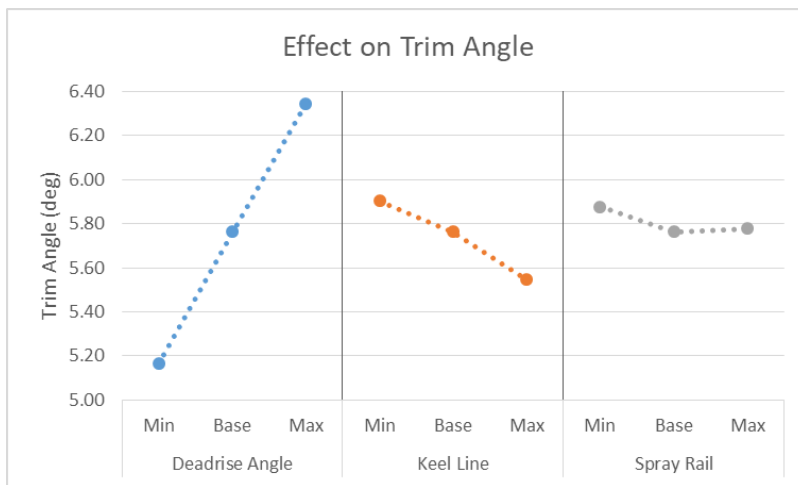


Figure 54. Single Parameter's Effect on Trim Angle

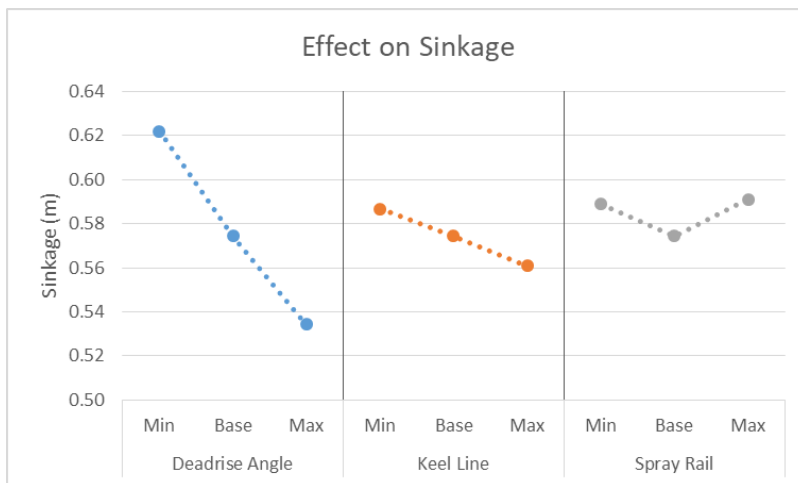


Figure 55. Single Parameter's Effect on Sinkage

Based on the results, it can be seen that each of the characteristics have an effect on hull performance. The deadrise angle had the most significant effect on total drag, trim angle, and sinkage. As the deadrise angle increased from 9.09 to 21.8 degrees, the trim angle also increased by 1.18 degrees while the sinkage decreased by 9 cm. This resulted in an increase of the total drag from 7683.99 N to 9305.22 N. The total difference from the minimum to the maximum geometry was 1621.23 N. This difference was much greater than that of the other two test parameters with the difference being 2.83 and 7.96 times larger than that of the keel line geometry and the spray rail location respectively. A smaller deadrise angle allowed the hull to generate more lift and rise further out of the water. This significantly decreased the wetted surface area and allowed the boat to be closer to parallel with the surface of the water. The combinations of these factors lead to the decrease in total drag.

Changing the keel line geometry had the next largest effect on the hull's performance. The low geometry had a total drag of 8153.96 N which was 571.56 N less than that of the high geometry. As the height of the keel line increased, the trim angle and the sinkage decreased. The trim angle and sinkage for the low geometry were 0.36 degrees and 3 cm greater than that of the high geometry.

The addition of spray rails had an effect on the hull's performance, while changing their location had very little. The reduction in drag from the addition of spray rails was 214.25 N on average, but the difference from changing the location was only 21.05 N. The effect on hull position was even less with a maximum difference of 0.11 degrees and 2 cm for trim angle and sinkage respectively. The reduction in drag was most likely caused by the reduction in wetted surface area. The spray rails were able to redirect the water as it moved outward on the hull as shown in Figure 56. This effect was present for both the high and low geometries. Redirecting the

water was able to generate slightly more lift and keep a larger area of the hull dry. Adding spray rails was able to generate more lift and raise the hull out of the water because the flow was redirected downward by the spray rails as shown in Figure 57. The figure shows how as the water moved along the bottom of the hull, the spray rails redirected the flow downward creating more lift. This the created a small vortex above the spray rail, allowing air to enter the region and reduce the wetted surface area.

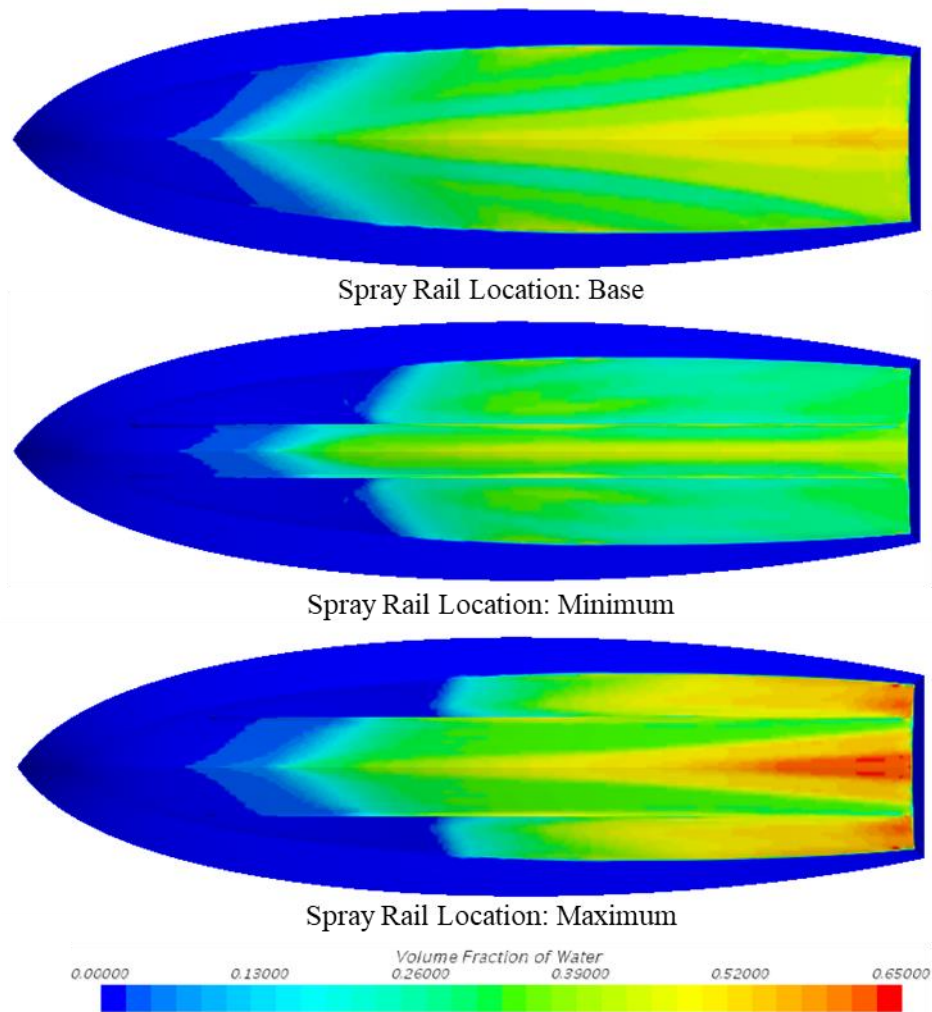


Figure 56. Wetter Surface Area Due to Spray Rails

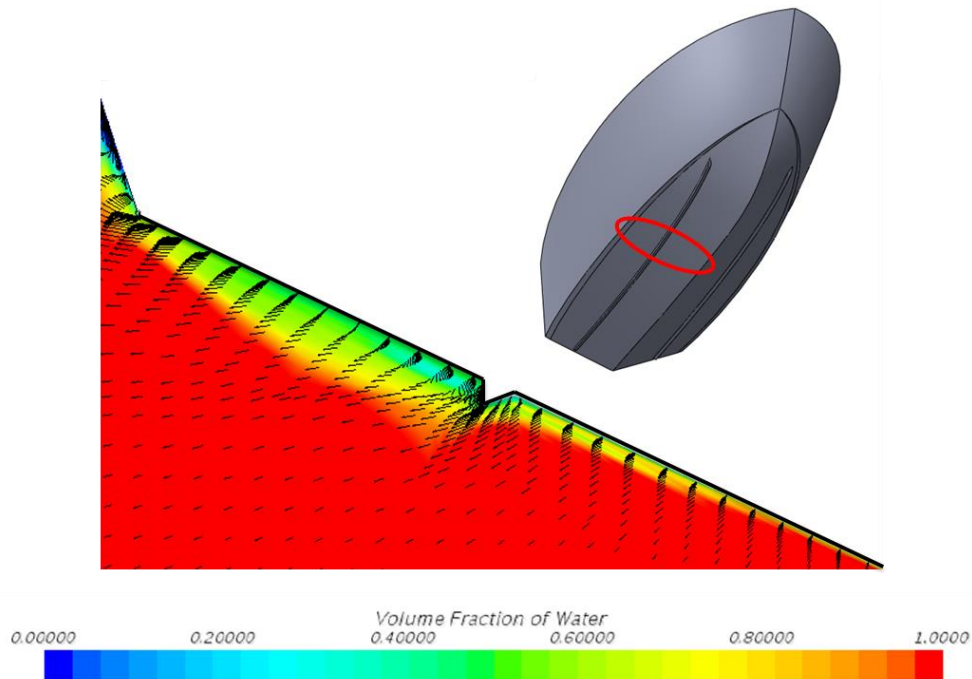


Figure 57. Flow Field Created Spray Rail on the Bottom of the Hull

Simply based on the single parameter tests, it can be seen that each of the geometric changes had an effect on the hulls performance with the deadrise angle having the largest effect. As the angle was increased, the total drag and trim angle increased while the sinkage decreased. The keel line geometry had the next largest effect. Increasing the height of the keel line increased the total drag, while decreasing the trim angle and sinkage. The final geometric feature had the smallest effect. Adding spray rails slightly decreased the total drag and increased the trim angle and sinkage. Changing the relative location of the spray rails had almost no effect on any of the results. While this analysis showed the individual effects, it did not provide evidence of any feature having a statistically significant effect on the results or provide information on the interactions of the geometric features. This resulted in the need for a DOE analysis of the geometric features.

7.3 Full DOE Results

To determine the statistical significance, a 2x2x3 factorial designed DOE analysis was performed. The deadrise angle and keel line height both had two levels being the maximum and minimum geometries. For the spray rails, three levels were tested being the maximum, minimum, and base geometries. This was done to provide information on not only the location of the spray rails, but also on the effect of adding them to the bottom of the hull. After completing the simulations, the results for total drag, trim angle, and sinkage were recorded and are shown in Table 22. When looking at the numerical results, it can be seen that the different geometries had an effect on the hull's performance.

Table 22. Complete DOE Results

Case Number	Description			Results			
	Deadrise Angle	Keel Line	Spray Rail	Total Drag (N)	Drag Coefficient	Trim Angle (deg)	Sinkage (m)
1	Min	Min	Min	7724.17	0.00106	5.52	0.642
2	Min	Min	Max	7803.33	0.00107	5.34	0.643
3	Min	Min	Base	7399.21	0.00102	5.29	0.634
4	Min	Max	Min	8048.05	0.00111	5.29	0.633
5	Min	Max	Max	8214.61	0.00113	5.20	0.632
6	Min	Max	Base	8198.42	0.00113	5.15	0.607
7	Max	Min	Min	8628.54	0.00119	6.27	0.550
8	Max	Min	Max	8913.32	0.00123	6.17	0.552
9	Max	Min	Base	9280.55	0.00128	6.38	0.543
10	Max	Max	Min	9366.83	0.00129	6.29	0.549
11	Max	Max	Max	9545.72	0.00131	6.05	0.541
12	Max	Max	Base	9719.10	0.00134	6.16	0.527

7.3.1 Total Drag Results

The initial ANOVA results for effects of deadrise angle, keel line geometry, and spray rail location on the total drag is shown in Table 23. The resulted showed that the significant terms were the deadrise angle, keel line geometry, and the interaction between the deadrise angle and the spray rails. Other terms were close to significant. These included the three way interaction and the

singular spray rail location. The least significant terms were then removed one by one until a final model was achieved.

Table 23. Total Drag ANOVA Results

Effect Tests					
Source	Nparm	DF	Sum of Squares	F Ratio	Prob > F
Deadrise	1	1	5422059.8	475.3041	<.0001*
Keel Line	1	1	931637.9	81.6685	0.0008*
Deadrise*Keel Line	1	1	6296.3	0.5519	0.4988
Spray Rail	1	1	86049.1	7.5432	0.0516
Deadrise*Spray Rail	1	1	173715.1	15.2281	0.0175*
Keel Line*Spray Rail	1	1	3854.1	0.3379	0.5922
Deadrise*Keel Line*Spray Rail	1	1	75091.3	6.5826	0.0623

Before any conclusions could be made, the model had to be proven reliable. The model had to be normal and have no obvious outliers. To accomplish this, the normal quantile plot, the standard residual plot, and the studentized residual plots were analyzed. The normal quantile plot in Figure 58 showed a linear relationship with no obvious outliers. If the data was skewed, a curve would have been present and the data near the edges would have been further from the predicted line. The standard residual plot is shown in Figure 59. The plot showed relatively centered data with no obvious outliers. The final plot was the studentized residual plot shown in Figure 60. This plot is necessary because outliers influence the regression model. This can make it difficult to identify outliers when using a standard residual plot. The studentized plot is an alternative that compares observed response to the fitted value and is then divided by its estimated standard deviation [29]. The studentized plot showed no obvious outliers and was reasonably centered. Based on these plots, there was not enough evidence to conclude that the data was not normal, so it was determined to be satisfactory. For each subsequent analysis, the same procedure was followed to ensure the results could be used in an ANOVA analysis.

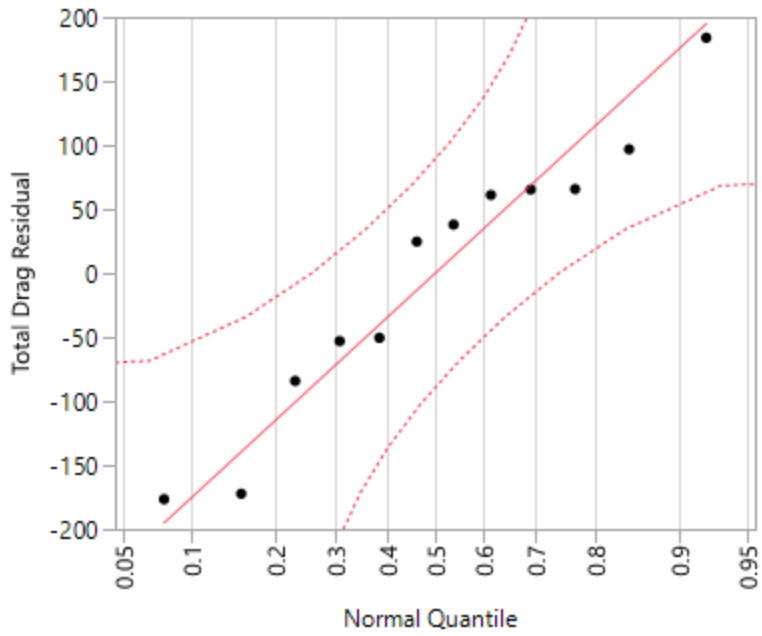


Figure 58. Normal Quantile Plot

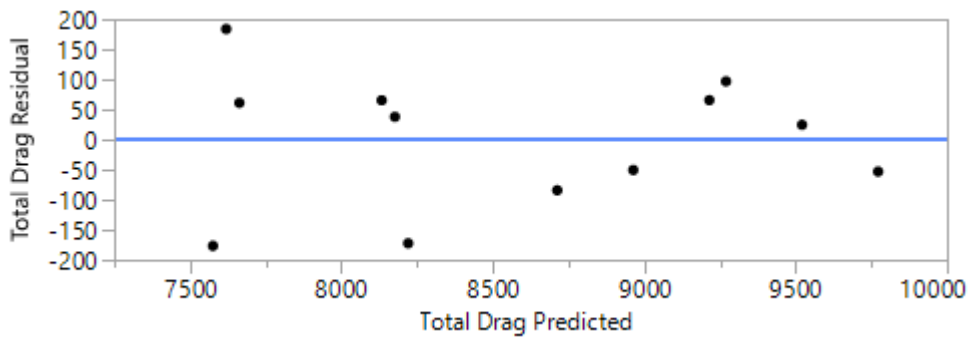


Figure 59. Total Drag Residual Plot

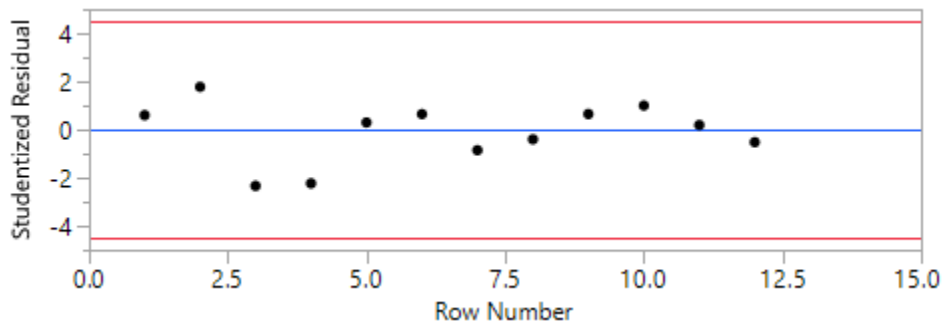


Figure 60. Studentized Total Drag Residual Plot

The final reduced ANOVA table is shown in Table 24. The results showed that there was significant evidence reject the null and conclude that the deadrise angle, keel line geometry, and the two way interaction between deadrise angle and spray rail location had an effect on the total drag of the hull. The effect of only the spray rails were almost significant and was included in the model because the interaction term was significant. Using this analysis, it was difficult to determine what effects changing the spray rail location had on the performance, and what effects were caused by simply adding the spray rails.

Table 24. Reduced Total Drag ANOVA Results

Effect Tests					
Source	Nparm	DF	Sum of Squares	F Ratio	Prob > F
Deadrise	1	1	5422059.8	290.0118	<.0001*
Keel Line	1	1	931637.9	49.8309	0.0002*
Spray Rail	1	1	86049.1	4.6025	0.0691
Deadrise*Spray Rail	1	1	173715.1	9.2916	0.0186*

To better analyze the effects of the spray rails, the DOE analysis was separated into two different studies. The first study included only the spray rail location and did not include hull with no spray rails to better understand the effect of changing the position. The second analysis performed used only one spray rail location and the hull without any to better analyze the effect of adding spray rails.

The first study performed included the location of the spray rails with the results shown in Table 25. The results showed that all three single effects terms were significant along with the two way interaction between the deadrise angle and the keel line depth. These results were different than the original case showing that separated studies would be preferred. The effect profiler for the single term effects is shown in Figure 61. Using this plot, it was possible to determine what effect each geometric feature had on the total drag on the hull. Increasing the deadrise angle, the

keel line height, and the distance of the spray rails from the center of the hull all had the same effect on the hull's performance by increasing the total drag.

Table 25. Total Drag ANOVA Results for Spray Rail Location

Effect Tests					
Source	Nparm	DF	Sum of Squares	F Ratio	Prob > F
Deadrise	1	1	2719409.4	765.9488	0.0001*
Keel Line	1	1	554320.6	156.1299	0.0011*
Deadrise*Keel Line	1	1	50487.1	14.2202	0.0326*
Spray Rail	1	1	62905.6	17.7180	0.0245*

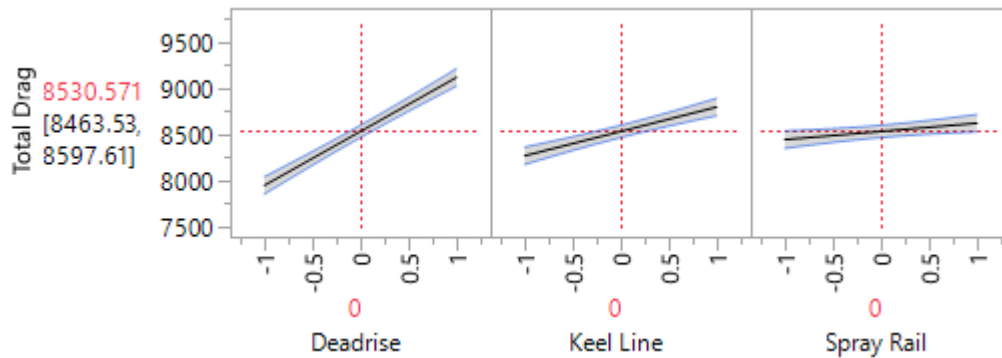


Figure 61. Single Effect Profiler for Total Drag with Different Spray Rail Location

The interaction profiler is shown in Figure 62. The plot showed how each of the geometric features interacted with the others. The plot showed the two way interaction between deadrise angle and keel line geometry. When using the minimum case (-1) for either the deadrise angle or keel line height, and then changing the other from low (-1) to high (1), there was a change in the total drag. When using the maximum case, the change in total drag was greater. This was represented on the chart by an increase in the slope for those interaction. The nonsignificant interactions showed no discernable change in slope. This showed that as both the deadrise angle and keel line height were increased, the total drag increased at a greater rate than when each were changed individually.

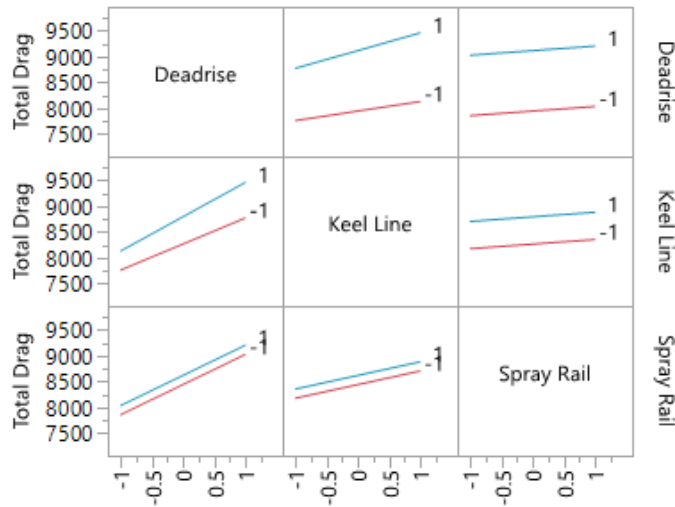


Figure 62. Interaction Profiler for Total Drag with Different Spray Rail Location

To examine the effects of simply adding spray rails, a second analysis was performed. The DOE analysis used the data from one hull with spray rails and the hull without them. The results from this study are shown in Table 26. When looking at the same terms as the original ANOVA results, it was shown that the two way interaction between spray rails and deadrise angle was not significant, contradicting the original results. This again showed that the data from the original ANOVA results in Table 23 was not entirely reliable.

Table 26. Total Drag ANOVA Results with Added Spray Rails

Effect Tests					
Source	Nparm	DF	Sum of Squares	F Ratio	Prob > F
Deadrise	1	1	4267755.6	258.9152	0.0005*
Keel Line	1	1	650617.6	39.4715	0.0081*
Spray Rail	1	1	1808.9	0.1097	0.7622
Deadrise*Spray Rail	1	1	115418.8	7.0022	0.0772

The final reduced results when including the addition of spray rails is shown in Table 27. These results showed that there was enough evidence to reject the null hypothesis and conclude that only deadrise angle and keel line height significantly effects the total drag on the hull. The effect profilers shown in Figure 63 showed that as the deadrise angle or keel line height was

increased, then the total drag also increased. This was consistent with the previous results. The main difference between changing the spray rail location and simply adding them was the effect on the interaction between deadrise angle and keel line height. Having spray rails present on every hull affected the flow enough to make this interaction significant.

Table 27. Reduced Total Drag ANOVA Results with Added Spray Rails

Effect Tests					
Source	Nparm	DF	Sum of Squares	F Ratio	Prob > F
Deadrise	1	1	4110049.3	88.0785	0.0002*
Keel line	1	1	655901.2	14.0560	0.0133*

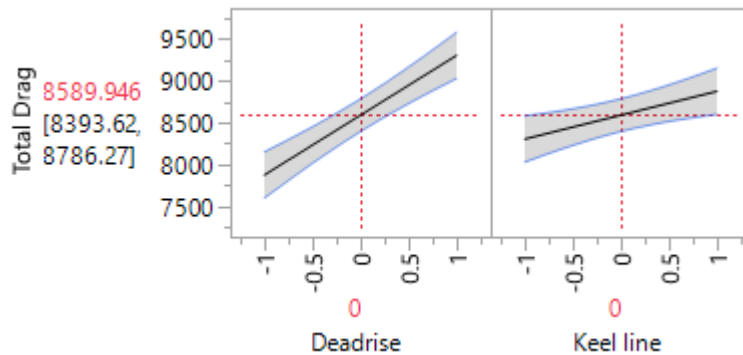


Figure 63. Single Effect Profilers for Total Drag with the Addition of Spray Rails

Based on the ANOVA results, there was enough evidence to reject the null hypothesis and conclude that several geometric features and one interaction had a significant effect on the total drag of the hull. The significant effects were the deadrise angle, keel line height, and the location of the spray rails while the simple addition of spray rails was not significant. The two way interaction between deadrise angle and keel line height was also significant. These results showed that increasing the deadrise angle, keel line height, or distance of the spray rails from the center of the hull increased the total drag on the hull. The DOE study provided enough evidence to support these conclusions.

7.3.2 Trim Angle Results

To analyze the effects of each of the geometric features on the trim angle of the hull, another DOE study was performed. As with the tests for total drag, two separate ANOVA tests were performed. The first only included spray rail location, while the second included the addition of spray rails. Both studies were proven to be reliable by analyzing the normal quantile plot, residual plot and the studentized residual plot. After both were proven reliable, the results were analyzed. The reduced ANOVA results when including spray rail location are shown in Table 28. The only significant term was the deadrise angle. The profiler in Figure 64 showed that as the deadrise angle was increased, the trim angle also increased. Besides the deadrise angle, there was not enough evidence to conclude that any other geometric feature had a significant effect on the trim angle of the hull.

Table 28. Reduced ANOVA Results for Trim Angle with Spray Rail Location

Effect Tests					
Source	Nparm	DF	Sum of Squares	F Ratio	Prob > F
Deadrise	1	1	1.4706125	97.2038	<.0001*

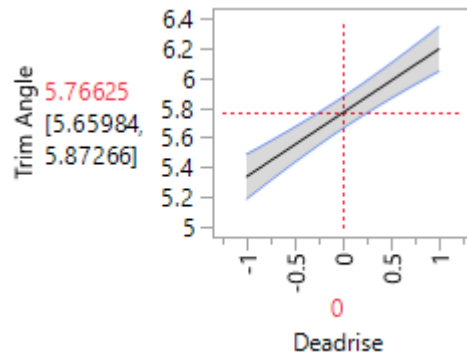


Figure 64. Single Effect Profiler for Trim Angle with Spray Rail Location

When analyzing the addition of spray rails, the results proved to be slightly different as shown in Table 29. The results showed that both the deadrise angle and keel line height were

significant. In the previous analysis, the keel line geometry was almost significant but there was not enough evidence to reject the null with $\alpha = 0.05$. The profiler in Figure 65 shows that as the deadrise angle was increased, the trim angle also increased, but when the keel line height increased, the trim angle decreased.

Table 29. Reduced ANOVA Results for Trim Angle with the Addition of Spray Rails

Effect Tests					
Source	Nparm	DF	Sum of Squares	F Ratio	Prob > F
Deadrise	1	1	1.8273921	339.3290	<.0001*
Keel line	1	1	0.0434491	8.0681	0.0362*

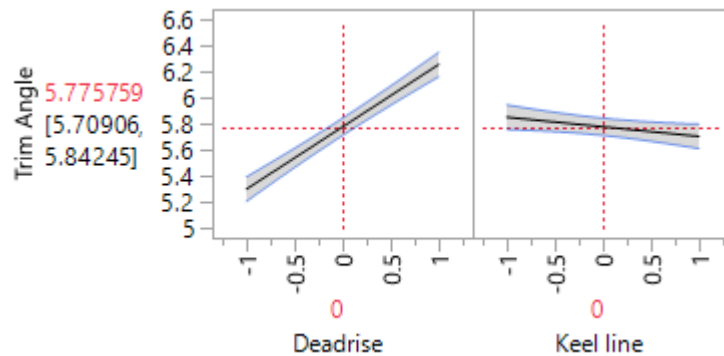


Figure 65. Single Effect Profiler for Trim Angle with the Addition of Spray Rails Added

7.3.3 Sinkage Results

A final set of DOE analysis were performed on the effects of tested geometries on the sinkage of the hull. Both studies were proven reliable by examining the normal quantile plot, residual plot and the studentized residual plot for normality and outliers. The first analysis included the spray rail location and the results are shown in Table 30. The results showed that both deadrise angle and keel line geometry had a significant effect on the sinkage of the hull. The profiler shown in Figure 66 showed that as the deadrise angle and keel line height increased, the sinkage of the hull decreased. This showed that increasing either geometric features, reduced the lift generated by the hull.

Table 30. Reduced ANOVA Results for Sinkage with Spray Rail Location

Effect Tests					
Source	Nparm	DF	Sum of Squares	F Ratio	Prob > F
Deadrise	1	1	0.01602050	1862.849	<.0001*
Keel Line	1	1	0.00012800	14.8837	0.0119*

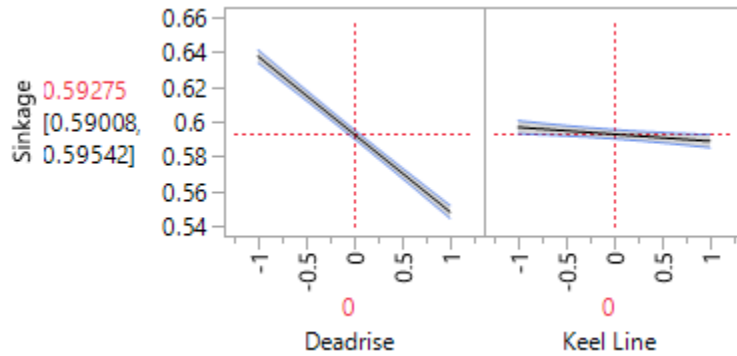


Figure 66. Single Effect Profiler for Sinkage with Spray Rail Location

The second analysis included the addition of spray rails and the results are shown in Table 31. The results showed that each of the geometric had a significant effect on sinkage of the hull. Adding spray rails, regardless of location, increased the lift generated by the hull and thus increased the sinkage as shown in Figure 67. Increasing the deadrise angle or keel line height decreased the sinkage meaning that less lift was generated. This information corresponds and verifies the observations from the previous case.

Table 31. Reduced ANOVA Results for Sinkage with the Addition of Spray Rails

Effect Tests					
Source	Nparm	DF	Sum of Squares	F Ratio	Prob > F
Deadrise	1	1	0.01518255	471.2169	<.0001*
Keel line	1	1	0.00043091	13.3739	0.0216*
Spray Rail	1	1	0.00045314	14.0639	0.0199*

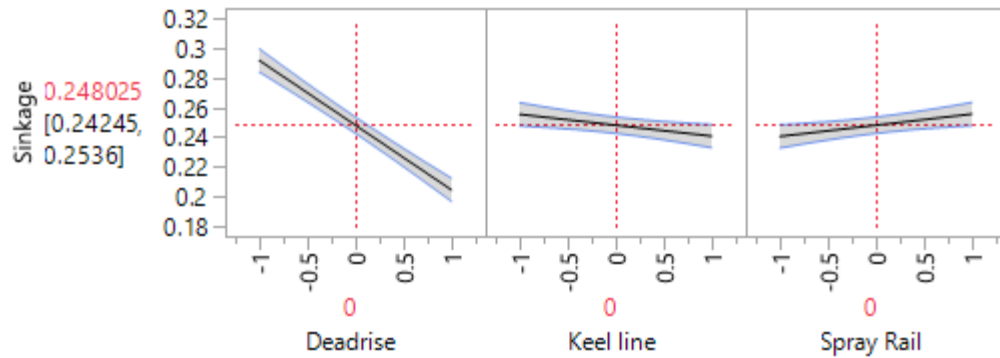


Figure 67. Single Effect Profiler for Sinkage with the Addition of Spray Rails Added

7.4 Geometric Analysis Conclusions

Based on the different DOE analysis performed, there were several geometric features that had an effect on the hull's performance. There was enough evidence to reject the null hypothesis and conclude several of the different geometric features had a significant effect on the hull's performance. As the deadrise angle was increased, the trim angle increased and the sinkage decreased. This meant that the hull sat deeper in the water and had a greater angle while moving through the water. This would result in significantly more drag on the hull as was shown by the results in Table 25 and Table 26. Deadrise angle had the most significant on each of the performance criteria. As the deadrise angle increased, the relative changes in total drag, trim angle and sinkage were greater than those caused by the other geometric features.

Changing the keel line geometry also had a significant effect on the performance of the hull. Increasing the height of the keel line decreased the trim angle and sinkage, while increasing the total drag on the hull. Altering the shape of the bow changed the flow across the entire hull and significantly affects how it performed. When the height increased, the hull generated less lift and was unable to rise out of the water to the same extent as when the keel line was lower.

The final tested geometric feature was the spray rails. Adding spray rails to the bottom of the hull had a significant effect on the sinkage. When they were added, the sinkage increased and

the hull was able to sit higher out of the water. This was due to the water being redirected downward and generating more lift. Changing the location had a significant effect on the total drag. As the spray rails were moved away from the center of the hull, the total drag increased. When the spray rails were located close to the center of the hull, more water was redirected away from the bottom of the hull. At the farther location, the spray rails still reduced the wetted surface area but to a lesser extent.

The final significant term was the two way interaction between the deadrise angle and the keel line geometry. As either the deadrise angle or the keel line height increased, the effect of the other on the total drag increased. So in combination, increasing both the deadrise angle and keel line height resulted in a greater increase in drag than the two individual geometric features could achieve alone.

8. Conclusion

Planing hulls are able to achieve far greater speeds than traditional displacement hulls. This is possible through the use of hydrodynamic forces. As the water flows beneath the boat, the hull's geometry creates lift that raises a portion of the hull out of the water. In some cases, the vessel will ride almost entirely on top of the water with only a small portion actual hull making contact. This significantly reduces the wetted surface area and the drag. There are three types of drag that act on a boat as it travels through the water. These include viscous hull drag, wake making drag, and air resistance. The first type is caused by shear stress in the water and a pressure differential along the hull. Wave making resistance is caused by the energy loss required to create waves, and air resistance is caused by the air acting on the portion of the hull above the water.

There are many geometric features that affect the flow around the hull. These include the deadrise angle, keel line geometry, the location of spray rails. The deadrise angle is angle between the bottom of the hull and the horizontal plane. The keel line is the center line at the bow. Finally, stray rails are small triangular protrusions on the bottom of the hull designed to redirect the flow of water downward to create more lift.

To test these features STAR CCM+ was used to solve for the fluid flow around the hull through a finite difference approach. Reynolds Averaged Navier-Stokes Equations were used to solve the multiphase flow around the hull, while the hull motion was solved using a two degree of freedom dynamic fluid body interaction. An initial model was created to examine the flow around the base hull. The hull was tested at speeds from 0 to 20 m/s. The hull exhibited the correct behavior based on previous studies. As the test speed was increased, the hull's position relative to the surface of the water changed. The trim angle began to increase until the hydrodynamic forces caused the hull to leave the transition region and begin to plane. At that point the total drag began to decrease

and the hull continued to rise out of the water. Throughout this period, the wake generated by the hull became more defined and wake angle decreased. Each of these observations were consistent with those from previous studies and showed that the CFD simulation was capable of modeling the flow around a planing hull.

The next phase of this study was to validate the initial CFD model with a scale model experiment. A scale model of the base hull was tested in GVSU's tow tank. The scale model results showed the same trend in total drag but the values for drag coefficient were lower than those from the CFD model. The scale model results also showed that the simulation was accurately predicting the trim angle and sinkage of the hull to within 12%. Any discrepancies could have been caused by uncertainty in the strain gage or a difference in the center of mass and moment of inertia. These results showed that the CFD simulation was accurate and capable of examining the effects of different geometric features on the performance of the hull.

The final stage of this study, a full DOE analysis was performed on the effects of deadrise angle, keel line height, and spray rail location. The results from the ANOVA tests showed there was significant evidence to reject the null hypothesis and conclude that several geometric features had an effect on the performance of the hull. Increasing the deadrise angle caused an increase in trim angle, a decrease in sinkage, and an increase in total drag. The keel line height had similar effects. As the height of the keel line increased, the trim angle and sinkage decreased while the total drag increased. Adding spray rails significantly increased the sinkage while changing the position affected the total drag. As the spray rails were moved laterally out from the center of the hull the total drag increased. The final significant term was the two way interaction between deadrise angle and the keel line geometry. As one was increased, the effect of the other on the total drag also increased.

The results of this study showed that computational fluid dynamics could be used to accurately model the flow around a planing hull and examine different hull geometries. Based on the tested cases, the total drag on the hull could be reduced by decreasing the deadrise angle, decreasing the keel line height, or moving the location of the spray rails toward the center line of the hull. Using this method, other geometric features could be analyzed to optimize the performance of planing hulls.

9. Future Work

There are several areas of study that could improve upon the finding of this thesis. Future work should focus into three distinct areas. The first is examining the hull at lower speeds. Although determining hull resistance while planing is important, improving the hull's performance during the transition region is also important. Examining the time to plane, and planing speed could improve a hull's efficiency and increase the fuel economy. The next area would involve changing the fluid conditions. An examination of the hull's performance in a current, with a strong cross wind, or in head seas would provide valuable information on the real world implications of the hull's design. The final area of future work should focus on examining different geometric features and how they affect the performance of the hull. Changing the shape of the spray rails or adding multiple to the hull would provide valuable information missing from this study.

References

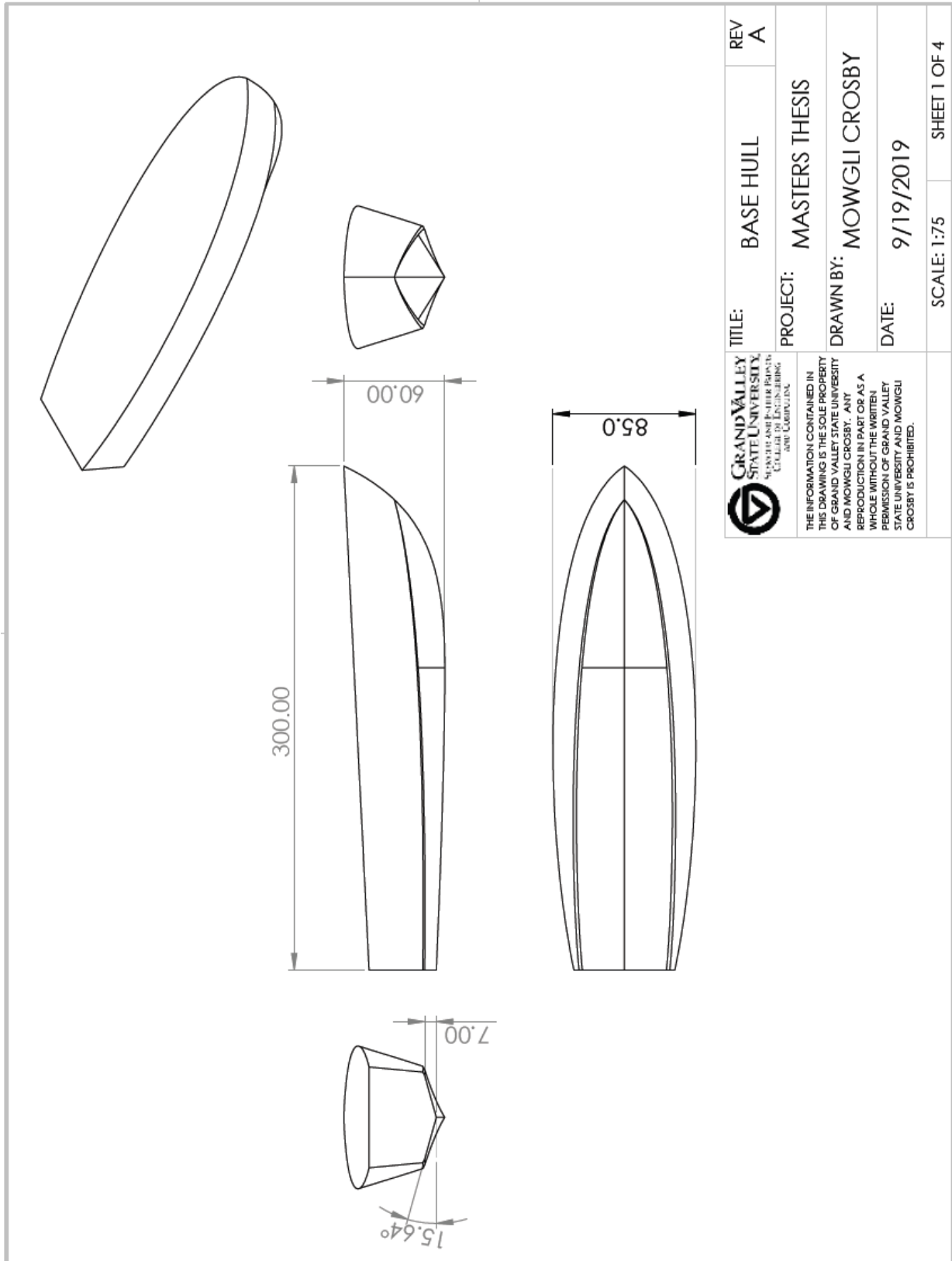
1. Dixon, T. (n.d.). Uffa Fox Biography. Retrieved November 16, 2018 from <http://www.uffafox.com/uffabiog.htm>
2. Yousefi, R., Shafaghat, R., & Shakeri, M. (2013). Hydrodynamic Analysis Techniques For High Speed Planing Hulls. *Applied Ocean Research*, 42, 105-113. doi:10.1016/j.apor.2013.05.004
3. Potgieter, K. (n.d.). Planing Hulls. *Kobus Naval Design*.
4. Mackenzie, M. (2005). *The Dictionary of English Nautical Language*. Nova Scotia, Canada
5. Resistance and Powering of Ships. (n.d.). In *Principles of Ship Performance*. Annapolis, MD: United States Naval Academy.
6. Ghadimi, P., Tavakoli, S., & Dashtimanesh, A. (2014). A Mathematical Scheme for Calculation of Lift of Planing Crafts with Large Mean Wetted Length and a Comparative Study of Effective Parameters. *Universal Journal of Fluid Mechanics*, 35(54)
7. Munson, B. R., Okiishi, T. H., Huebsch, W. W., & Rothmayer, A. P.(2013). *Fundamentals of Fluid Mechanics* (7th ed.). Hoboken, N. J.: John Wiley & Sons.
8. David, C. G., Roeber, V., Goseberg, N., & Schlurmann, T. (2017). Generation and Propagation of Ship-borne Waves - Solutions from a Boussinesq-type Model. *Coastal Engineering*, 127, 170-187. doi:10.1016/j.coastaleng.2017.07.001
9. Rabaud, M., & Moisy, F. (2014). Narrow Ship Wakes and Wave Drag for Planing Hulls. *Ocean Engineering*, 90, 34-38. doi:10.1016/j.oceaneng.2014.06.039

10. Matveev, K. I. (2014). Hydrodynamic Modeling of Planing Hulls with Twist and Negative Deadrise. *Ocean Engineering*, 82, 14-19.
doi:10.1016/j.oceaneng.2014.02.021
11. Caponnetto, M. (2015). *Practical CFD Simulations for Planing Hull* (Tech.). Balerna, Switzerland: ResearchGate.
12. Taunton, D., Hudson, D., & Sheno, R. (n.d.). Characteristics of a Series of High Speed Hard Chine Planing Hulls
13. Luca, F. D., & Pensa, C. (2017). The Naples Warped Hard Chine Hulls Systematic Series. *Ocean Engineering*, 139, 205-236. doi:10.1016/j.oceaneng.2017.04.038
14. Seo, J., Choi, H., Jeong, U., Lee, D. K., Rhee, S. H., Jung, C., & Yoo, J. (2016). Model Tests on Resistance and Seakeeping Performance of Wave-Piercing High-Speed Vessel with Spray Rails. *International Journal of Naval Architecture and Ocean Engineering*, 8(5), 442-455. doi:10.1016/j.ijnaoe.2016.05.010
15. Kim, D. J., Kim, S. Y., You, Y. J., Rhee, K. P., Kim, S. H., & Kim, Y. G. (2013). Design of High-Speed Planing Hulls for the Improvement of Resistance and Seakeeping Performance. *International Journal of Naval Architecture and Ocean Engineering*, 5(1), 161-177. doi:10.3744/jnaoe.2013.5.1.161
16. Yousefi, R., Shafaghat, R., & Shakeri, M. (2014). High-Speed Planing Hull Drag Reduction Using Tunnels. *Ocean Engineering*, 84, 54-60.
doi:10.1016/j.oceaneng.2014.03.033
17. Jiang, C. G., Xin, S. C., & Wu, C. W. (2011). Drag Reduction of a Miniature Boat with Superhydrophobic Grille Bottom. *AIP Advances*, 1(3), 032148.
doi:10.1063/1.3633686

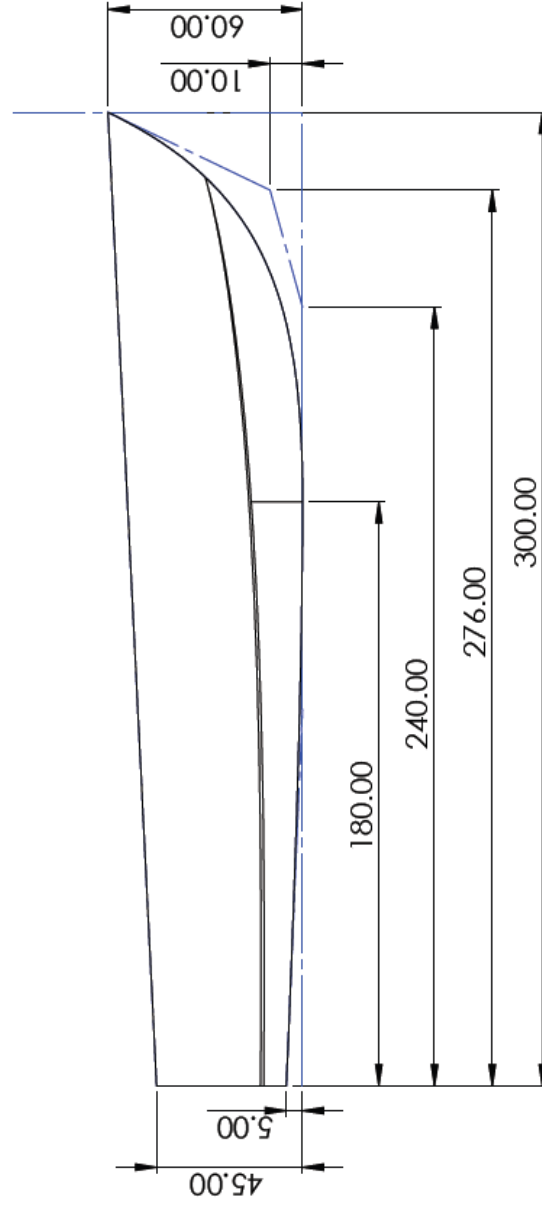
18. Versteeg, H. K., & Malalasekera, W. (2010). *An Introduction to Computational Fluid Dynamics: The Finite Volume Method* (2nd ed.). Harlow: Pearson/Prentice Hall.
19. Frisk, D., & Tegehall, L. (2015). *Prediction of High-Speed Planing Hull Resistance and Running Attitude* (Unpublished master's thesis). Chalmers University of Technology.
20. Launder, B. E., Spalding, D. B. *Lectures in Mathematical Models of Turbulence*. London: Academic Press; 1972.
21. Wilcox, D. C. *Turbulence Modeling for CFD*. 3rd ed. La Canada: DCW Industries; 2006.
22. Menter, F. R. Two-Equation Eddy-Viscosity Turbulence Models for Engineering Applications. *The American Institute of Aeronautics and Astronautics Journal*. 1994;32(8):1598–1605. doi: 10.2514/3.12149.
23. Gopala, V. R., vanWachem, B. G. M. Volume of Fluid Methods for Immiscible-Fluid and Free-Surface Flows. *Chemical Engineering Journal*. 1-3 2008;141:204–221. doi: 10.1016/j.cej.2007.12.035.
24. *STAR CCM+ User Manual*, 13th ed. Siemens, Berlin, Germany, 2019
25. Pérez-Arribas, F. (2014). Parametric Generation of Planing Hulls. *Ocean Engineering*, 81, 89-104. doi:10.1016/j.oceaneng.2014.02.016
26. 2019 Boat Buyer's Guide. (2018, December 11). Retrieved January 15, 2019 from <https://www.onthewater.com/2019-boat-buyers-guide>
27. Woodward, C. (2019, March 20). 20 Best Center Console Fishing Boats, 26 Feet and Under. Retrieved January 15, 2019 from <https://www.sportfishingmag.com/20-top-center-consoles-26-feet-and-under/>

28. *Recommended procedures, testing and extrapolation methods*, Rev. 01. International Towing Tank Conference, Denmark, 2002, pp. 1-11
29. Daniel, W. W., & Cross, C. L. (2014). *Biostatistics: a foundation for analysis in the health sciences* (10th ed.). Hoboken (New Jersey): John Wiley & Sons.
30. Montgomery, D. C. (2013). *Design and analysis of experiments* (8th ed.). Hoboken (New Jersey): John Wiley & Sons

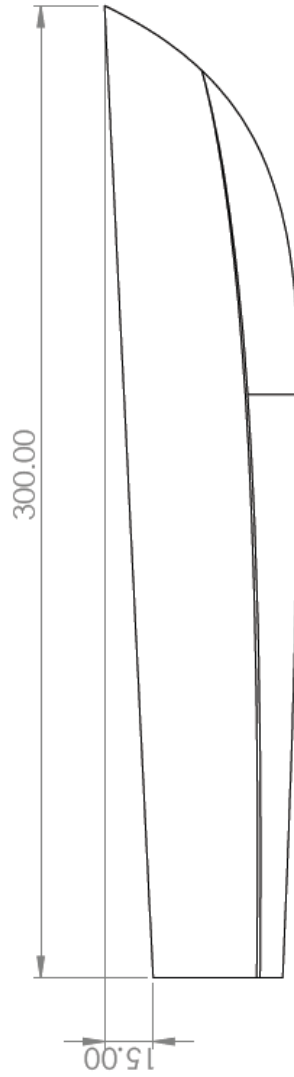
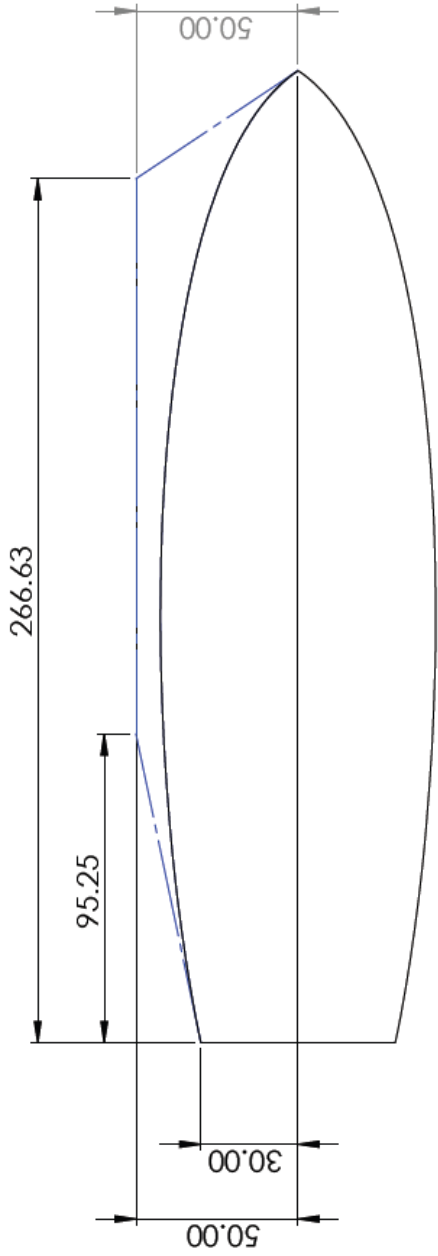
Appendix A – Drawings



 GRAND VALLEY STATE UNIVERSITY <small>MEMBER AND FOUNDER PARTNER</small> <small>COLLEGE OF ENGINEERING AND COMPUTING</small>	TITLE:	BASE HULL	REV	A
	PROJECT:	MASTERS THESIS		
<small>THE INFORMATION CONTAINED IN THIS DRAWING IS THE SOLE PROPERTY OF GRAND VALLEY STATE UNIVERSITY AND MOWGLI CROSBY. ANY REPRODUCTION IN PART OR AS A WHOLE WITHOUT THE WRITTEN PERMISSION OF GRAND VALLEY STATE UNIVERSITY AND MOWGLI CROSBY IS PROHIBITED.</small>	DRAWN BY:	MOWGLI CROSBY		
	DATE:	9/19/2019		
	SCALE:	1:75	SHEET 1 OF 4	

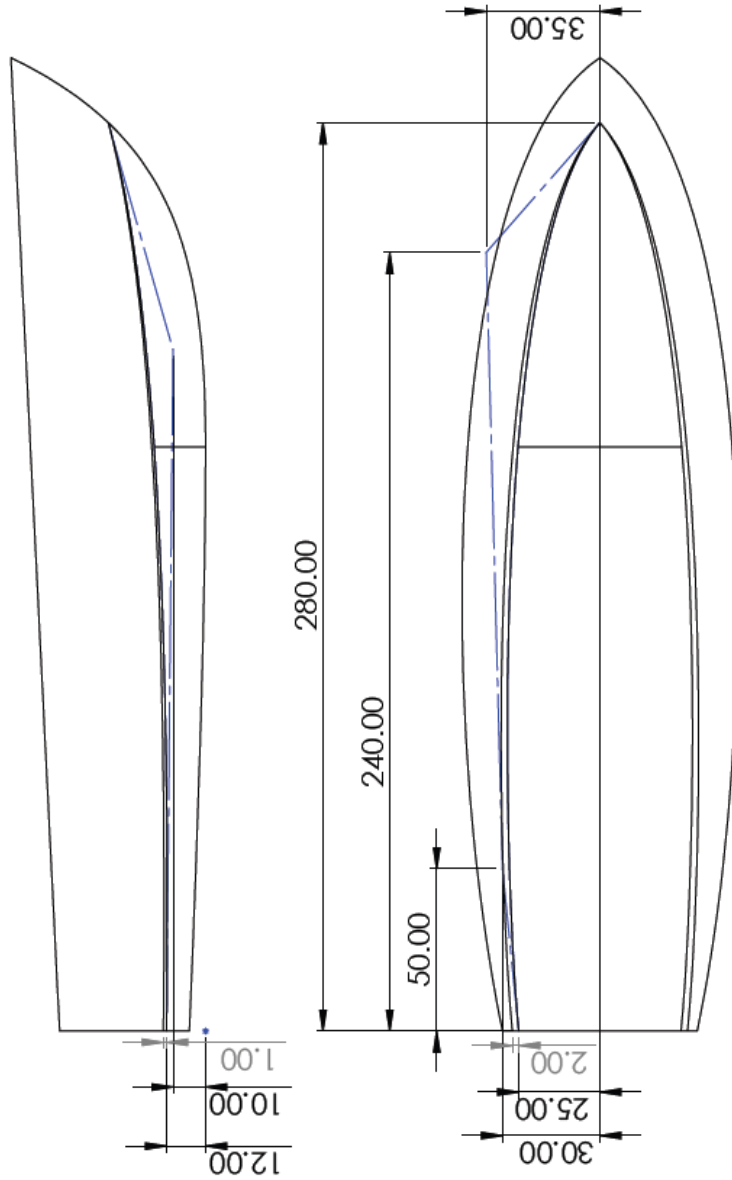


 GRAND VALLEY STATE UNIVERSITY <small>SCHOOL OF ENGINEERING AND COMPUTING</small>	TITLE:	BASE HULL	REV	A	
	PROJECT:	MASTERS THESIS			
	DRAWN BY:	MOWGLI CROSBY			
	DATE:	9/19/2019			
<small>THE INFORMATION CONTAINED IN THIS DRAWING IS THE SOLE PROPERTY OF GRAND VALLEY STATE UNIVERSITY AND MOWGLI CROSBY. ANY REPRODUCTION IN PART OR AS A WHOLE WITHOUT THE WRITTEN PERMISSION OF GRAND VALLEY STATE UNIVERSITY AND MOWGLI CROSBY IS PROHIBITED.</small>			SCALE:	1:50	
				SHEET 2 OF 4	



THE INFORMATION CONTAINED IN THIS DRAWING IS THE SOLE PROPERTY OF GRAND VALLEY STATE UNIVERSITY AND MOWGLI CROSBY. ANY REPRODUCTION IN PART OR AS A WHOLE WITHOUT THE WRITTEN PERMISSION OF GRAND VALLEY STATE UNIVERSITY AND MOWGLI CROSBY IS PROHIBITED.

TITLE:	BASE HULL	REV	A
PROJECT:	MASTERS THESIS		
DRAWN BY:	MOWGLI CROSBY		
DATE:	9/19/2019		
SCALE: 1:50		SHEET 3 OF 4	



 GRAND VALLEY STATE UNIVERSITY <small>UNIVERSITY AND FERRIS DIVISION</small> <small>SCHOOL OF ENGINEERING</small> <small>AND COMPUTER</small>	TITLE:	BASE HULL	REV	A
	PROJECT:	MASTERS THESIS		
	DRAWN BY:	MOWGLI CROSBY		
	DATE:	9/19/2019		
<small>THE INFORMATION CONTAINED IN THIS DRAWING IS THE SOLE PROPERTY OF GRAND VALLEY STATE UNIVERSITY AND MOWGLI CROSBY. ANY REPRODUCTION IN PART OR AS A WHOLE WITHOUT THE WRITER PERMISSION OF GRAND VALLEY STATE UNIVERSITY AND MOWGLI CROSBY IS PROHIBITED.</small>		SCALE:	1:50	SHEET 4 OF 4